UNIVERSITY OF CALIFORNIA

Santa Barbara

Epitaxial Design and Characterization of III-Nitride Optoelectronic Devices

A dissertation submitted in partial satisfaction of the

requirements for the degree

Doctor of Philosophy in Materials

by

Yi Chao Chow

Committee in charge:

Professor James S. Speck, Chair

Professor Claude Weisbuch

Professor Steven P. DenBaars

Professor John E. Bowers

Professor Jonathan Klamkin

September 2022

The dissertation of Yi Chao Chow is approved.

_____

Claude Weisbuch

_____

Steven P. DenBaars

_____

John E. Bowers

_____

Jonathan Klamkin

_____

James S. Speck, Committee Chair

September 2022

ACKNOWLEDGEMENTS

First of all, I would like to extend my deepest gratitude to my advisor, Professor Jim Speck for the guidance and support during my time at UCSB. I would also like to thank my committee members, Professors Claude Weisbuch, Steve DenBaaars, John Bowers, and Jonathan Klamkin for the advice and resources they provided throughout my PhD study.

I am indebted to a few people who have taught me so much when I first joined the group. I want to thank Changmin Lee, Abdullah Alhassan, Matthew Wong, Guillaume Lheureux, and Shlomo Mehari, from whom I have learned so much about MOCVD growth, cleanroom processing, characterization, and device simulations. I'm also extremely grateful to work at UCSB which has a great support network of technical and support staff. Thank you to the MOCVD lab staff (Mike, David, Brian), cleanroom staff (Don, Brian, Aidan), CNSI staff (Tom), and SSLEEC staff (Feng Wu, Tal, Yukina, Emi, Tara).

I'm grateful to have shared the MOCVD reactors with so many brilliant growers and to have worked with so many talented people in the nitrides group at UCSB. In particular, I want to acknowledge a few collaborators: Cheyenne Lynsky, Mylène Sauty, Haojun Zhang, and Hongjian Li.

My graduate career has been financially supported by CREST. Special thanks to Jaffri, Hoo Kooi, and Lau Yue Hoong for doing an excellent job handling the financial duties, allowing me to focus on my study.

I also would like to thank my friends who have made my time in Santa Barbara truly enjoyable: Clayton, Chen, Yating, Zach, Brent, John, Suyi, Warren, Alex, Rubayn, ZJ, Ashley, and Kenneth.

Lastly, I want to thank my parents, my sister, and my fiancée, Wan Ying for their unwavering support.

VITA OF YI CHAO CHOW

September 2022

Education

University of California, Santa Barbara Sept. 2016- Sept. 2022
Ph.D. in Materials Engineering
Advisor: Prof. James S. Speck
Dissertation Title: Epitaxial Design and Characterization of III-Nitride Optoelectronic Devices *CGPA: 3.92*

University of Washington Sept. 2011- June 2015
Bachelor of Science, *magna cum laude*
Physics; Mathematics *CGPA: 3.88*

Experience

Graduate Researcher, University of California, Santa Barbara Sept. 2016- Present

- MOCVD growth and material characterization of III-nitride thin films for LEDs and photodetectors.
- Fabrication of III-nitride devices in cleanroom facility.
- Designed optical and electrical experiments to study III-nitride devices.
- Developed *c*-plane InGaN-based LEDs with low efficiency droop through internal electric field engineering.
- Developed high-speed *c*-plane InGaN-based photodetectors for visible light communication (VLC).
- Characterization of high-speed III-nitride devices such as lasers, photodetectors, and micro-LEDs.

Teaching Assistance, University of California, Santa Barbara

- Course: Fundamentals of Electronic Solids Jan. 2022- March 2022
- Course: Electronic & Atomic Structure of Materials Jan. 2018- March 2018

Product Engineer, Texas Instruments Jan. 2016- Aug. 2016

- Developed ATE test programs for production use.

Industrial Trainee, OSRAM Opto Semiconductors Sept. 2015- Nov. 2015

- Optical characterization of LEDs.

Undergraduate Researcher, Ultracold Atoms Group, University of Washington Dec. 2013- June 2015

- Constructed a lithium vapor cell using ultra-high vacuum techniques.
- Developed the frequency stabilization of the cooling lasers on the lithium D1 transition via saturated absorption laser spectroscopy.

Publications

Y. C. Chow, C. Lynsky, S. Nakamura, S. P. DenBaars, C. Weisbuch, and J. S. Speck, "Impact of doped barriers on the recombination coefficients of *c*-plane InGaN/GaN single quantum well light-emitting diodes," (submitted).

W. Y. Ho, A. I. Alhassan, C. Lynsky, **Y. C. Chow**, S. P. DenBaars, S. Nakamura, J. Peretti, C. Weisbuch, and J. S. Speck, "Detection of hot electrons originating from side valley at ~1.7 eV above the Γ-valley in wurtzite GaN using Electron Emission Spectroscopy (EES)," (submitted).

M. Sauty, N. Alyabyeva, C. Lynsky, **Y. C. Chow**, S. Nakamura, J. S. Speck, Y. Lassailly, A. C. H. Rowe, C. Weisbuch, and J. Peretti, "Probing local emission properties in InGaN/GaN quantum wells by scanning tunneling luminescence microscopy," arXiv Prepr. arXiv2208.08298 (2022).

P. Li, H. Zhang, H. Li, T. Cohen, R. Anderson, M. S. Wong, E. Trageser, **Y. C. Chow**, M. de Vries, S. Nakamura, and S. P. DenBaars, "Demonstration of yellow (568 nm) stimulated emission from optically pumped InGaN/GaN multi-quantum wells," Appl. Phys. Lett. 121, 71103 (2022).

R. Yapparov, C. Lynsky, **Y. C. Chow**, S. Nakamura, J. S. Speck, and S. Marcinkevičius, "Optimization of InGaN quantum well interfaces for fast interwell carrier transport and low nonradiative recombination," in *Gallium Nitride Materials and Devices XVII*, H. Fujioka, H. Morkoç, and U. T. Schwarz, eds. (SPIE, 2022), Vol. 12001, p. 1200104.

Y. C. Chow, C. Lynsky, F. Wu, S. Nakamura, S. P. DenBaars, C. Weisbuch, and J. S. Speck, "Reduction of efficiency droop in c-plane InGaN/GaN light-emitting diodes using a thick single quantum well with doped barriers," Appl. Phys. Lett. 119, 221102 (2021).

S. Marcinkevičius, R. Yapparov, **Y. C. Chow**, C. Lynsky, S. Nakamura, S. P. DenBaars, and J. S. Speck, "High internal quantum efficiency of long wavelength InGaN quantum wells," Appl. Phys. Lett. 119, 71102 (2021).

W. Y. Ho, **Y. C. Chow**, D. J. Myers, F. Wu, J. Peretti, C. Weisbuch, and J. S. Speck, "Quantitative correlation of hot electron emission to Auger recombination in the active region of c-plane blue III-N LEDs," Appl. Phys. Lett. 119, 51105 (2021).

C. Lynsky, R. C. White, **Y. C. Chow**, W. Y. Ho, S. Nakamura, S. P. DenBaars, and J. S. Speck, "Role of V-defect density on the performance of III-nitride green LEDs on sapphire substrates," J. Cryst. Growth 560–561, 126048 (2021).

R. Yapparov, **Y. C. Chow**, C. Lynsky, F. Wu, S. Nakamura, J. S. Speck, and S. Marcinkevičius, "Variations of light emission and carrier dynamics around V-defects in InGaN quantum wells," J. Appl. Phys. 128, 225703 (2020).

Y. C. Chow, C. Lee, M. S. Wong, Y.-R. Wu, S. Nakamura, S. P. DenBaars, J. E. Bowers, and J. S. Speck, "Dependence of carrier escape lifetimes on quantum barrier thickness in InGaN/GaN multiple quantum well photodetectors," Opt. Express 28, 23796–23805 (2020).

H. Li, H. Zhang, P. Li, M. S. Wong, **Y. C. Chow**, S. Pinna, J. Klamkin, P. DeMierry, J. S. Speck, S. Nakamura, and S. P. DenBaars, "Development of efficient semipolar {InGaN} long wavelength light-emitting diodes and blue laser diodes grown on a high quality semipolar GaN/sapphire template," J. Phys. Photonics 2, 31003 (2020).

H. Li, P. Li, H. Zhang, **Y. C. Chow**, M. S. Wong, S. Pinna, J. Klamkin, J. S. Speck, S. Nakamura, and S. P. DenBaars, "Electrically driven, polarized, phosphor-free white semipolar (20-21) InGaN light-emitting diodes grown on semipolar bulk GaN substrate," Opt. Express 28, 13569–13575 (2020).

M. Khoury, H. Li, P. Li, **Y. C. Chow**, B. Bonef, H. Zhang, M. S. Wong, S. Pinna, J. Song, J. Choi, J. S. Speck, S. Nakamura, and S. P. DenBaars, "Polarized monolithic white semipolar (20–21) InGaN light-emitting diodes grown on high quality (20–21) GaN/sapphire templates and its application to visible light communication," Nano Energy 67, 104236 (2020).

H. Li, M. S. Wong, M. Khoury, B. Bonef, H. Zhang, **Y. C. Chow**, P. Li, J. Kearns, A. A. Taylor, P. De Mierry, Z. Hassan, S. Nakamura, and S. P. DenBaars, "Study of efficient semipolar (11-22) InGaN green micro-light-emitting diodes on high-quality (11-22) GaN/sapphire template," Opt. Express 27, 24154–24160 (2019).

Awards

Outstanding Graduate Student Research Achievement Award 2019
SSLEEC, University of California, Santa Barbara

Mary Gates Research Scholarship 2014
University of Washington

ABSTRACT

Epitaxial Design and Characterization of III-Nitride Optoelectronic Devices

by

Yi Chao Chow

The III-nitride material system, i.e., (In, Ga, Al)N, which has a direct bandgap ranging from 0.7 eV to 6 eV, is well-suited for a wide range of optoelectronic devices. One of them would be the InGaN-based light-emitting diode (LED), which has become one of the leading general illumination technologies. The success of nitride LEDs has also sparked interest in other optoelectronic devices including photodetectors. This dissertation focuses on the development of both III-nitride photodetectors and LEDs.

In recent years, increasing interest in visible light communication (VLC) has created demand for high-speed photodetectors in the visible light spectrum. InGaN-based photodetectors, which offer great wavelength-selective response due to its tunable bandgap, are promising candidates for optical receivers in VLC links. Instead of the InGaN double heterostructure devices, InGaN-based photodetectors with multiple quantum well (MQW) structure designs are favored due to their significant advantages in terms of growth. The speed limiting factors of such devices were studied to improve their speed performance. On top of the usual RC time constant, InGaN/GaN MQW photodetectors are also limited by carrier escape lifetimes due to carrier trapping in the QWs. By reducing the thickness of the quantum barriers, carrier escape lifetimes were reduced, resulting in a twofold improvement in the 3-dB bandwidth of the photodetectors.

Despite the huge success of InGaN-based LEDs in solid-state lighting, one of the most enduring challenges that still limit the LEDs is the efficiency droop phenomenon, which refers to the decrease in the quantum efficiency with increasing injection current density. In conventional *c*-plane LEDs, polarization-induced electric fields further exacerbate the droop problem. The large internal electric fields in the quantum wells lead to a reduction in the overlap of the electron and hole wavefunctions. This lowers the recombination coefficients and causes an increase in carrier density at a given current density, leading to an early onset of efficiency droop due to the nonlinear Auger recombination. Additionally, the large internal electric fields also prevent the use of thick QW active region designs to reduce the carrier densities. One approach to reduce the internal electric field in *c*-plane QWs is through the use of doped barriers. However, the heavily doped Mg(Si)-doped *p*(*n*)-type GaN barriers also lead to a higher defect density. Growth optimization was performed with the aim of maximizing the field reduction and minimizing the detrimental impact of the doped barriers. With doped barriers, we demonstrated a 9-nm-thick single QW LED with a low efficiency droop. Biased photocurrent spectroscopy was also carried out to illustrate the effect of doped barriers on the internal electric fields. Device simulations were used in tandem with experimental results to guide the interpretation of the results. Lastly, differential carrier lifetime measurements were performed to determine the impact of doped barriers on the recombination coefficients of the LEDs. The improvement in the radiative coefficients in the LEDs with doped barriers, coupled with the blueshift of the emission wavelengths, indicates an enhancement in wavefunction overlap and a reduction of quantum confined Stark effect (QSCE) as a result of the reduced internal electric field.

TABLE OF CONTENTS

1 Introduction **1**

1.1 III-nitride material system **1**

1.2 III-nitride light-emitting diode **4**

1.3 Photodetectors **8**

1.4 Preview of the dissertation **13**

2 High-Speed InGaN-Based Photodetectors **16**

2.1 Background and motivation **16**

2.2 Progress in III-nitride photodetectors **19**

2.2.1 AlGaN-based and GaN-based photodetectors **19**

2.2.2 InGaN-based photodetectors **21**

2.3 Epitaxial structure and fabrication **24**

2.4 Characterization **26**

2.5 Speed improvement through reduction of quantum barrier thickness **30**

2.5.1 Responsivity and 3-dB bandwidth **31**

2.5.2 Speed limitations **33**

2.5.3 Experimental carrier escape lifetimes **38**

2.6 Future work **42**

2.7 Conclusion **45**

3 Internal Electric Field Reduction in *c*-plane InGaN/GaN Single Quantum Well Light-Emitting Diodes **53**

3.1 Introduction **53**

3.2 Understanding reduction of internal electric fields through doped barriers **56**

3.3 Growth optimization of thin SQW LEDs **66**

3.3.1 Impact of doping level and location of doped barriers on thin SQW LEDs **67**

3.3.2 2-step barrier growth **70**

3.3.3 Improving doping profile and incorporation of Mg **72**

3.4 Growth optimization of thick SQW LEDs **78**

3.4.1 Optimizing the thicknesses of the UID GaN interlayers in thick SQW LEDs **79**

3.4.2 Optimizing the doping levels of the doped barriers in thick SQW LEDs **83**

3.5 Impact of doped barriers and quantum well thickness on the LED performance **86**
3.5.1 Biased photocurrent spectroscopy and simulated electric field profiles **87**
3.5.2 Simulated electron-hole wavefunction overlap **92**
3.5.3 Simulated energy band diagrams **94**
3.5.4 External quantum efficiency and electroluminescence wavelengths **99**
3.6 Impact of doped barriers on the recombination coefficients of *c*-plane InGaN/GaN single quantum well LEDs **103**
3.6.1 External quantum efficiency and electroluminescence wavelengths **105**
3.6.2 Differential carrier lifetime measurements and evaluation of recombination coefficients **107**
3.6.3 Discussion **112**
3.6.4 Modulation bandwidths **115**
3.7 Conclusion **117**

1

Introduction

1.1 III-nitride material system

III-nitride material system consists of GaN, InN, AlN, and their alloys. They exist in two different crystal structures (wurtzite or zinc blende) but in this dissertation, only the more stable wurtzite form is considered (Figure 1.1). III-nitride materials form a continuous alloy system, with direct bandgaps ranging from 0.7 eV (near IR) to 6 eV (mid UV) as shown in Figure 1.2, making them suitable for many optoelectronic applications.

Due to their non-centrosymmetric crystal structure, wurtzite III-nitrides are polar materials. As such, spontaneous polarization presents in the materials without any external

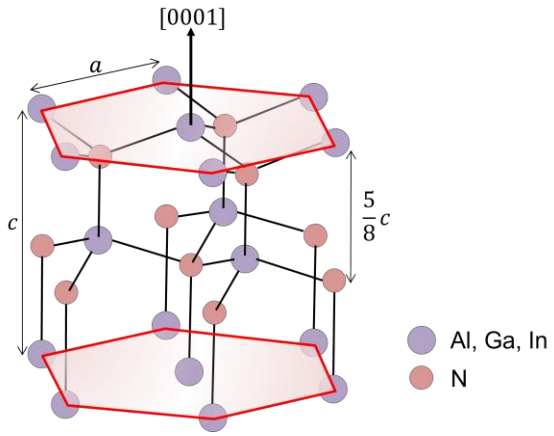

Figure 1.1. Crystal structure of wurtzite III-nitride compounds.

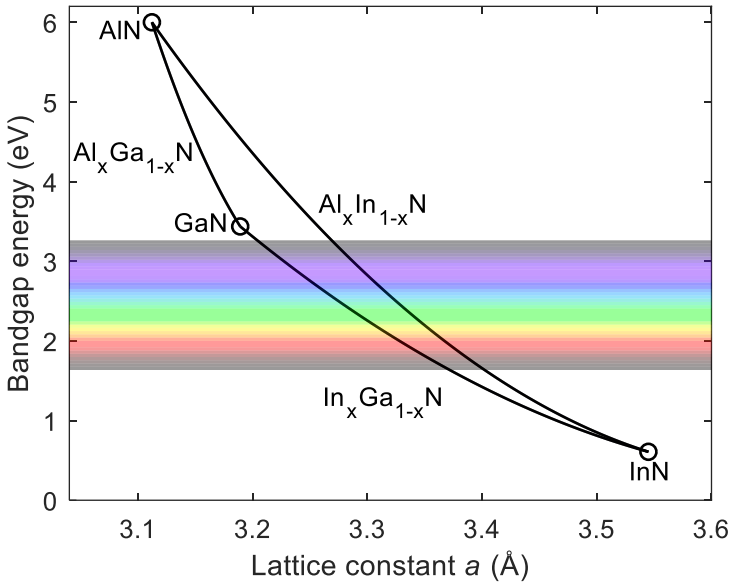

Figure 1.2. Bandgap energy vs. lattice constant for III-nitride material system at 300 K.

electric field. The origin of spontaneous polarization is the deviation from ideal tetrahedral coordination of the atoms and the partially ionic nature of the bonds between nitrogen and metal ions. A hexagonal closed packed (HCP) crystal with zero spontaneous polarization has an ideal c/a ratio of 1.633. Table 1-1 shows the c/a ratio for each III-nitride binary compound [1]. The deviation from the ideal c/a leads to unbalanced compensation polarization along the polar c-axis, resulting in the spontaneous polarization [2]. Additionally, for the common (0001) c-plane growth, equibiaxial compressive or tensile stress due to lattice mismatch between epitaxial alloy layers can further distort the crystal lattice. This exacerbates the deviation from the ideal c/a ratio, leading to strain-induced piezoelectric polarization.

The spontaneous and piezoelectric polarization for III-nitride materials is directed along the c-axis of the wurtzite crystal structure which coincides with the typical growth direction of

	Ideal	InN	GaN	AlN
c/a	1.633	1.618	1.634	1.606

Table 1-1. Bulk c/a ratios for InN, GaN, and AlN.

III-nitride heteroepitaxial structures. The polarization charges resulting from polarization discontinuities at heterointerfaces cause large electric fields in the III-nitride layers. III-nitride devices like AlGaN/GaN high-electron-mobility transistors (HEMT) benefit from the polarization-induced two-dimensional electron gas (2DEG). However, for some optoelectronic devices such as light-emitting diodes (LEDs) and photodetectors, the resulting electric fields in the InGaN/GaN quantum wells are generally detrimental to the device performance.

1.2 III-nitride light-emitting diodes

The demonstration of the first blue InGaN LEDs by Shuji Nakamura in the early 1990s sparked intense research on III-nitride materials. Nowadays, III-nitride LEDs, which are the basis of solid-state lighting, have become one of the predominant general illumination technologies. The most common way to create white light emission is by combining blue LEDs with phosphor with broad emission centered at yellow emission wavelengths. The combination of the emission from the LED and the phosphor appears white to human eyes. White light can also be achieved by using color-mixed LEDs (i.e., mixing together several monochromatic LEDs to produce white light) which have a higher fundamental efficiency limit of around 400 lm/W than phosphor-converted LEDs [3,4]. This and the pursuit for next generation displays using RGB micro-LEDs have led to great interest in long-wavelength LEDs (green, yellow, and red LEDs) in recent years.

LED structures are based on GaN *p*-*n* junctions. For visible III-nitride LEDs, InGaN/GaN QWs (active region) are placed in the depletion region of the *p*-*n* junction. Under forward bias, electrons and holes are injected into the QWs where they recombine either radiatively or non-radiatively. There are three important recombination processes in III-nitride LEDs as shown in Figure 1.3. Each process has a different dependence on the carrier densities (n) in the QW: Shockley-Read-Hall (SRH) non-radiative recombination (proportional to n), bimolecular radiative recombination (proportional to n^2), and Auger non-radiative recombination (proportional to n^3).

The internal quantum efficiency (IQE), which is an important quantity for LEDs, is the ratio of radiative recombination to total recombination as follows:

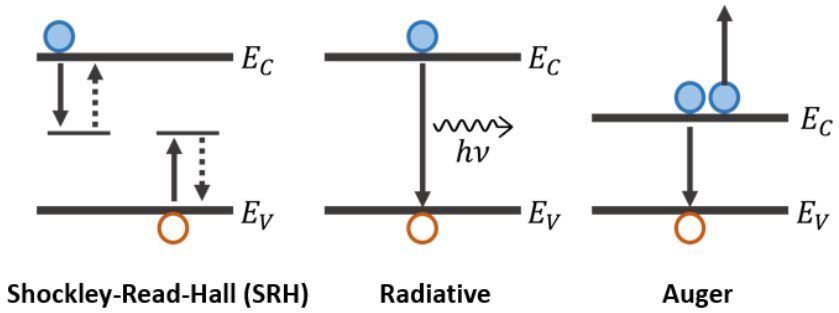

Figure 1.3. Recombination processes in III-nitride LEDs.

$$IQE = \frac{Bn^2}{An + Bn^2 + Cn^3} \tag{1}$$

where *A*, *B*, and *C* are the coefficients for SRH, radiative, and Auger recombination, respectively. IQE is not an easily accessed quantity. On the other hand, external quantum efficiency, which is defined as the ratio of emitted photons to injected electrons, can be directly measured (e.g., by integrating sphere) and is related to IQE by the following equation:

$$EQE = IQE \times LEE \tag{2}$$

where LEE is the light extraction efficiency. In addition, the injected current density (*J*) is given by

$$J = qh(An + Bn^2 + Cn^3) \tag{3}$$

where *q* and *h* are the electron charge and the active region thickness, respectively.

A typical dependence of the IQE of a LED on the current density is shown in Figure 1.4. Due to the different dependence on *n*, SRH and Auger recombination dominate at low and high current densities, respectively. The decrease in the quantum efficiency with increasing injection current density (and with it, the carrier density) at high current densities is commonly

referred to as the efficiency droop which is one of the most enduring challenges in III-nitride LEDs.

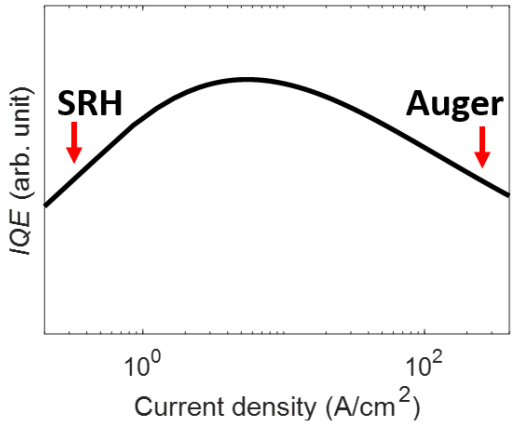

Figure 1.4. A typical IQE curve as a function of current density.

III-nitride LEDs are commonly grown along the [0001] *c*-axis. As such, polarization-induced electric fields play a significant role in the recombination physics of the *c*-plane devices. Due to the magnesium memory effect, *c*-plane LEDs are usually grown n-side first. In a conventional Ga-polar p-side-up device orientation, the polarization-induced electric fields (mostly piezoelectric polarization) point in the opposite direction of the built-in or *p*-*n* junction electric field originating from the *p*-*n* junction. Since polarization fields are usually much larger than the *p*-*n* junction electric field, there is a large net internal electric field in the QWs.

The internal electric field in the QWs leads to a spatial separation of the electron and hole wavefunctions, causing a reduction in the wavefunction overlap ($I = \int \psi_e(z)\psi_h(z)\,dz$). Since the radiative coefficient (B) is proportional to the square of the matrix element of the electron-photon coupling Hamiltonian, which is proportional to the wavefunction overlap, B scales with the square of the wavefunction overlap ($B \propto |I|^2$). The reduction of the radiative coefficient is often focused on as the main impact of reduced wavefunction overlap. However,

theoretical and experimental studies have shown that the other non-radiative recombination processes (SRH and Auger) also exhibit dependence on wavefunction overlap [5–8].

Kioupakis *et al.* argued that *A*, *B*, and *C* coefficients are all functions of the square of the wavefunction overlap [5]. An in-depth study of SRH recombination was carried out with numerous QW samples of varying In content and thickness which have vastly different wavefunction overlaps [7]. An empirical scaling law of $A \sim B^{0.9}$ was obtained, affirming that SRH coefficient is wavefunction-overlap dependent. A model of field-assisted multiphonon point defect recombination is then introduced to explain the dependence of SRH coefficient on the wavefunction overlap. Similarly, a strong correlation was also observed between *B* and *C* [8] where empirical dependence of $C \sim B^{1.2}$ was measured. The proposed model claims that the Auger recombination rates are determined by the spatial tails of decaying wavefunctions. As such, Auger recombination has a comparable dependence on wavefunction overlap.

In an ideal case where defect density remains constant, the peak IQE should not vary with wavefunction overlap owning to the similar overlap dependence of the recombination coefficients. Nonetheless, slower recombination processes (or lower coefficients) because of the large internal electric field, lead to an increase in the carrier density at a given current density. Consequently, the IQE peaks at a lower current density. In other words, the internal electric field leads to an early onset of efficiency droop. The trends have been observed experimentally in the past when LEDs with varying QW indium compositions were studied [6,9]. Therefore, being able to reduce the internal electric field effectively is essential in tackling the efficiency droop problem in *c*-plane LEDs.

1.3 Photodetectors

1.3.1 Basic operation of photodetectors

Photodetectors are devices that convert light to an electrical signal such as voltage or current. We will only consider *p-i-n* photodiode-based devices here as they are commonly used for high-speed applications. A *p-i-n* photodiode is a *p-n* diode with an intrinsic (often unintentionally doped) region sandwiched between the p-type and n-type layers (as shown in Figure 1.5(a)). The typical net charge distribution and the electric field of a *p-i-n* diode are also shown in Figure 1.5(b) and Figure 1.5(c), respectively. Note that the actual electric fields in *c*-plane InGaN-based photodetectors are slightly different due to the presence of polarization-induced electric fields.

The conversion is achieved through the absorption of light which leads to the creation of free electron-hole pairs (i.e., the creation of electrons and holes in the conduction band and valence band respectively). A photon can be absorbed if it has an energy greater than the

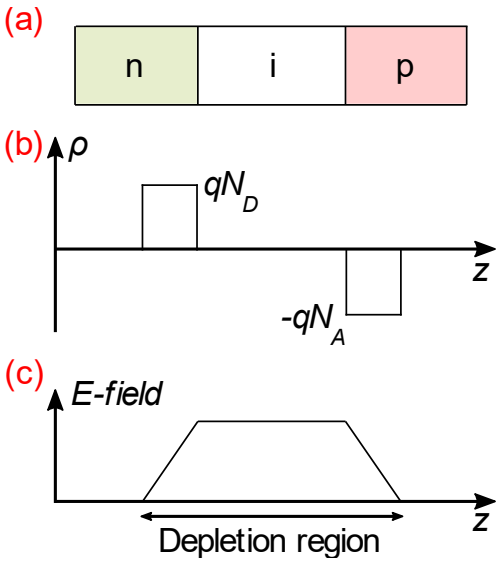

Figure 1.5. (a) The *p-i-n* structure and its (b) charge distribution and (c) electric field profile.

bandgap of the semiconductor. If the electron-hole pairs are photogenerated in the depletion region, the electric field separates the electrons and holes which subsequently drift toward the majority regions (i.e., electrons to the n-side and holes to the p-side of the junction). The current generated through the drifting carriers is called the photocurrent. Electron-hole pairs created outside the depletion layer region but within a diffusion length to the depletion region can still reach the depletion region by random diffusion and contribute to the photocurrent. If they are created outside the depletion layer region and not within a diffusion length to the depletion region, these carriers will be annihilated by recombination and do not contribute to the photocurrent.

1.3.2 Speed limitations

In general, the speed of photodetectors is limited by (1) carrier transit time, (2) diffusion current, (3) carrier trapping, and (4) RC time constant.

The carrier transit time is the time for a carrier to drift across the depletion region. The transit time limitation on the bandwidth of the photodetectors arises from the time delay introduced by the motion of the carriers through the active region. The transit time depends on the carrier velocities which, in turn, depends on the electric field across the photodiode. In high-speed operation, most photodetectors have high electric fields across the photodiode. Therefore, carriers are traveling at the saturation velocity most of the time. Normally, electron and hole saturation velocities are unequal, and the effective transit time of a photodetector is generally determined by the slower carriers.

The frequency response (H_i) of a *p*-*i*-*n* photodiode with excitation from the p-side is given by [10,11]:

$$H_i(\omega) = \frac{i(\omega)}{i(0)} = \frac{1}{1-e^{-\alpha L}}\left[\frac{1-e^{-\alpha L - j\omega\tau_p}}{j\omega\tau_p + \alpha L} + e^{-\alpha L}\frac{e^{-j\omega\tau_p - 1}}{j\omega\tau_p} + \frac{1-e^{-j\omega\tau_n}}{j\omega\tau_n} + e^{-\alpha L}\frac{1-e^{\alpha L - j\omega\tau_n}}{\alpha L - j\omega\tau_n}\right] \quad (4)$$

where $i(\omega)$ is the detected current at an angular modulation frequency (ω), $i(0)$ is the DC current, α is the absorption coefficient, L is the depletion width, $\tau_{p(n)} = L/v_{p(n)}$ is the hole (electron) transit time, and $v_{p(n)}$ is the hole (electron) velocity. This equation assumes constant carrier velocities in the depletion region and assumes that the absorbing layer thickness is the same as the depletion width. The equation for n-side illumination is obtained by interchanging the p and n subscripts.

The frequency response is plotted as a function of $\omega\tau_p$ as shown in Figure 1.6. Assuming equal electron and hole velocities ($v_n = v_p$), the half-power point of the function is at $\omega\tau_p = 3.5$ and $\omega\tau_p = 2.8$ for a uniformly illuminated detector ($\alpha L \to 0$) and an edge

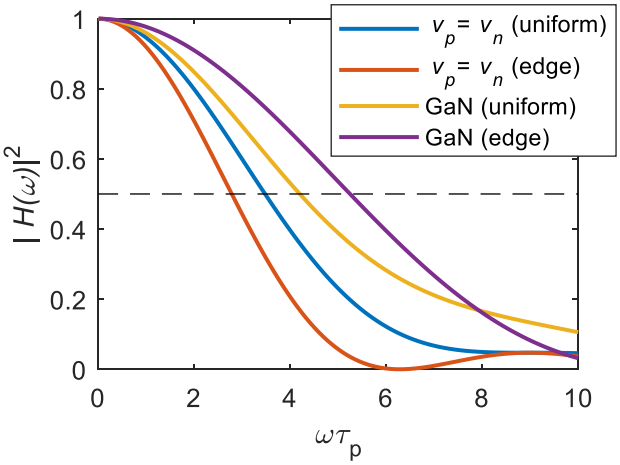

Figure 1.6. Frequency response of a *p-i-n* photodiode for the equal velocities case ($v_n = v_p$) and for GaN photodiodes ($v_p = 6.63 \times 10^6$ cm s^{-1} and $v_n = 1.25 \times 10^7$ cm s^{-1}).

illuminated detector ($\alpha L \to \infty$), respectively. Correspondingly, the transit-time-limited bandwidths for these two limits are then $f_{tr(\alpha L \to 0)} = 0.55/\tau_p$ and $f_{tr(\alpha L \to \infty)} = 0.45/\tau_p$. For InGaN-based photodetectors, saturation velocities of GaN ($v_p = 6.63 \times 10^6$ cm s^{-1} and $v_n = 1.25 \times 10^7$ cm s^{-1}) are used [12,13]. The transit-time-limited bandwidths are calculated to be $f_{tr(\alpha L \to 0)} = 0.67/\tau_p$ and $f_{tr(\alpha L \to \infty)} = 0.84/\tau_p$, respectively for the two limits. For a InGaN *p-i-n* photodiode with a 100-nm-thick intrinsic region, the transit-time-limited bandwidth is ~500 GHz.

Photodetectors are also limited by the diffusion current which is a relatively slow process compared with the drift process. Since the diffusion current can last as long as the carrier recombination lifetime, the diffusion current contributes to a slow tail to the impulse response. This problem can be eliminated by using a double-heterostructure design where larger bandgap materials sandwich a smaller bandgap material. This limits the light absorbing region to the high-field depletion region. Similarly, diffusion current is not a problem for the InGaN/GaN multiple quantum well (MQW) photodetectors, which are the focus of Chapter 2. The absorbing region of the structure is the InGaN QWs which are located in the depletion region of the junction.

However, this causes another problem – the carrier trapping of electrons and holes at the conduction band and valence band discontinuities, respectively. Carriers generally escaped via thermionic emission or tunneling [14,15]. This effect will be discussed more in detail for InGaN/GaN MQW photodetectors in section 2.5.2.

Lastly, the bandwidths of the photodetectors are also limited by the RC time constant. Generally, photodetectors can be modeled as a lumped-element device with the simplified

circuit diagram as shown in Figure 1.7. Assuming the photodetector is reverse biased, there is a depletion region capacitance. It can be modeled as a current source in parallel with a junction capacitor (C_J). There is also a parasitic capacitance (C_P) which depends on the metallization geometry and packaging. We also need to consider the series resistance (R_S) that is due to the ohmic contacts and bulk resistances. Lastly, a load resistance (R_L), which is usually $50\ \Omega$, is used to terminate the device. The RC-limited bandwidth (f_{RC}) can then be approximated as

$$f_{RC} = \frac{1}{2\pi(R_L + R_S)(C_J + C_P)}. \qquad (5)$$

In some cases, junction resistance and series inductance can also be included to improve the model [11,16].

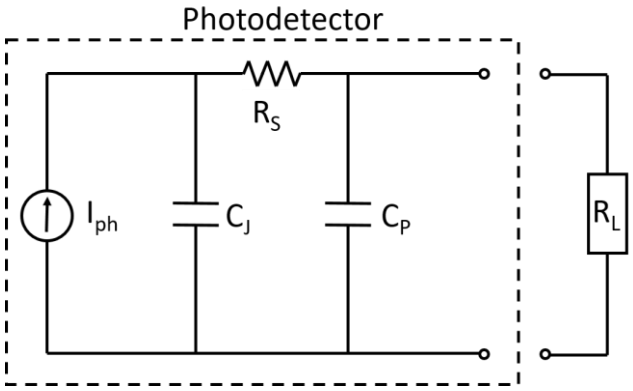

Figure 1.7. Equivalent circuit of a photodetector.

1.4 Preview of the dissertation

This dissertation focuses on the work on III-nitride optoelectronic devices—visible light-emitting diodes (LEDs) and photodetectors. Hence, after introducing the basics of LEDs and photodetectors in this chapter, the dissertation is separated into two main parts (Chapter 2 and Chapter 3). Chapter 2 will focus on the InGaN-based photodetectors. Specifically, it will discuss the efforts in understanding and improving the speed performance of the photodetectors. Chapter 3 will cover the work on the *c*-plane InGaN/GaN LEDs with an emphasis on the reduction of the internal electric field through doped barriers. It will cover the growth optimization that aims to minimize the detrimental impact of the doped barriers while maintaining small internal electric fields in the *c*-plane QWs. Results of low efficiency droop LEDs with thick SQW and doped barriers will be discussed. Experimental results from biased photocurrent spectroscopy and differential carrier lifetime measurements will be examined to understand the effects of the doped barriers on the internal electric fields and the recombination coefficients of the LEDs.

References:

1. O. Ambacher, J. Majewski, C. Miskys, A. Link, M. Hermann, M. Eickhoff, M. Stutzmann, F. Bernardini, V. Fiorentini, V. Tilak, B. Schaff, and L. F. Eastman, "Pyroelectric properties of Al(In)GaN/GaN hetero- and quantum well structures," J. Phys. Condens. Matter **14**, 3399–3434 (2002).

2. J. Lähnemann, O. Brandt, U. Jahn, C. Pfüller, C. Roder, P. Dogan, F. Grosse, A. Belabbes, F. Bechstedt, A. Trampert, and L. Geelhaar, "Direct experimental determination of the spontaneous polarization of GaN," Phys. Rev. B **86**, 81302 (2012).

3. M. R. Krames, O. B. Shchekin, R. Mueller-Mach, G. O. Mueller, L. Zhou, G. Harbers, and M. G. Craford, "Status and Future of High-Power Light-Emitting Diodes for Solid-State Lighting," J. Disp. Technol. **3**, 160–175 (2007).

4. J. M. Phillips, M. E. Coltrin, M. H. Crawford, A. J. Fischer, M. R. Krames, R. Mueller-Mach, G. O. Mueller, Y. Ohno, L. E. S. Rohwer, J. A. Simmons, and J. Y. Tsao, "Research challenges to ultra-efficient inorganic solid-state lighting," Laser \& Photonics Rev. **1**, 307–333 (2007).

5. E. Kioupakis, Q. Yan, and C. G. de Walle, "Interplay of polarization fields and Auger recombination in the efficiency droop of nitride light-emitting diodes," Appl. Phys. Lett. **101**, 231107 (2012).

6. A. David, N. G. Young, C. Lund, and M. D. Craven, "Review —The Physics of Recombinations in III-Nitride Emitters," ECS J. Solid State Sci. Technol. **9**, 16021 (2020).

7. A. David, C. A. Hurni, N. G. Young, and M. D. Craven, "Field-assisted Shockley-Read-Hall recombinations in III-nitride quantum wells," Appl. Phys. Lett. **111**, 233501 (2017).

8. A. David, N. G. Young, C. Lund, and M. D. Craven, "Compensation between radiative and Auger recombinations in III-nitrides: The scaling law of separated-wavefunction recombinations," Appl. Phys. Lett. **115**, 193502 (2019).

9. A. David and M. J. Grundmann, "Influence of polarization fields on carrier lifetime and recombination rates in InGaN-based light-emitting diodes," Appl. Phys. Lett. **97**, 33501 (2010).

10. G. Lucovsky, R. F. Schwarz, and R. B. Emmons, "Transit-Time Considerations in p—i—n Diodes," J. Appl. Phys. **35**, 622–628 (1964).

11. J. Bowers and C. Burrus, "Ultrawide-band long-wavelength p-i-n photodetectors," J. Light. Technol. **5**, 1339–1350 (1987).

12. E. Bellotti and F. Bertazzi, "Transport Parameters for Electrons and Holes," in *Nitride Semiconductor Devices: Principles and Simulation* (John Wiley & Sons, Ltd, 2007), pp. 69–93.

13. D. Ji, B. Ercan, and S. Chowdhury, "Experimental Determination of Velocity-Field

Characteristic of Holes in GaN," IEEE Electron Device Lett. **41**, 23–25 (2020).

14. H. Schneider and K. v. Klitzing, "Thermionic emission and Gaussian transport of holes in a GaAs/$Al_xGa_{1-x}As$ multiple-quantum-well structure," Phys. Rev. B **38**, 6160–6165 (1988).

15. A. M. Fox, D. A. B. Miller, G. Livescu, J. E. Cunningham, and W. Y. Jan, "Quantum well carrier sweep out: relation to electroabsorption and exciton saturation," IEEE J. Quantum Electron. **27**, 2281–2295 (1991).

16. Yih-Guei Wey, K. Giboney, J. Bowers, M. Rodwell, P. Silvestre, P. Thiagarajan, and G. Robinson, "110-GHz GaInAs/InP double heterostructure p-i-n photodetectors," J. Light. Technol. **13**, 1490–1499 (1995).

2

High-Speed InGaN-Based Photodetectors

2.1 Background and motivation

Visible light communication (VLC) has garnered significant interest in recent years as it offers a solution to the impending capacity crunch problem in the congested radio frequency (RF) spectrum [1–3]. VLC refers to short-range optical wireless communication (OWC) that uses visible light spectrum from 380 nm to 780 nm [4]. In a VLC link, data is transmitted by intensity modulating optical sources, such as light-emitting diodes (LEDs) and laser diodes (LDs). Due to the widespread adoption of solid-state lighting (SSL)-based illumination, VLC has the ability to provide communication in conjunction with illumination. Nitride LEDs and LDs have demonstrated modulation bandwidths as high as 1.5 GHz and 6.8 GHz respectively [5,6]. By using modulation schemes like orthogonal frequency division multiplexing (OFDM), data transmission rates of 7.9 Gb/s and 17.6 Gb/s have been achieved by using a violet micro-LED and a blue LD respectively [7,8]. In addition to the high-speed link, some of the potential applications of VLC are vehicular communication, underwater communication, and indoor positioning [9].

The rapid advancements of VLC have created demand for high-speed and high-performance optical receivers in the visible light spectrum. The optical receivers in most VLC links are mostly photodiodes and image sensors. Image sensors such as charge-coupled device (CCD) and complementary metal oxide semiconductor (CMOS) based sensors are only limited to applications that do not require high data rates due to their low number of frames per second rate (in the kHz range or lower). For high-speed VLC applications, silicon photodetectors (PIN photodiode and avalanche photodiodes) are used. Depending on the design, their bandwidths range from tens of MHz to GHz. However, silicon photodetectors have some significant limitations especially at short wavelengths (<600 nm). Due to its narrow bandgap energy (1.1 eV), in order to stop undesired photons with longer wavelengths, high-pass optical filters are required [10]. This increases the cost and complexity of the detection system. Furthermore, its large absorption coefficient in the blue/UV region causes photogenerations to take place very near to the surface where carriers may be lost through surface state recombination. Due to these limitations, InGaN photodetectors have been considered as an alternative for the optical receiver of VLC links.

InGaN is a promising material for photodetectors, especially in the visible light spectrum. They have a direct bandgap (0.61-3.4 eV) that can be flexibly tuned over the spectral range from the UVA region to the infrared region. However, due to the degrading crystalline quality of InGaN at high indium composition, the detection edges of most InGaN photodiodes are in the violet/blue region. Nonetheless, for VLC links using InGaN-based LEDs and lasers, the wavelengths of interest coincide with the available detection range of a typical InGaN photodiode (380 nm – 500 nm). The tunability also enables wavelength-selective response which improves the signal-to-noise ratio of the receiver without external filters. Due to the

wide bandgap, InGaN-based photodetectors also have a high breakdown voltage and a low intrinsic noise in comparison to the well-established silicon photodetectors [11]. Furthermore, their radiation hardness and high thermal stability allow them to operate under harsh conditions (e.g. outer space, underwater, etc.) [12].

2.2 Progress in III-nitride photodetectors

2.2.1 AlGaN-based and GaN-based photodetectors

Earlier studies on III-nitride photodetectors mainly focused on (AlGaN or GaN-based) UV photodetectors owing to their application in the areas of military, medicine, environment, and biology. Different types of photodetector structures have been developed, such as photoconductor, Schottky barrier, metal-semiconductor-metal (MSM), metal-insulator-semiconductor (MIS), *p-n* junction, and *p-i-n* junction [13,14,23–25,15–22]

Basic photodetector structures like the photoconductors have been fabricated using AlGaN and GaN layers [14–16]. They showed abnormally high responsivity (>100 A/W) due to the strong persistent photoconductivity (PPC). PPC is photo-induced conductivity that persists after the termination of light excitation. This effect is the consequence of deep level impurities in the material [26,27]. Due to the PPC effects, the photodetectors show extremely slow temporal response and are unsuitable for real applications.

The Schottky-type photodetectors like the Schottky barrier photodetectors and MSM photodetectors, where metals with high work function are used, exhibit faster speed and little PPC effect. RC-limited Schottky barrier UV photodetectors by using n-GaN layers showed a decay time of 118 ns at 337 nm and a peak responsivity of 0.18 A/W [17]. In an AlGaN-based implementation of this structure, a decay time of 14 ns was obtained [18]. MSM UV photodetectors fabricated on GaN exhibited a rise time of 28 ps at 267 nm with a gap spacing of 2 μm [19]. A bandwidth of 3.8 GHz was obtained by fast-Fourier transform (FFT). The photodetectors are transit-time limited owing to the slower drift velocity of the holes in GaN. Picosecond response (3.5 ps FWHM) at 360 nm was obtained when the spacing of metal

fingers was further reduced to 1 μm [20]. AlGaN MSM photodetectors were also demonstrated. The best device showed a pulse width of 76 ps and a bandwidth of 5.4 GHz (obtained by FFT) [21].

With the development of doping in p-GaN and p-AlGaN, *p-i-n* structure UV photodetectors were also fabricated. GaN-based *p-i-n* photodetectors with a rise time of 29 ns at 267 nm was demonstrated. Faster speed was observed by eliminating the low diffusion process in the absorbing p-GaN when the p-GaN layer was replaced by a p-AlGaN layer [22]. By using laterally epitaxially overgrown GaN, the dislocation density of GaN was greatly reduced where lower leakage current and a decay time of 4.5 ns were observed [21]. *p-i-n* UV photodetectors in the GHz regime were also reported. GaN-based *p-i-n* photodetectors with a bandwidth of 1.4 GHz and AlGaN-based *p-i-n* photodetectors with a bandwidth of 1.65 GHz were demonstrated [19,28].

Similar to III-V photodetectors, low-temperature-grown GaN photodetectors also exhibited very high frequency response by trading off responsivity. MSM photodetectors fabricated on LTG-GaN has reported a pulse width of 1.4 ps at 3 V bias [24]. The plasma induced MBE grown GaN exhibits a sub-picosecond carrier lifetime due to the high concentration of defects in the material. The same group also integrated both LTG-GaN photodetectors and MESFET on the same chip. The photoresponse transient of the photodetectors is amplified by the MESFET device. The electrical pulse produced by the photodetectors is as short as 0.9 ps but it is widened to 4 ps after being amplified by the MESFET. The fast Fourier transform of the resulting response is 55 GHz [25].

2.2.2 InGaN-based photodetectors

InGaN-based photodetectors were fabricated to extend the spectral photodetection range of nitrides to the UVA/visible range. Few studies have been reported on InGaN photodetectors due to the difficulty in growing high-quality InGaN films, especially with high indium composition. InGaN-based MSM photodetectors aiming at the short-wavelength range of visible light were fabricated and showed a responsivity of 0.1 A/W [29]. Fast response on the order of 10 ns was reported but with very small pulse amplitude (which corresponds to a 10^{-4} A/W responsivity).

InGaN-based photodetectors suffer from large leakage current and it is difficult to obtain high quality Schottky contacts due to high density surface defects [30,31]. Many groups use the metal-insulator-semiconductor structure to reduce the leakage current. The added layer of insulator increases the effective barrier height which, in turn, reduces the leakage current. Si_3N_4, CaF_2, Al_2O_3 layers have been chosen as the insulator layer by various groups [32–34]. The frequency response of these devices is not reported except for the photodetectors with CaF_2 layer which showed a rising time of 747 μs [32].

InGaN/GaN *p-i-n* photodetectors were also fabricated. Their responsivities range from 0.1 A/W to 0.2 A/W with external quantum efficiency as high as 67% [35–37]. However, bad material quality often plagues their performance. InGaN layers exhibit problems such as alloy segregation and clustering which worsens as indium content and layer thickness increase [38,39].

Due to the difficulty of growing a thick InGaN layer with a high crystalline quality, several groups also fabricated GaN/InGaN multi-quantum-well (MQW) photodetectors as an

alternative to bulk-based devices [40–49]. This design offers significant advantages in growth as it avoids strain-induced morphological instability and suppresses the formation of V-defects which act as leakage pathways. Some additional advantages of this structure include a more abrupt detection edge, extra flexibility in tuning the detection edge by adjusting well thickness, and easy integration of emitter and detector structures [10,12]. Initial studies on InGaN photodetectors focused on the characteristics of quantum efficiency and reduction of dark current. A study has shown that collection efficiency can be significantly reduced for QWs located outside the space charge region (SCR) [42]. Bias conditions and proper design of the photodetector structure like thinner quantum barriers are needed to improve the responsivity [43].

Due to the rising popularity of VLC, dynamic characteristics of the InGaN photodetectors have also been studied. An InGaN/GaN MQW photodetector with a bandwidth of 300 MHz was obtained. However, it was obtained by using a (less accurate) noise figure technique due to the lack of a modulated laser source [44]. In recent years, InGaN/GaN MQW photodetectors have been integrated with LED and laser diodes [45,46]. In one case, MQW photodetectors and laser diodes sharing the same active region were grown on a semipolar GaN substrate and processed into two distinct components. The photodetectors demonstrated a bandwidth of 230 MHz but a relatively low responsivity (0.05 A/W) [46]. The 3-dB bandwidths of InGaN/GaN MQW photodetectors range only from tens to hundreds of MHz (60 MHz- 350 MHz) [45–51] which are lower than the bandwidths of most commercially available high-speed silicon photodetectors which are in the GHz range. Nonetheless, there is hope that with more efforts investing in high-speed InGaN-based photodetectors due to the

recent interest in VLC, the challenges faced by InGaN-based photodetectors can be better understood and overcome.

2.3 Epitaxial structure and fabrication

We focused on InGaN/GaN multiple quantum well (MQW) photodetectors. Although InGaN has a large absorption coefficient near the band edge (~10^5 cm^{-1}) [52], hundreds of nanometers of InGaN are still required for full absorption. Since degradation of InGaN at high indium compositions starts after only a few nanometers of InGaN growth, a MQW active region design offers significant advantages in growth. In particular, the MQW structure enables different growth conditions for quantum wells (QWs) and quantum barriers (QBs). In general, GaN QBs are usually grown at temperature higher than the QW growth temperature to improve the surface adatom mobility and improve the crystal quality of the layers. However, immediately increasing the growth temperature after the QW growth can cause indium desorption of the QW. Two-step growth is applied when growing the GaN QBs. The first 2 nm GaN layer of the QB is grown at the same temperature as the QW before increasing the temperature (+40 ^oC) for the subsequent QB growth. This limits the formation of V-defects [53,54], which, in turn, reduces the dark current.

The InGaN/GaN MQW photodetectors were grown by metalorganic chemical vapor deposition (MOCVD) on *c*-plane sapphire substrates. The epitaxial structure (Figure 2.1(a)) consisted of a 1.2 μm un-intentionally doped (UID) GaN template layer and a 4.8 μm Si-doped n-GaN, followed by a 14 nm highly Si-doped n^+-GaN layer. The intrinsic active region consisted of an undoped $In_{0.14}Ga_{0.86}N$ MQW with 6 periods of alternating 2.5 nm QWs and 18 nm QBs. Above the active region was a 23 nm highly Mg-doped p^+-$Al_{0.1}Ga_{0.9}N$ layer, followed by a 100 nm moderately doped Mg-doped p-GaN layer and a 17 nm highly Mg-doped p^{++}-GaN contact layer. The highly doped layers sandwiching the active region were used to improve carrier collection [55]. Furthermore, the AlGaN layer on top of the MQW structure

was used to suppress the dark current by hindering the minority carrier transport in the p-type region [56].

Following the MOCVD growth, the wafers were fabricated into photodetectors with different mesa areas ranging from 20×20 μm^2 to 100×100 μm^2. The devices are designed for front illumination through the p-side. First, a 110 nm layer of indium tin oxide (ITO) was deposited by electron-beam evaporation to form a transparent p-contact. Square mesas were then defined by reactive-ion etching the ITO and the epitaxial layers to reach the n-GaN layer. After that, a dielectric stack composed of silicon dioxide and aluminum oxide was deposited using ion beam deposition as a metal isolation layer. A 50 nm layer of silicon dioxide was then blanket deposited using atomic-layer deposition (ALD) for sidewall passivation [57]. After via opening, common Al/Ni/Au n- and p-metal contacts were deposited by electron-beam evaporation. The fabricated photodetectors are shown in Figure 2.1(b).

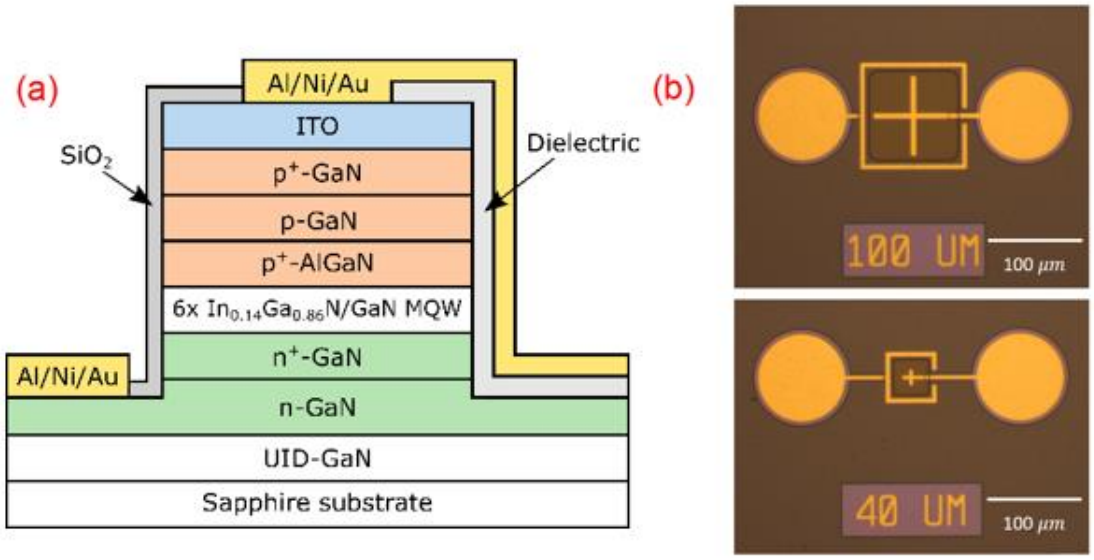

Figure 2.1. (a) Schematic of the front illuminated InGaN/GaN MQW photodetector. (b) Optical images of devices with 100×100 μm^2 and 40×40 μm^2 mesa sizes.

2.4 Characterization

External quantum efficiency (EQE) of the photodetectors is an important quantity to characterize the devices. It measures the efficiency of the conversion process of received photons to charge carriers that can be collected. It is defined by

$$\eta_{EQE} = \frac{Number\ of\ collected\ electrons\ at\ detector\ terminals}{Number\ of\ incident\ photons} = \frac{I_{ph}/q}{P_o/h\nu} \qquad (1)$$

where I_{ph}, q, P_o, and $h\nu$ are the photocurrent generated, electron charge, incident optical power, and energy of the photon, respectively.

Another quantity frequently used to characterize photodetectors is responsivity (R) which characterizes the device performance in terms of the photocurrent generated per incident optical power. Responsivity is related to EQE by the following equation

$$R = \eta_{EQE}\frac{q}{h\nu}. \qquad (2)$$

Figure 2.2 shows the schematic of the setup to measure the EQE and responsivity of the photodetectors. An Oriel 300 W Xe lamp with an Oriel 260 monochromator was used as the light source. The spectral flux of the light source was measured separately with a calibrated silicon photodetector. Our fabricated devices were designed for front illumination. They also have small sizes in order to minimize the RC time constant. To effectively couple light into the small devices, a lensed fiber (with a focused beam diameter of around 50 μm) was used. The photocurrent of the photodetectors was then measured by a source meter (Keithley 2400) as functions of the wavelength of the incident light and the applied voltages. Figure 2.3(a)(b) shows the J-V curves and the measured responsivity of an InGaN MQW photodetector, respectively.

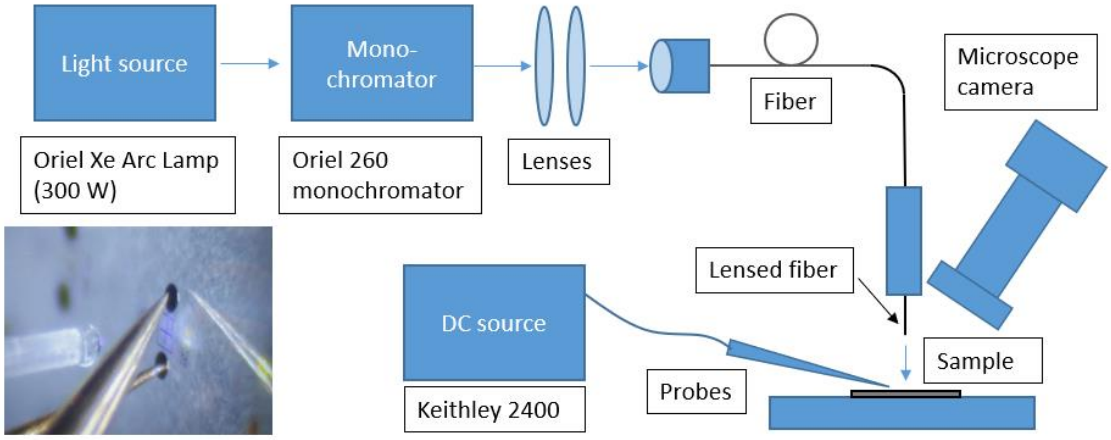

Figure 2.2. Schematic of the EQE measurement setup.

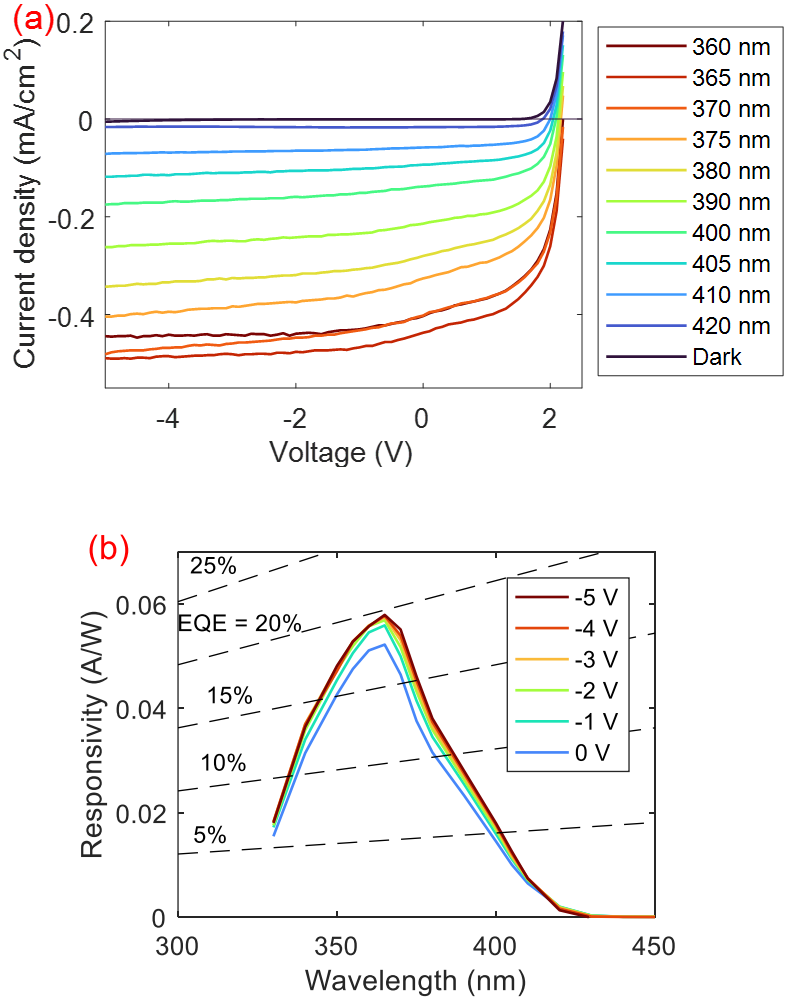

Figure 2.3. (a) Dark and illuminated J-V curves, (b) spectral response and EQE of an InGaN MQW photodetector with varying applied voltages.

The optical-to-electrical (O-E) frequency response of the photodetectors was also measured. Figure 2.4 presents the schematic of the frequency response measurement setup. A commercial III-nitride laser diode was used as the excitation source. Figure 2.5 shows the frequency response of the laser diode which was measured separately by using a high-speed silicon photodetector (UPD-50-UP) with a 5-GHz 3-dB bandwidth. At an injection current of

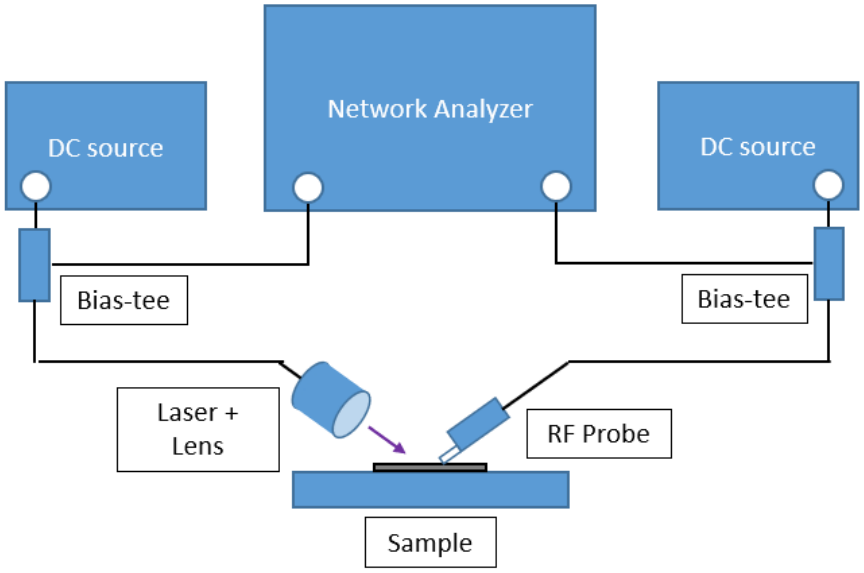

Figure 2.4. The RF setup for measuring the frequency response of the photodetectors.

19 mA, the frequency of the laser diode is flat below 1 GHz which is sufficient for the

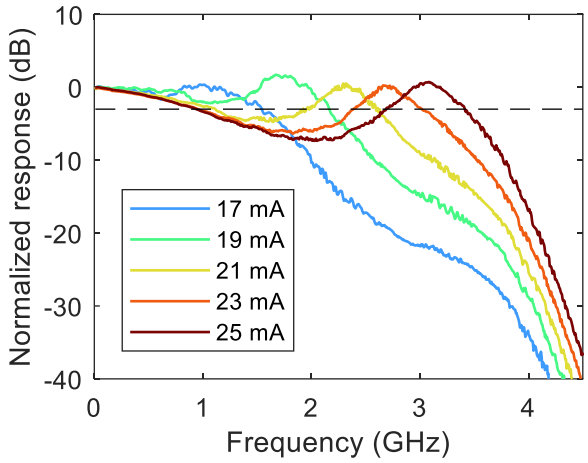

Figure 2.5. The frequency response of the commercial III-nitride laser diode (excitation source).

frequency response of the photodetectors in our studies which have fairly low 3-dB bandwidths (<1 GHz).

During the measurement, the laser diode was modulated by a small signal from a network analyzer (PNA-X N5247A). The modulated light was detected by the photodetector which was also linked to the network analyzer through a RF micro-probe (ACP40-GS-250). The small signal frequency was swept from 10 MHz to 1 GHz. Figure 2.6 shows a typical frequency response of an InGaN/GaN MQW photodetector. The 3-dB bandwidth, which is the frequency at which the signal amplitude reduces by half its value, can then be determined.

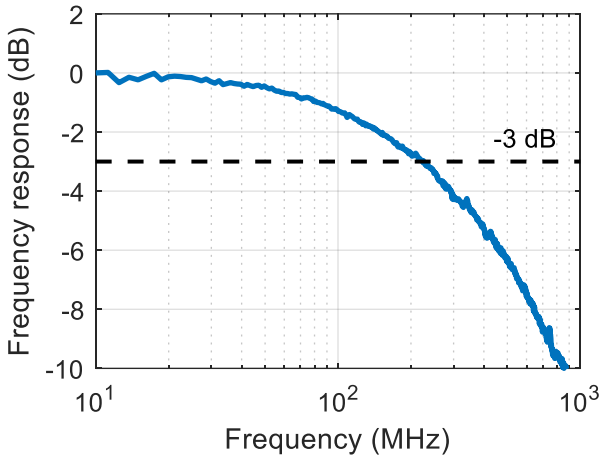

Figure 2.6. The normalized frequency response of an InGaN/GaN MQW photodetector.

2.5 Speed improvement through reduction of quantum barrier thickness

In general, the bandwidths of most *p-i-n* photodetectors are limited by both RC time constant or/and carrier transit time. For photodetectors (PDs) with a multiple quantum well (MQW) active region design, since electron and hole pairs are generated in the quantum well, they have to escape from the wells first before drifting to the collecting electrodes. As a result, on top of the usual RC time constant and carrier transit time, MQW PDs can also be potentially limited by the carrier escape lifetimes. In literature, it has been reported lower than expected bandwidths were observed in Ge/SiGe MQW PDs due to carrier trapping [58]. Since III-nitride materials have a wider bandgap, their conduction band and valence band offsets are also much larger than that of narrow bandgap materials such as Ge and Si. As such, carrier trapping might be more severe for InGaN/GaN MQW PDs.

In this study, we demonstrated that reducing the quantum barrier (QB) thicknesses in the InGaN/GaN MQW structures improved the 3-dB bandwidth by decreasing the carrier escape lifetimes. To this end, InGaN/GaN MQW epitaxial structures with varying QB thicknesses were grown and fabricated into PDs with different device sizes. Following that, we reported the responsivity, dark current, and frequency response for the thickness series. Simulations were performed to calculate the carrier escape lifetimes due to carrier trapping in the QWs. The carrier escape lifetimes of the PDs were also extracted by considering the combined effects of the RC response, carrier trapping, and transit time to explain the observed trends.

Three InGaN/GaN MQW epitaxial structures with varying GaN QB thicknesses were grown by metalorganic chemical vapor deposition (MOCVD) on *c*-plane sapphire substrates

(Figure 2.7(a)). The structure began with a 1.2 μm unintentionally doped (UID) GaN template layer and a 4.8 μm Si-doped n-GaN ([Si] = 5×10^{18} cm^{-3}), followed by a 14 nm highly Si-doped n+-GaN layer ([Si] = 1×10^{19} cm^{-3}). Then, an active region was grown, consisting of a 6 period UID InGaN/GaN MQW with 2.5 nm $In_{0.14}Ga_{0.86}N$ QW. The GaN QB thicknesses were varied: 18 nm, 13.5 nm, and 9.5 nm in PD-A, PD-B, and PD-C, respectively. Above the active region was a 23 nm highly Mg-doped p+-$Al_{0.1}Ga_{0.9}N$ layer ([Mg] = 1.5×10^{20} cm^{-3}), followed by a 100 nm moderately doped Mg-doped p-GaN layer ([Mg] = 2×10^{19} cm^{-3}) and a 17 nm highly Mg-doped p+-GaN contact layer ([Mg] = 1.5×10^{20} cm^{-3}).

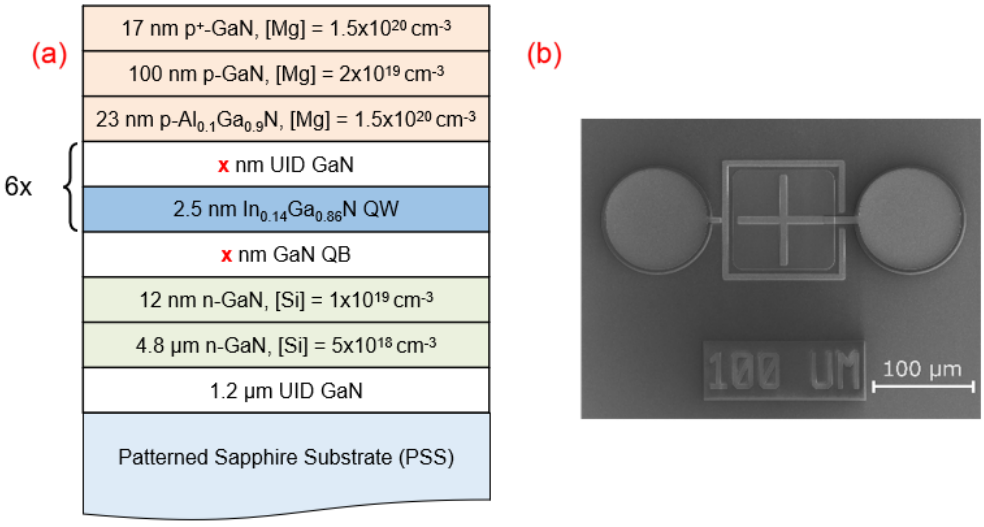

Figure 2.7. (a) Schematic of the photodetector epitaxial structure. (b) Top-view SEM image of a 100×100 μm^2 device.

2.5.1 Responsivity and 3-dB bandwidth

The measured spectral response and EQE of PD-A, PD-B, and PD-C at -4 V are shown in Figure 2.8(a). Measurements were taken on PDs of size 100×100 μm^2 but the results are representative of PDs with different device sizes. The spectral response and EQE of all three devices were found to peak at around 365 nm. The peak EQE increases with the thickness of

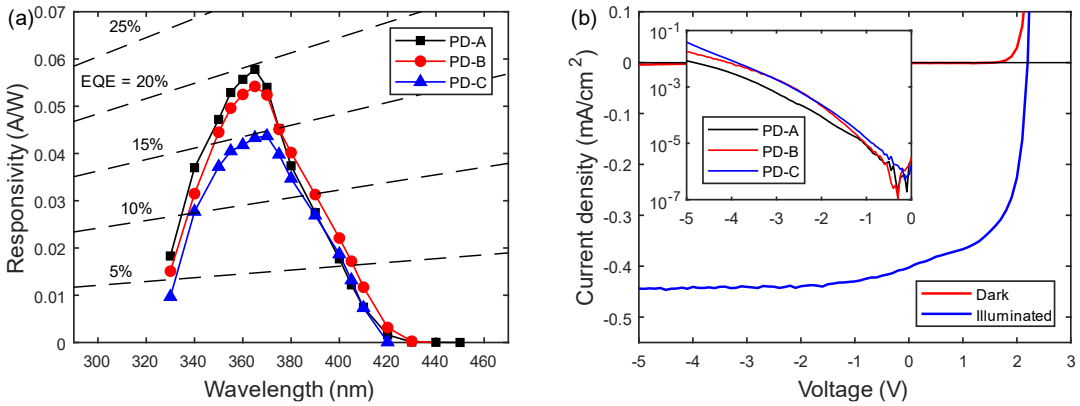

Figure 2.8. (a) Spectral response and EQE of PD-A, PD-B, and PD-C of size 100×100 μm^2 at -4 V. (b) Dark and illuminated (360 nm) J-V curves of PD-A of size 100×100 μm^2. Inset: J-V curves for PD-A, PD-B, and PD-C under dark condition.

the GaN QBs, as they contribute to the absorption. At >380 nm, all devices show similar spectral response and EQE since they have the same total thickness of the InGaN layers and the absorption mostly occurs in the QWs. The slightly higher responsivity of PD-B in this range is likely due to the small variations in thickness and/or indium composition in the QW layers across the samples. Representative dark and illuminated current density versus applied voltage (J-V) curves for PD-A are shown in Figure 2.8(b). Under illumination, photocurrent saturation corresponding to maximized IQE occurs at a reverse bias as low as -1 V, indicating excellent carrier collection. The inset of Figure 2.8(b) shows the dark current density of all 3 devices of size 100×100 μm^2. The dark current (density) ranges from 1 pA to 4 nA (1×10^{-5} to 4×10^{-2} mA/cm^2) with a bias from -1 V to -5 V. The devices with thinner QBs have slightly larger dark current due to higher thermionic emission or tunneling rates as well as the poorer crystalline quality of the active region.

Figure 2.9(a) shows the frequency response of various device sizes for PD-C at -6 V. The 3-dB bandwidths of the PDs increase with decreasing device sizes due to the smaller RC time constant. Similar bandwidth dependence on device size was observed for PD-A and PD-

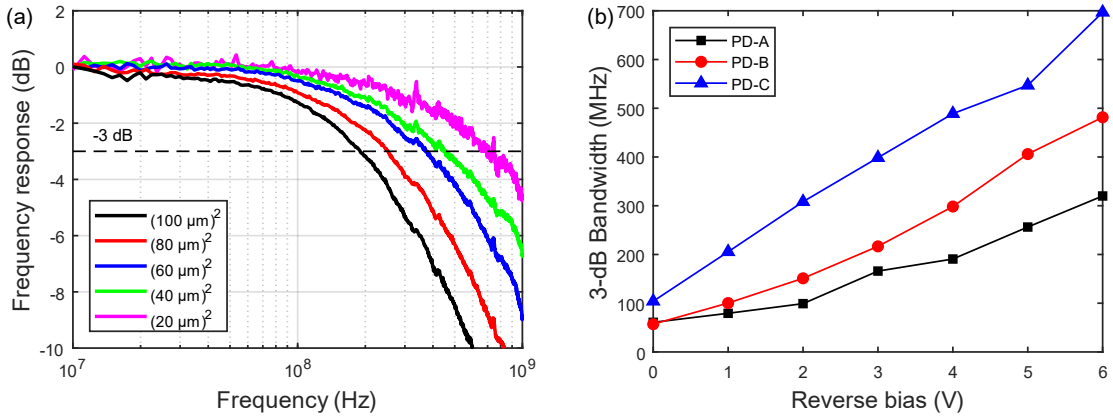

Figure 2.9. (a) O-E frequency response of PD-C of various device sizes at -6 V. (b) 3-dB bandwidth versus applied bias of PD-A, PD-B, and PD-C of size 20×20 μm^2.

B. The bias dependent 3-dB bandwidths for PD-A, PD-B, and PD-C of size 20×20 μm^2 are plotted in Figure 2.9(b) showing that the bandwidths increase as the reverse bias increases from 0 V to -6 V. Furthermore, PDs with thinner QBs achieve higher bandwidths under the same bias voltages. At -6 V, the bandwidth of PD-C is more than double the bandwidth of PD-A. Finally, we note that the highest measured 3-dB bandwidth is 700 MHz for the smallest device (20×20 μm^2) with the thinnest QBs (9.5 nm) under a reverse bias of -6 V.

2.5.2 Speed limitations

Various speed limiting factors are considered to understand the dependence of bandwidth on applied bias and QB thickness. Under the illumination of a 405 nm light source, electron-hole pairs are photogenerated in the InGaN QWs. These carriers either escape the wells and contribute to the photocurrent or are lost through recombination. The possible escape mechanisms of the carriers include tunneling through the barrier and thermionic emission over the barrier. Once escaped, the electrons and holes drift in opposite directions with respective drift velocities to the collecting electrodes. Electric fields in the GaN QB region are usually in

excess of hundreds of kV/cm at moderate reverse bias. Due to these high electric fields in the QB region, carriers travel at velocities close to their saturation velocities (1.25×10^7 cm/s and 6.63×10^6 cm/s for electron and hole respectively) [59,60]. Therefore, apart from the RC time constant, the bandwidth of an MQW PDs also depends on the carrier escape lifetimes (tunneling or thermionic emission) and the transit time of the carriers through the depletion region.

For our structures, due to the thin depletion region, the transit-time-limited bandwidths (f_{Tr}) are calculated to be hundreds of GHz (>300 GHz). Assuming uniform illumination, the equation used is $f_{Tr} = 0.67v_p/L$ where v_p and L are hole saturation velocity and active layer thickness respectively [61,62]. Since the measured bandwidths (<1 GHz) are orders of magnitude lower than the calculated f_{Tr}, the PDs in this work are not limited by the transit time. In other words, even though the depletion widths for all three structures are different, the calculated transit times are too small compared to other limiting lifetimes to explain the differing bandwidths.

We now consider the carrier escape lifetimes. Photogenerated carriers can escape from the quantum well either through tunneling or thermionic emission. Lifetime for tunneling (τ_T) can be estimated through a WKB-approximation by using the following equation [63]:

$$\frac{1}{\tau_T} = \frac{n\pi\hbar}{2L_w^2 m^*} \exp \int_0^{L_b} -2\sqrt{\frac{2m^*\left(E_{c,v}(x) - E_n\right)}{\hbar^2}}\,dx \qquad (3)$$

where m^* is the electron/hole mass, L_w and L_b are QW and QB thickness, respectively, E_n is the nth eigenvalue in the QW, and $E_{c,v}$ is the conductive/valence band.

Thermionic emission lifetime (τ_{TE}) is given by

$$\frac{1}{\tau_{TE}} = \left(\frac{k_B T}{2\pi m^* L_w^2}\right)^{\frac{1}{2}} \exp\left(-\frac{E_{c,v} - E_n}{k_B T}\right) \quad (4)$$

where k_B is Boltzmann's constant and T is the temperature. For both lifetimes, we only consider the carriers escaping from the lowest energy bound state (E_1), which represent the worst-case scenario. To calculate both tunneling and thermionic emission lifetimes, band diagrams of the devices have to be computed. Simulations were performed by using a self-consistent Schrödinger-Poisson drift-diffusion solver [64,65]. Our calculations used full theoretical polarization values and a conduction-to-valence-band offset ratio of 0.63:0.37 [66–68]. The electric field, band profile, and quantum-confined eigenstates of the three structures at different bias voltages were determined.

Figure 2.10 presents the simulated electric field profiles of PD-A and PD-C under a reverse bias of -4 V. The net electric fields in the QWs are negative due to the large polarization-induced electric fields which are in the opposite direction of the *p*-*n* junction electric field (defined as positive). Since PD-C has a smaller depletion width, which is mainly determined by the thickness of the UID active region, built-in and applied potentials are

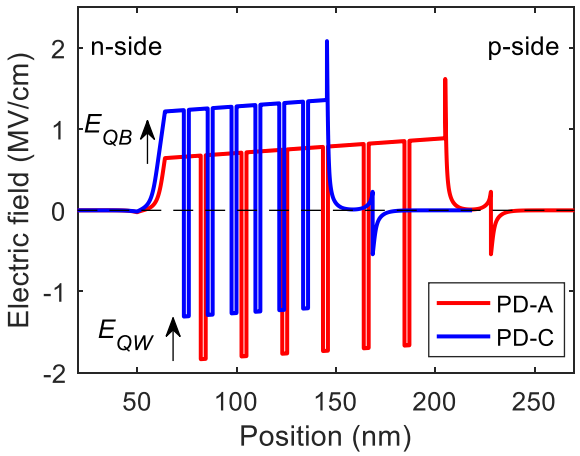

Figure 2.10. Simulated electric field profiles of PD-A and PD-C at -4 V (positive electric fields point toward the growth surface).

distributed over a smaller distance. Therefore, its electric fields are shifted in the positive direction, resulting in larger electric fields (E_{QB}) in the GaN QB region and smaller electric fields (E_{QW}) in the InGaN QW region. The difference in field strengths in PD-A and PD-C is around 0.5 MV/cm.

Due to the smaller electric fields in the QW, the barrier height (measured relative to the ground state) in PD-C is lower than that in PD-A under the same applied bias as shown in Figure 2.11(b). Note that the holes want to escape to the p-side (right). The probability of the carriers tunneling through the barrier depends on the height and width of the classically forbidden triangular barrier while the thermionic emission lifetime grows exponentially with the barrier height. Since both tunneling and thermionic emission lifetimes decrease with decreasing barrier height, devices with thinner QBs are expected to have smaller escape lifetimes (both tunneling and thermionic emission lifetimes).

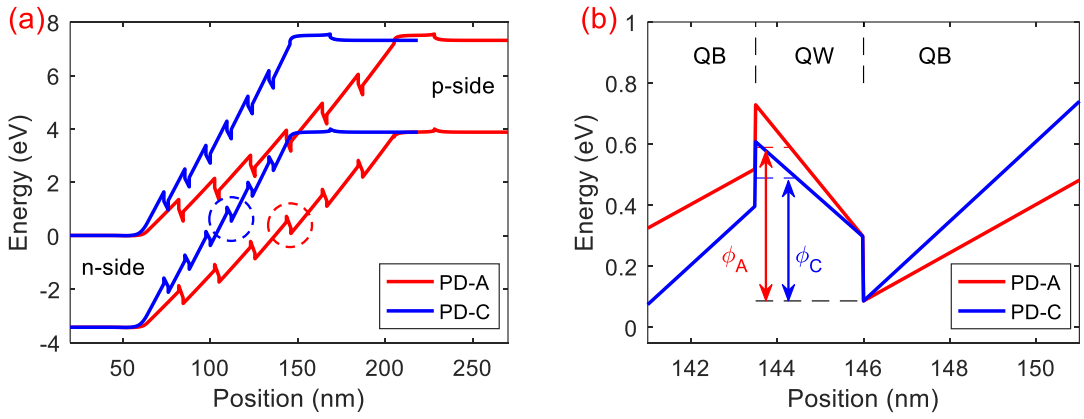

Figure 2.11. (a) Band diagrams of PD-A and PD-C at -4 V. The circles show the part of the valence band edges shown in (b). (b) Valence band edges near a QW in PD-A and PD-C at -4 V. The band edges are drawn superimposed for comparison. The holes drift to the right (p-side) after escaping from the QW. The barrier heights (measured relative to the ground state) in PD-A and PD-C ($\phi_{\text{PD-A/C}}$) are shown in the figure.

The simulations up to this point used an ideal "tophat" function for the indium compositional profile in the QW. However, due to the compositional fluctuations in InGaN QW, the abrupt profile might not be realistic [69]. We used a Gaussian shape to describe the indium compositional profile [70,71]. The full width at half maximum (FWHM) of the Gaussian profile was set to be the QW thickness. Figure 2.12 compares the valence band edges of PD-A using the ideal "tophat" function and the Gaussian function. In the case of the Gaussian function, the band edges near the QW/QB heterointerfaces are less abrupt. The resulting smaller barrier height should lead to smaller carrier escape lifetimes (tunneling and thermionic emission) since they are functions of the barrier height. However, all the trends that we observed with decreasing QB thickness remain true.

The tunneling and thermionic emission lifetimes were calculated by Eq. 3 and Eq. 4 for electrons and heavy holes at 300 K. There are slight differences in the escape lifetimes from different QWs. The lifetimes, averaged over each quantum well, are plotted in Figure 2.13(a)(b). As shown by the figures, all escape lifetimes decrease with increasing reserve bias. Besides that, it is also shown that the dominant escape mechanisms for holes and electrons are

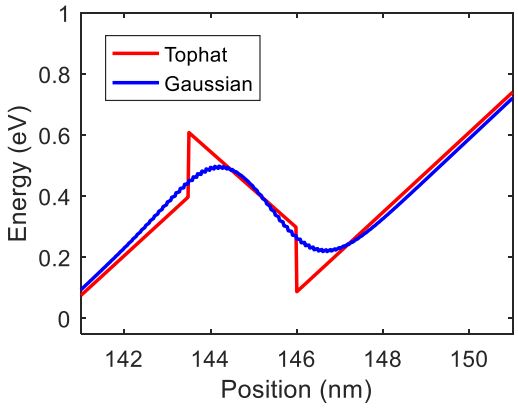

Figure 2.12. Simulated valence band edges near a QW in PD-A using "tophat" and Gaussian function for indium composition in the QW.

thermionic emission and tunneling respectively in the bias range of interest. More importantly, all escape lifetimes, regardless of carrier type and escape mechanism, are smaller for PDs with thinner QBs under the same bias voltages as expected.

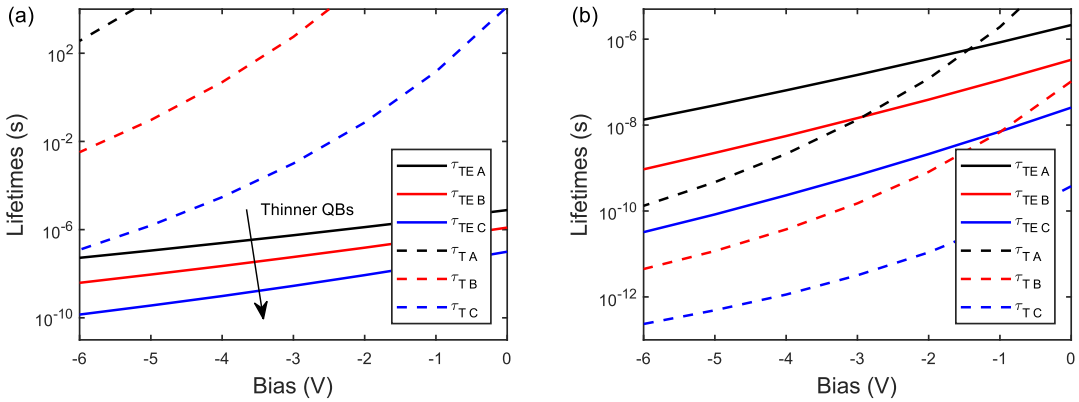

Figure 2.13. Simulated thermionic emission (TE) and tunneling (T) lifetimes as a function of applied bias for (a) holes (b) and electrons.

2.5.3 Experimental carrier escape lifetimes

Escape lifetimes were also extracted by fitting the frequency response of the PDs. The net frequency response is the product of the circuit transfer function (H_{ckt}) and the current source response (H_i) [72]. The PD is modeled as a lumped-element device with the equivalent circuit as shown in Figure 2.14(a). The characteristic impedance of the PD is given by:

$$Z(\omega) = R_S + j\omega L_S + \frac{R_d}{1 + j\omega R_d C_J} \qquad (5)$$

where R_S, C_J, R_d, and L_S are series resistance, junction capacitance, junction resistance, and series inductance, respectively. The circuit parameters were de-embedded from the electrical reflection (S_{22}) measurement. Figure 2.14(b-d) shows the impedance of PD-C of size 20×20 μm^2 on a Smith chart as well as its real and imaginary parts. The measured and modeled impedances were shown to be in good agreement. For this particular device, the extracted

circuit parameters are 2.7 Ω, 2.7 pF, 21 kΩ, and 2.0 nH for R_S, C_J, R_d, and L_S, respectively. The circuit transfer function of the PD is given by:

$$H_{ckt}(\omega) = \frac{1}{1 + (j\omega C_J + 1/R_d)(R_S + Z_L + j\omega L_S)} \tag{6}$$

where ω is the angular modulation frequency and Z_L is the 50 Ω load resistance. For a p-side illuminated *p-i-n* photodiode, the current-source response is given by:

$$H_i(\omega) = \frac{1}{1 - e^{-\alpha L}}\left[\left(\frac{1 - e^{-j\omega t_p - \alpha L}}{j\omega t_p + \alpha L} + e^{-\alpha L}\frac{e^{-j\omega t_p - 1}}{j\omega t_p}\right)\left(\frac{1}{1 + j\omega\tau_p}\right) + \left(\frac{1 - e^{-j\omega t_n}}{j\omega t_n} + e^{-\alpha L}\frac{1 - e^{\alpha L - j\omega t_n}}{\alpha L - j\omega t_n}\right)\left(\frac{1}{1 + j\omega\tau_n}\right)\right] \tag{7}$$

where α is the absorption coefficient, L is the absorption layer thickness, $t_{p(n)}$ is the hole (electron) transit time, and $\tau_{p(n)}$ is the hole (electron) escape lifetime [72,73]. As mentioned before, since transit time is very short (1-2 ps), its effect is negligible and $\omega t_{p(n)}$ goes to zero in the frequency range of interest. Additionally, we only extract the escape lifetimes at large reverse bias so we can ignore the electron escape lifetime which is orders of magnitude smaller than the hole escape lifetime ($\omega\tau_n \rightarrow 0$). The net frequency response expression ($H(\omega) = H_i H_{ckt}$) is then simplified to:

$$H(\omega) = \left[\left(\frac{1}{\alpha L} - \frac{e^{-\alpha L}}{1 - e^{-\alpha L}}\right)\left(\frac{1}{1 + j\omega\tau_p}\right) + \left(\frac{1}{1 - e^{\alpha L}} - \frac{1}{\alpha L}\right)\right]\left[\frac{1}{1 + (j\omega C_J + 1/R_d)(R_S + Z_L + j\omega L_S)}\right]. \tag{8}$$

Eq. 8 was then fitted to the measured frequency response of PDs using the nonlinear least-square method shows the measured and modeled frequency response of PD-C of size 20×20 μm^2 at -6 V. In the same figure, we plotted the frequency response only considering the

circuit transfer function which predicts a higher bandwidth. It shows that the carrier trapping effect cannot be ignored when modeling the frequency response.

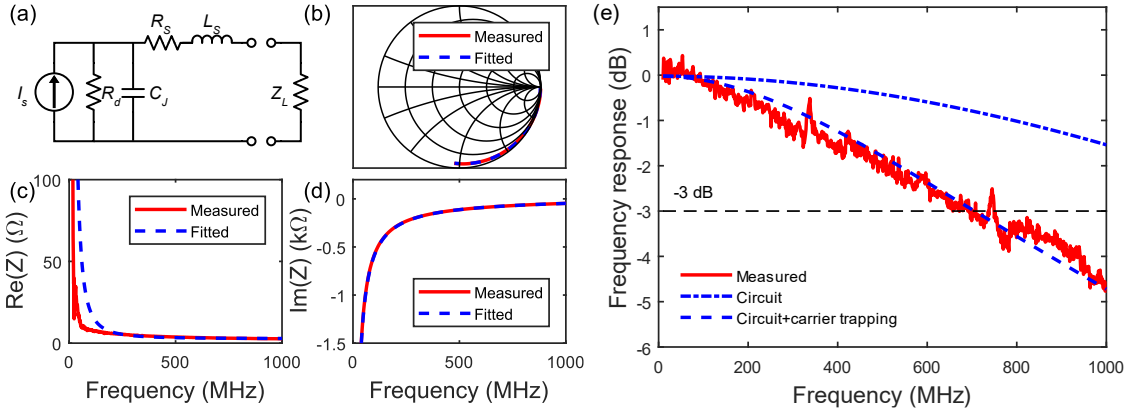

Figure 2.14. (a) Equivalent circuit of the photodetector. (b) Measured and modeled impedance of PD-C (20×20 μm^2) on Smith chart. (c)(d) The real and imaginary part of the impedance. (e) Measured and modeled frequency response of PD-C (20×20 μm^2) considering only the circuit transfer function (dash-dot line) and both circuit transfer function and carrier trapping effect (dashed line).

The fitted hole escape lifetimes of PD-A, PD-B, and PD-C with various sizes from -4 V to -6 V are shown in Figure 2.14(e). The extracted experimental hole escape lifetimes were found to be independent of device size. This was expected as escape lifetimes are only determined by the epitaxial structures and the bias voltages. They range from 0.3 ns to 1.5 ns at -4 V and 0.2 ns to 0.6 ns at -6 V. The simulated hole thermionic emission lifetimes that we obtained earlier are also shown in the same figure for comparison. In general, the experimental values are smaller than the simulated escape lifetimes. However, we emphasize that only carriers escaping from the lowest energy bound states were considered for the calculation of the simulated escape lifetimes. Therefore, they can be seen as the upper bound for the escape lifetimes. Nonetheless, similar to the simulated lifetimes, the experimental hole escape

lifetimes decrease with increasing reverse bias and, more importantly, with decreasing QB thicknesses. This explains the higher 3-dB bandwidths measured in PDs with thinner QBs.

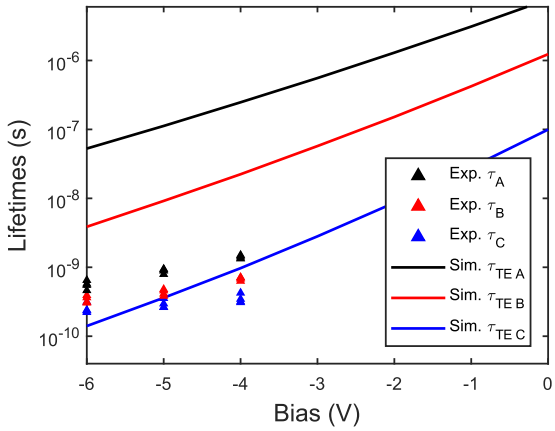

Figure 2.15. The extracted experimental hole escape lifetimes of PD-A, PD-B, and PD-C with different sizes (triangles). The simulated thermionic emission lifetimes for holes (from Fig. 2.13(a)) are also shown for comparison.

In conclusion, we demonstrated that reducing the thickness of QBs in InGaN/GaN MQW PDs leads to improved 3-dB bandwidths, going as high as 700 MHz. The large carrier escape lifetimes due to carrier trapping in the QWs significantly limit the bandwidth of the devices. Further device speed improvement efforts should reduce the carrier escape lifetimes to enable high-speed applications in VLC.

2.6 Future work

The work on InGaN/GaN MQW photodetectors shows that their bandwidths are limited by carrier escape lifetimes due to the carrier trapping in the QW. Further speed improvements of InGaN/GaN MQW photodetectors should be done by reducing the carrier escape lifetimes. We have shown that having a thinner depletion region via reducing the QB thickness helps to decrease the barrier height for the carriers to escape. Even though a similar effect can be achieved by increasing the reverse bias, it is preferable to operate the devices at a low bias to minimize the dark current (background noise) and power consumption. Further reduction of the QB thickness can improve the bandwidth but risks increasing the dark current. As mentioned in section 2.3, parts of the QBs were grown at an elevated temperature to restore the growth morphology following the low temperature InGaN QW growth. Further decreasing the QB thickness might start impacting its ability to protect the structural integrity of the MQW, leading to indium desorption in the QW and generation of V-defects.

Another way to obtain smaller depletion widths is by reducing the number of periods in the MQW at the expense of the efficiency of the devices. Figure 2.16 shows the electric field profiles and the band diagrams of the photodetectors with different numbers of QWs at a bias of -4 V. With decreasing QW number, the net electric field in the QW decreases. As a result, the effective barrier heights also decrease, decreasing the carrier escape lifetimes. To avoid sacrificing efficiency, side-illuminated waveguide structures can be used if normal-incidence is not required for the application [46,74].

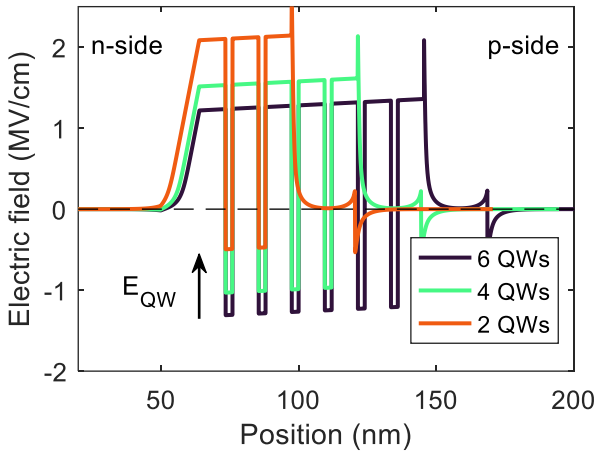

Figure 2.16. Simulated electric field profiles of PD-A and PD-C at -4 V (positive electric fields point toward the growth surface).

The large carrier escape lifetimes are primarily due to the large conduction and valence band offsets at the InGaN/GaN interfaces. Superlattice or compositional grading at each heterointerface is another way to eliminate carrier trapping effects although it leads to higher accumulative stress in the MQW structure [75].

Apart from the large band offsets, the devices, usually grown on *c*-plane substrates, also suffer from the polarization-induced electric fields in the QWs which oppose the *p*-*n* junction electric field. The resulting net electric field in the QW pushes the photogenerated carriers away from the barrier, resulting in a larger barrier height, thus larger escape lifetimes. To alleviate the effect of the polarization fields, devices can be grown on semipolar or nonpolar substrates to reduce or eliminate the polarization fields. Figure 2.17(a) shows the valence band edges of devices with *c*-plane and *m*-plane orientations. A significant reduction in the effective barrier height is observed. At certain orientations (e.g., $20\bar{2}1$ and $11\bar{2}2$), the polarization field switches direction and aids the carrier escape. The most extreme case is N-polar ($000\bar{1}$) oriented devices [76]. In N-polar photodetectors, assuming the same p-side up geometry, the

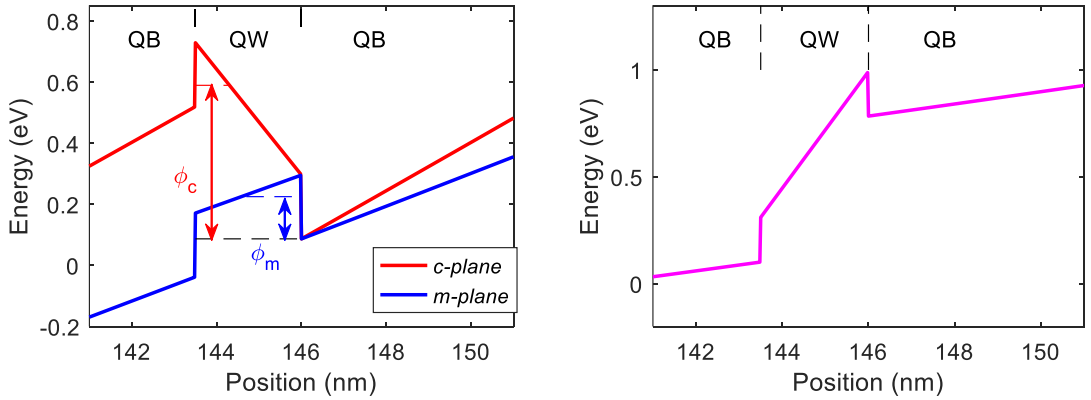

Figure 2.17. (a) Valence band edges of devices with *c*-plane and *m*-plane orientations. The band edges are drawn superimposed for comparison. (b) Valence band edge of a N-polar device.

polarization-induced electric fields in the QW are in the same direction as the *p*-*n* junction field. Figure 2.17(b) shows the valence band edge near a QW of a N-polar device. The ground state is not shown as it is difficult to calculate the eigenstates due to the low confinement of the QW as a result of the large electric field in the QW. Nonetheless, it is clear that there is minimal carrier trapping effect in N-polar devices compared to devices in other orientations.

2.7 Conclusion

In this work, InGaN/GaN multiple quantum well (MQW) samples were grown by MOCVD and fabricated into photodetector devices for high-speed applications in visible light communication (VLC). On top of the usual RC time constant and transit time, carrier trapping can be a speed limiting factor for MQW photodetectors. In order to improve the speed performance of the devices, quantum barrier (QB) thicknesses in the MQW structure were reduced. Simulations show that reducing the QB thickness indeed decreases both tunneling and thermionic lifetimes. The carrier escape lifetimes of the devices were also extracted to explain the observed experimental trend. A 3-dB bandwidth of 700 MHz was demonstrated with a reserve bias of -6 V for the InGaN/GaN MQW photodetectors with the thinnest quantum barriers. Additional approaches to further improve the device speed were also suggested.

References:

1. H. Haas, E. Sarbazi, H. Marshoud, and J. Fakidis, "Chapter 11 - Visible-light communications and light fidelity," in *Optical Fiber Telecommunications VII*, A. E. Willner, ed. (Academic Press, 2020), pp. 443–493.

2. H. Burchardt, N. Serafimovski, D. Tsonev, S. Videv, and H. Haas, "VLC: Beyond point-to-point communication," IEEE Commun. Mag. **52**, 98–105 (2014).

3. S. Rajbhandari, H. Chun, G. Faulkner, K. Cameron, A. V. N. Jalajakumari, R. Henderson, D. Tsonev, M. Ijaz, Z. Chen, H. Haas, E. Xie, J. J. D. McKendry, J. Herrnsdorf, E. Gu, M. D. Dawson, and D. O'Brien, "High-Speed Integrated Visible Light Communication System: Device Constraints and Design Considerations," IEEE J. Sel. Areas Commun. **33**, 1750–1757 (2015).

4. "IEEE Standard for Local and Metropolitan Area Networks--Part 15.7: Short-Range Wireless Optical Communication Using Visible Light," IEEE Std 802.15.7-2011 1–309 (2011).

5. A. Rashidi, M. Monavarian, A. Aragon, A. Rishinaramangalam, and D. Feezell, "Nonpolar *m*-Plane InGaN/GaN Micro-Scale Light-Emitting Diode With 1.5 GHz Modulation Bandwidth," IEEE Electron Device Lett. **39**, 520–523 (2018).

6. C. Lee, C. Shen, C. Cozzan, R. M. Farrell, S. Nakamura, A. Y. Alyamani, B. S. Ooi, J. E. Bowers, S. P. DenBaars, and J. S. Speck, "Semipolar GaN-based laser diodes for Gbit/s white lighting communication: devices to systems," in *Gallium Nitride Materials and Devices XIII*, J.-I. Chyi, H. Fujioka, and H. Morkoç, eds. (SPIE, 2018), Vol. 10532, pp. 121–131.

7. M. S. Islim, R. X. Ferreira, X. He, E. Xie, S. Videv, S. Viola, S. Watson, N. Bamiedakis, R. V Penty, I. H. White, A. E. Kelly, E. Gu, H. Haas, and M. D. Dawson, "Towards 10 Gb/s orthogonal frequency division multiplexing-based visible light communication using a GaN violet micro-LED," Photon. Res. **5**, A35--A43 (2017).

8. Y.-F. Huang, C.-T. Tsai, H.-Y. Kao, Y.-C. Chi, H.-Y. Wang, T.-T. Shih, and G.-R. Lin, "17.6-Gbps universal filtered multi-carrier encoding of GaN blue LD for visible light communication," in *2017 Conference on Lasers and Electro-Optics (CLEO)* (2017), pp. 1–2.

9. D. Karunatilaka, F. Zafar, V. Kalavally, and R. Parthiban, "LED Based Indoor Visible Light Communications: State of the Art," IEEE Commun. Surv. Tutorials **17**, 1649–1678 (2015).

10. F. Omnès, E. Monroy, E. Muñoz, and J.-L. Reverchon, "Wide bandgap UV photodetectors: a short review of devices and applications," in *Gallium Nitride Materials and Devices II*, H. Morkoc and C. W. Litton, eds. (SPIE, 2007), Vol. 6473, pp. 111–125.

11. C. Rivera, J. Pereiro, Á. Navarro, O. Brandt, and H. Grahn, "Advances in Group-III-Nitride Photodetectors," Open Electr. Electron. Eng. J. **4**, (2010).

12. L. Sang, M. Liao, and M. Sumiya, "A Comprehensive Review of Semiconductor Ultraviolet Photodetectors: From Thin Film to One-Dimensional Nanostructures," Sensors **13**, 10482–10518 (2013).

13. M. A. Khan, J. N. Kuznia, D. T. Olson, J. M. Van Hove, M. Blasingame, and L. F. Reitz, "High-responsivity photoconductive ultraviolet sensors based on insulating single-crystal GaN epilayers," Appl. Phys. Lett. **60**, 2917–2919 (1992).

14. B. W. Lim, Q. C. Chen, J. Y. Yang, and M. Asif Khan, "High responsitivity intrinsic photoconductors based on $Al_xGa_{1-x}N$," Appl. Phys. Lett. **68**, 3761–3762 (1996).

15. B. Shen, K. Yang, L. Zang, Z. Chen, Y. Zhou, P. Chen, R. Zhang, Z. Huang, H. Zhou, and Y. Zheng, "Study of Photocurrent Properties of GaN Ultraviolet Photoconductor Grown on 6H-SiC Substrate," Jpn. J. Appl. Phys. **38**, 767–769 (1999).

16. E. Monroy, F. Calle, J. A. Garrido, P. Youinou, E. Muñoz, F. Omnès, B. Beaumont, and P. Gibart, "Si-doped $Al_xGa_{1-x}N$ photoconductive detectors," Semicond. Sci. Technol. **14**, 685–689 (1999).

17. Q. Chen, J. W. Yang, A. Osinsky, S. Gangopadhyay, B. Lim, M. Z. Anwar, M. Asif Khan, D. Kuksenkov, and H. Temkin, "Schottky barrier detectors on GaN for visible–blind ultraviolet detection," Appl. Phys. Lett. **70**, 2277–2279 (1997).

18. E. Monroy, F. Calle, E. Muñoz, F. Omnès, P. Gibart, and J. A. Muñoz, "$Al_xGa_{1-x}N$:Si Schottky barrier photodiodes with fast response and high detectivity," Appl. Phys. Lett. **73**, 2146–2148 (1998).

19. J. C. Carrano, T. Li, C. J. Eiting, R. D. Dupuis, and J. C. Campbell, "Very high-speed ultraviolet photodetectors fabricated on GaN," J. Electron. Mater. **28**, 325–333 (1999).

20. J. Li, Y. Xu, T. Y. Hsiang, and W. R. Donaldson, "Picosecond response of gallium-nitride metal–semiconductor–metal photodetectors," Appl. Phys. Lett. **84**, 2091–2093 (2004).

21. E. Ozbay, N. Biyikli, I. Kimukin, T. Kartaloglu, T. Tut, and O. Aytur, "High-performance solar-blind photodetectors based on $Al_xGa_{1-x}N$ heterostructures," IEEE J. Sel. Top. Quantum Electron. **10**, 742–751 (2004).

22. G. Y. Xu, A. Salvador, W. Kim, Z. Fan, C. Lu, H. Tang, H. Morkoç, G. Smith, M. Estes, B. Goldenberg, W. Yang, and S. Krishnankutty, "High speed, low noise ultraviolet photodetectors based on GaN p-i-n and AlGaN(p)-GaN(i)-GaN(n)structures," Appl. Phys. Lett. **71**, 2154–2156 (1997).

23. G. Parish, S. Keller, P. Kozodoy, J. P. Ibbetson, H. Marchand, P. T. Fini, S. B. Fleischer, S. P. DenBaars, U. K. Mishra, and E. J. Tarsa, "High-performance (Al,Ga)N-based solar-blind ultraviolet p–i–n detectors on laterally epitaxially overgrown GaN," Appl. Phys. Lett. **75**, 247–249 (1999).

24. M. Mikulics, M. Marso, P. Javorka, P. Kordoš, H. Lüth, M. Kočan, A. Rizzi, S. Wu, and R. Sobolewski, "Ultrafast metal-semiconductor-metal photodetectors on low-temperature-grown GaN," Appl. Phys. Lett. **86**, 211110 (2005).

25. M. Mikulics, P. Kordos, D. Gregusova, R. Adam, M. Kocan, S. Wu, J. Zhang, R. Sobolewski, D. Grutzmacher, and M. Marso, "Monolithic Integration of Ultrafast Photodetector and MESFET in the GaN Material System," IEEE Photonics Technol. Lett. **23**, 1189–1191 (2011).

26. F. Binet, J. Y. Duboz, E. Rosencher, F. Scholz, and V. Härle, "Mechanisms of recombination in GaN photodetectors," Appl. Phys. Lett. **69**, 1202–1204 (1996).

27. C. H. Qiu and J. I. Pankove, "Deep levels and persistent photoconductivity in GaN thin films," Appl. Phys. Lett. **70**, 1983–1985 (1997).

28. N. Biyikli, I. Kimukin, T. Tut, T. Kartaloglu, O. Aytur, and E. Ozbay, "High-speed characterization of solar-blind $Al_xGa_{1-x}N$ p-i-n photodiodes," Semicond. Sci. Technol. **19**, 1259–1262 (2004).

29. J. Ohsawa, T. Kozawa, H. Hayashi, O. Fujishima, and H. Itoh, "Low-Dark-Current Large-Area Narrow-Band Photodetector Using InGaN/GaN Layers on Sapphire," Jpn. J. Appl. Phys. **44**, L623--L625 (2005).

30. D. J. Chen, Y. Huang, B. Liu, Z. L. Xie, R. Zhang, Y. D. Zheng, Y. Wei, and V. Narayanamurti, "High-quality Schottky contacts to n-InGaN alloys prepared for photovoltaic devices," J. Appl. Phys. **105**, 63714 (2009).

31. S. X. Li, K. M. Yu, J. Wu, R. E. Jones, W. Walukiewicz, J. W. Ager, W. Shan, E. E. Haller, H. Lu, and W. J. Schaff, "Fermi-level stabilization energy in group III nitrides," Phys. Rev. B **71**, 161201 (2005).

32. L. Sang, M. Liao, Y. Koide, and M. Sumiya, "High-performance metal-semiconductor-metal InGaN photodetectors using CaF_2 as the insulator," Appl. Phys. Lett. **98**, 103502 (2011).

33. Z. Jian-Jun, W. Bo, J. Ruo-Lian, L. Cheng-Xiang, J. Xiao-Li, X. Zi-Li, C. Dun-Jun, H. Ping, Z. Rong, and Z. You-Dou, "Photoresponse of the $In_{0.3}Ga_{0.7}N$ metal-insulator-semiconductor photodetectors," Chinese Phys. **16**, 2120–2122 (2007).

34. K. Zhang, A. Ma, J. Jiang, Y. Xu, F. Tai, J. Gong, H. Zou, and W. Zhu, "InGaN metal-insulator-semiconductor photodetector using Al_2O_3 as the insulator," Sci. China Technol. Sci. **56**, 633–636 (2013).

35. K. W. Lin, "InGaN p–i–n ultraviolet-A band-pass photodetectors," IEE Proc. - Optoelectron. **153**, 212-214(2) (2006).

36. Y. K. Su, H. C. Lee, J. C. Lin, K. C. Huang, W. J. Lin, T. C. Li, and K. J. Chang, "$In_{0.11}Ga_{0.89}N$-based p-i-n photodetector," Phys. status solidi c **6**, S811–S813 (2009).

37. Y. Lu, Y. Zhang, and X. Li, "Properties of InGaN P-I-N ultraviolet detector," in *7th International Symposium on Advanced Optical Manufacturing and Testing Technologies: Optoelectronics Materials and Devices for Sensing and Imaging*, Y. Jiang, J. Yu, and B. Kippelen, eds. (SPIE, 2014), Vol. 9284, pp. 153–159.

38. R. Singh, D. Doppalapudi, T. D. Moustakas, and L. T. Romano, "Phase separation in InGaN thick films and formation of InGaN/GaN double heterostructures in the entire

alloy composition," Appl. Phys. Lett. **70**, 1089–1091 (1997).

39. D. Doppalapudi, S. N. Basu, K. F. Ludwig, and T. D. Moustakas, "Phase separation and ordering in InGaN alloys grown by molecular beam epitaxy," J. Appl. Phys. **84**, 1389–1395 (1998).

40. Y.-Z. Chiou, Y.-K. Su, S.-J. Chang, Y.-C. Lin, C.-S. Chang, and C.-H. Chen, "InGaN/GaN MQW p–n junction photodetectors," Solid. State. Electron. **46**, 2227–2229 (2002).

41. C. Rivera, J. L. Pau, J. Pereiro, and E. Muñoz, "Properties of Schottky barrier photodiodes based on InGaN/GaN MQW structures," Superlattices Microstruct. **36**, 849–857 (2004).

42. C. Rivera, J. L. Pau, A. Navarro, and E. Munoz, "Photoresponse of (In,Ga)N-GaN multiple-quantum-well structures in the visible and UVA ranges," IEEE J. Quantum Electron. **42**, 51–58 (2006).

43. J. Pereiro, C. Rivera, A. Navarro, E. Munoz, R. Czernecki, S. Grzanka, and M. Leszczynski, "Optimization of InGaN–GaN MQW Photodetector Structures for High-Responsivity Performance," IEEE J. Quantum Electron. **45**, 617–622 (2009).

44. B. Alshehri, K. Dogheche, S. Belahsene, A. Ramdane, G. Patriarche, D. Decoster, and E. Dogheche, "Dynamic Characterization of III-Nitride-Based High-Speed Photodiodes," IEEE Photonics J. **9**, 1–7 (2017).

45. W. Cai, X. Gao, W. Yuan, Y. Yang, J. Yuan, H. Zhu, and Y. Wang, "Integrated p-n junction InGaN/GaN multiple-quantum-well devices with diverse functionalities," Appl. Phys. Express **9**, 52204 (2016).

46. C. Shen, C. Lee, E. Stegenburgs, J. H. Lerma, T. K. Ng, S. Nakamura, S. P. DenBaars, A. Y. Alyamani, M. M. El-Desouki, and B. S. Ooi, "Semipolar III-nitride quantum well waveguide photodetector integrated with laser diode for on-chip photonic system," Appl. Phys. Express **10**, 42201 (2017).

47. C. H. Kang, G. Liu, C. Lee, O. Alkhazragi, J. M. Wagstaff, K.-H. Li, F. Alhawaj, T. K. Ng, J. S. Speck, S. Nakamura, S. P. DenBaars, and B. S. Ooi, "Semipolar $(20\bar{2}\bar{1})$ InGaN/GaN micro-photodetector for gigabit-per-second visible light communication," Appl. Phys. Express **13**, 14001 (2019).

48. X. Liu, R. Lin, H. Chen, S. Zhang, Z. Qian, G. Zhou, X. Chen, X. Zhou, L. Zheng, R. Liu, and P. Tian, "High-Bandwidth InGaN Self-Powered Detector Arrays toward MIMO Visible Light Communication Based on Micro-LED Arrays," ACS Photonics **6**, 3186–3195 (2019).

49. O. Alkhazragi, C. H. Kang, M. Kong, G. Liu, C. Lee, K. Li, H. Zhang, J. M. Wagstaff, F. Alhawaj, T. K. Ng, J. S. Speck, S. Nakamura, S. P. DenBaars, and B. S. Ooi, "7.4-Gbit/s Visible-Light Communication Utilizing Wavelength-Selective Semipolar Micro-Photodetector," IEEE Photonics Technol. Lett. **32**, 767–770 (2020).

50. K.-T. Ho, R. Chen, G. Liu, C. Shen, J. Holguin-Lerma, A. A. Al-Saggaf, T. K. Ng,

M.-S. Alouini, J.-H. He, and B. S. Ooi, "3.2 Gigabit-per-second Visible Light Communication Link with InGaN/GaN MQW Micro-photodetector," Opt. Express **26**, 3037–3045 (2018).

51. C. Lee, C. Zhang, D. L. Becerra, S. Lee, C. A. Forman, S. H. Oh, R. M. Farrell, J. S. Speck, S. Nakamura, J. E. Bowers, and S. P. DenBaars, "Dynamic characteristics of 410 nm semipolar $(20\bar{2}\bar{1})$ III-nitride laser diodes with a modulation bandwidth of over 5 GHz," Appl. Phys. Lett. **109**, 101104 (2016).

52. J. F. Muth, J. H. Lee, I. K. Shmagin, R. M. Kolbas, H. C. Casey, B. P. Keller, U. K. Mishra, and S. P. DenBaars, "Absorption coefficient, energy gap, exciton binding energy, and recombination lifetime of GaN obtained from transmission measurements," Appl. Phys. Lett. **71**, 2572–2574 (1997).

53. S. M. Ting, J. C. Ramer, D. I. Florescu, V. N. Merai, B. E. Albert, A. Parekh, D. S. Lee, D. Lu, D. V Christini, L. Liu, and E. A. Armour, "Morphological evolution of InGaN/GaN quantum-well heterostructures grown by metalorganic chemical vapor deposition," J. Appl. Phys. **94**, 1461–1467 (2003).

54. Y.-L. Hu, R. M. Farrell, C. J. Neufeld, M. Iza, S. C. Cruz, N. Pfaff, D. Simeonov, S. Keller, S. Nakamura, S. P. DenBaars, U. K. Mishra, and J. S. Speck, "Effect of quantum well cap layer thickness on the microstructure and performance of InGaN/GaN solar cells," Appl. Phys. Lett. **100**, 161101 (2012).

55. C. J. Neufeld, S. C. Cruz, R. M. Farrell, M. Iza, J. R. Lang, S. Keller, S. Nakamura, S. P. DenBaars, J. S. Speck, and U. K. Mishra, "Effect of doping and polarization on carrier collection in InGaN quantum well solar cells," Appl. Phys. Lett. **98**, 243507 (2011).

56. C. Rivera and E. Muñoz, "Observation of giant photocurrent gain in highly doped (In,Ga)N⁄GaN multiple-quantum-well-based photodiodes," Appl. Phys. Lett. **92**, 233510 (2008).

57. M. S. Wong, D. Hwang, A. I. Alhassan, C. Lee, R. Ley, S. Nakamura, and S. P. DenBaars, "High efficiency of III-nitride micro-light-emitting diodes by sidewall passivation using atomic layer deposition," Opt. Express **26**, 21324–21331 (2018).

58. P. Chaisakul, D. Marris-Morini, G. Isella, D. Chrastina, X. Le Roux, S. Edmond, E. Cassan, J.-R. Coudevylle, and L. Vivien, "Ge/SiGe multiple quantum well photodiode with 30 GHz bandwidth," Appl. Phys. Lett. **98**, 131112 (2011).

59. D. Ji, B. Ercan, and S. Chowdhury, "Experimental Determination of Velocity-Field Characteristic of Holes in GaN," IEEE Electron Device Lett. **41**, 23–25 (2020).

60. E. Bellotti and F. Bertazzi, "Transport Parameters for Electrons and Holes," in *Nitride Semiconductor Devices: Principles and Simulation* (John Wiley & Sons, Ltd, 2007), pp. 69–93.

61. G. Lucovsky, R. F. Schwarz, and R. B. Emmons, "Transit-Time Considerations in p—i—n Diodes," J. Appl. Phys. **35**, 622–628 (1964).

62. A. Beling and J. C. Campbell, "Chapter 3 - Advances in Photodetectors and Optical Receivers," in *Optical Fiber Telecommunications (Sixth Edition)*, I. P. Kaminow, T. Li, and A. E. Willner, eds., Sixth Edit, Optics and Photonics (Academic Press, 2013), pp. 99–154.

63. J. R. Lang, N. G. Young, R. M. Farrell, Y.-R. Wu, and J. S. Speck, "Carrier escape mechanism dependence on barrier thickness and temperature in InGaN quantum well solar cells," Appl. Phys. Lett. **101**, 181105 (2012).

64. C.-K. Li, M. Piccardo, L.-S. Lu, S. Mayboroda, L. Martinelli, J. Peretti, J. S. Speck, C. Weisbuch, M. Filoche, and Y.-R. Wu, "Localization landscape theory of disorder in semiconductors. III. Application to carrier transport and recombination in light emitting diodes," Phys. Rev. B **95**, 144206 (2017).

65. See http://yrwu-wk.ee.ntu.edu.tw/ for more information on the Schrödinger-Poisson drift-diffusion solver developed by Y.-R. Wu *et al.*.

66. A. E. Romanov, T. J. Baker, S. Nakamura, and J. S. Speck, "Strain-induced polarization in wurtzite III-nitride semipolar layers," J. Appl. Phys. **100**, 23522 (2006).

67. V. Fiorentini, F. Bernardini, and O. Ambacher, "Evidence for nonlinear macroscopic polarization in III–V nitride alloy heterostructures," Appl. Phys. Lett. **80**, 1204–1206 (2002).

68. O. Ambacher, J. Majewski, C. Miskys, A. Link, M. Hermann, M. Eickhoff, M. Stutzmann, F. Bernardini, V. Fiorentini, V. Tilak, B. Schaff, and L. F. Eastman, "Pyroelectric properties of Al(In){GaN}/{GaN} hetero- and quantum well structures," J. Phys. Condens. Matter **14**, 3399–3434 (2002).

69. T.-J. Yang, R. Shivaraman, J. S. Speck, and Y.-R. Wu, "The influence of random indium alloy fluctuations in indium gallium nitride quantum wells on the device behavior," J. Appl. Phys. **116**, 113104 (2014).

70. D. A. Browne, B. Mazumder, Y.-R. Wu, and J. S. Speck, "Electron transport in unipolar InGaN/GaN multiple quantum well structures grown by NH3 molecular beam epitaxy," J. Appl. Phys. **117**, 185703 (2015).

71. M. Sabathil, A. Laubsch, and N. Linder, "Self-consistent modeling of resonant PL in InGaN SQW LED-structure," in *Light-Emitting Diodes: Research, Manufacturing, and Applications XI*, K. P. Streubel and H. Jeon, eds. (SPIE, 2007), Vol. 6486, pp. 212–220.

72. Yih-Guei Wey, K. Giboney, J. Bowers, M. Rodwell, P. Silvestre, P. Thiagarajan, and G. Robinson, "110-GHz GaInAs/InP double heterostructure p-i-n photodetectors," J. Light. Technol. **13**, 1490–1499 (1995).

73. J. Bowers and C. Burrus, "Ultrawide-band long-wavelength p-i-n photodetectors," J. Light. Technol. **5**, 1339–1350 (1987).

74. J.-. Shi, H.-. Huang, J.-. Sheu, S.-. Hsieh, Y.-. Wu, Ja-Yu Lu, F.-. Huang, and W.-. Lai, "Nitride-based photodiode at 510-nm wavelength for plastic optical fiber communication," IEEE Photonics Technol. Lett. **18**, 283–285 (2006).

75. Y. G. Wey, D. L. Crawford, K. Giboney, J. E. Bowers, M. J. Rodwell, P. Silvestre, M. J. Hafich, and G. Y. Robinson, "Ultrafast graded double-heterostructure GaInAs/InP photodiode," Appl. Phys. Lett. **58**, 2156–2158 (1991).

76. M. H. Wong, S. Keller, S. D. Nidhi, D. J. Denninghoff, S. Kolluri, D. F. Brown, J. Lu, N. A. Fichtenbaum, E. Ahmadi, U. Singisetti, A. Chini, S. Rajan, S. P. DenBaars, J. S. Speck, and U. K. Mishra, "N-polar GaN epitaxy and high electron mobility transistors," Semicond. Sci. Technol. **28**, 74009 (2013).

3

Internal Electric Field Reduction in *c*-plane InGaN/GaN Single Quantum Well Light-Emitting Diodes

3.1 Introduction

Current state-of-the-art III-nitride optoelectronic devices are grown along the [0001] axis including InGaN/GaN light-emitting diodes (LEDs). As a result, there is a large polarization-induced electric field in the InGaN quantum well (QW) in the LEDs. The effects of these large internal electric fields have been discussed in Chapter 1. To improve the efficiency and droop performance of LEDs, we focus on reducing internal electric fields in the QWs.

Growing LEDs on semipolar or nonpolar planes is one of the ways to have smaller electric fields in the QWs. Owing to their reduced or non-existence polarization fields, semipolar and nonpolar LEDs with low efficiency droop have been demonstrated [1,2]. Earlier studies on nonpolar planes focused on *m*-plane. However, challenges such as poor indium uptake and stacking fault generation have hindered the progress of *m*-plane LEDs [3]. These challenges motivate the movement to semipolar planes with high inclination angles such as $(20\bar{2}\bar{1})$ and $(30\bar{3}\bar{1})$. However, since most semipolar planes are not naturally occurring during

bulk crystal growth [4], semipolar substrates are created by cutting a bulk GaN boule at a certain angle, resulting in a small substrate size and low boule yield [5]. As such, the cost of growing on the semipolar and nonpolar substrates is much higher. Therefore, it would still be preferable to grow LEDs on *c*-plane substrates which have become the industrial standard.

Theoretical and experimental efforts have shown that it is possible to reduce the internal electric fields in the c-plane QWs through the use of doped barriers [6–8]. Screening the polarization field through the use of doping has been first proposed by Fiorentini *et al*. [6]. The concepts have also been explored experimentally. Young *et al*. has reported complete screening of polarization field in a *c*-plane single QW (SQW) as thick as 7.5 nm by placing heavily doped Mg(Si)-doped *p*(*n*)-type GaN barriers next to the SQW [7]. The LEDs, however, suffered from high Shockley-Read-Hall (SRH) recombination as heavily doped layers are known to cause degradation of epitaxial morphology and introduce nonradiative recombination centers (NRCs) in the LEDs. Despite these challenges, through growth optimization, it is possible to reduce the detrimental impact of nonradiative recombination. The approach of using doped barriers to reduce internal electric field holds great promise for high performance *c*-plane LEDs.

The chapter focuses on the growth and characterization of *c*-plane InGaN/GaN light-emitting diodes with an emphasis on the reduction of internal electric fields through doped barriers. In section 3.2, we will first illustrate the role of doped barriers in the QW field reduction. Through simulations, key parameters were studied to understand how they influence the internal electric fields. Next, section 3.3 and section 3.4 will cover the growth optimization of the LEDs. To decouple the growth problems of the doped barriers and the thick QWs, we first focused our effort on thin (3 nm) SQW LEDs in section 3.3. With an improved growth

condition, we continued the growth optimization on SQW LEDs with thicker QWs (7 nm or 9 nm) in section 3.4. Following the growth optimizations, in section 3.5, we will present the study on a series of LEDs of different well widths with and without doped barriers. We will discuss the results of the biased photocurrent spectroscopy and the droop performance of the thick SQW LEDs. Lastly, section 3.6 will cover the results of differential carrier lifetime measurements on a series of LEDs of different QW indium compositions. The impact of the doped barriers on the recombination coefficients of the LEDs will be discussed.

3.2 Understanding reduction of internal electric fields through doped barriers

Let us consider a simple *c*-plane SQW LED structure. It is essentially a GaN *p*-*i*-*n* diode with an InGaN QW embedded in the intrinsic region. The schematic in Figure 3.1(a) shows a typical (0001) oriented device design with a p-side-up geometry.

At equilibrium (applied voltage = 0 V), similar to a *p*-*n* junction, the p and n-type doped layers are depleted near the edges of the junction. The ionized dopant concentrations in the p and n-type layers are N_A^- and N_D^+, respectively. The idealized "depletion-approximation" charge density profile (ρ) of the structure is presented in Figure 3.1(b). The widths of the depleted region in the p-GaN and n-GaN are labeled as w_p and w_n, respectively. On top of that, for *c*-plane devices, polarization charges (σ_{pol}), resulting from both piezoelectric and spontaneous polarization, also exist at the InGaN/GaN interfaces.

The electric field (E) across the junction is determined by the Poisson equation:

$$\nabla \cdot (\epsilon E) = -\rho = -q\left(p - n + N_D^+ - N_A^- \pm \sigma_{pol}\right) \qquad (1)$$

where $\epsilon = \epsilon_r \epsilon_0$ is the static dielectric constant of the semiconductor. The net charge (ρ) is the combination of the ionized dopant (N_A, N_D), carriers (n, p), and the polarization charge (σ_{pol}). To simplify the expression, we assume $\epsilon_{InGaN} = \epsilon_{GaN} = \epsilon$. In one dimension, the Poisson equation is:

$$\frac{dE}{dx} = \frac{q\left(n - p + N_A^- - N_D^+ \pm \sigma_{pol}\right)}{\epsilon}. \qquad (2)$$

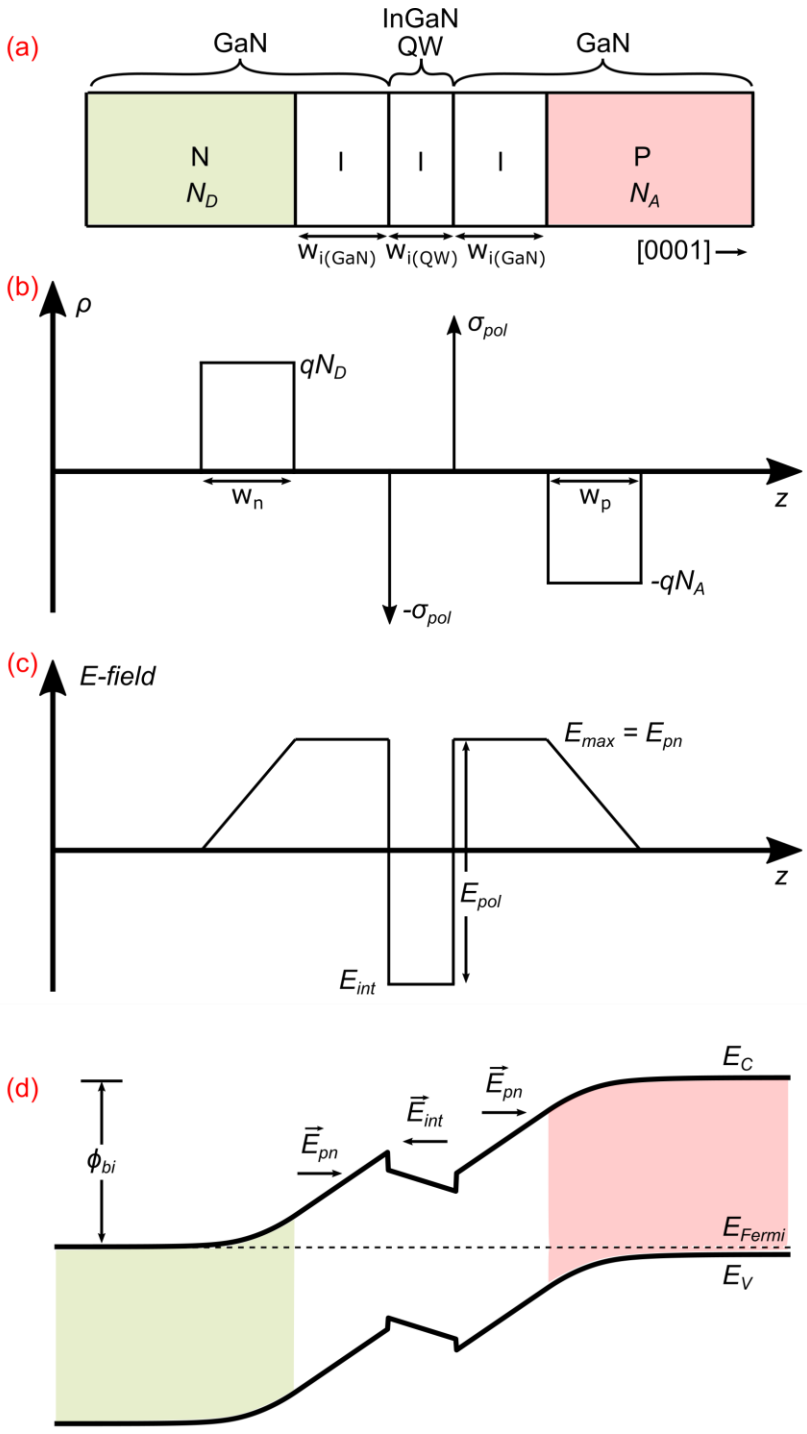

Figure 3.1. (a) A schematic showing a GaN *p-i-n* diode with an InGaN QW, (b) space charge profile, (c) electric field profile, and (d) energy band diagram.

By using Eq. 2, the electric field for the *p-i-n* junction can then be calculated (Figure 3.1(c)). At zero bias, the mobile carrier densities (*n, p*) are assumed to be zero as they are much smaller than the dopant concentration. The electric field increases from the edge of the junction and reaches the maximum value, $E_{max} = \frac{qN_A w_p}{2\epsilon} = \frac{qN_D w_n}{2\epsilon}$. For ease of discussion, the maximum electric field is henceforth referred as the *p-n* junction electric field (E_{pn}) (the electric field in the barrier region is also sometimes called the built-in field). In the intrinsic region, the electric field is constant since charge density is zero everywhere except at the InGaN/GaN interfaces. In reality, it is very difficult to obtain intrinsic GaN and InGaN layers. Undoped GaN and InGaN layers are usually n-type due to the background impurity [9] with concentration around 10^{16} cm^{-3}. This leads to slight changes in the electric field in the "intrinsic" region, but the changes are small enough that they can be ignored here.

The polarization charges at the interface cause a large dip in the electric field. The net internal electric field (E_{int})[1] in the InGaN QW is therefore the difference between E_{pn} and the polarization-induced electric field ($E_{pol} = \sigma_{pol}/\epsilon$):

$$E_{int} = E_{pn} - E_{pol}. \qquad (3)$$

Here, we define the positive sign to be the direction pointing toward the growth surface ([0001] direction). In typical Ga polar *c*-plane LEDs, E_{pol} and E_{pn} are in the opposite direction. Since

[1] In literature, the net internal electric field (E_{int}) is sometimes simply referred to as 'polarization field' since the magnitude of the polarization field (E_{pol}) is much larger than that of *p-n* junction field (E_{pn}) and thus $|E_{int}| \approx |E_{pol}|$. The distinction between the polarization field and the net internal electric field is important in this context as we attempt to reduce the internal electric field in the QW by manipulating the *p-n* junction field. (Note that, the magnitude of the polarization field depends only on the composition and crystal orientation.)

E_{pol} are usually much larger than the E_{pn}, E_{int} is negative. As a result, E_{int} is in the opposite direction of E_{pn} and points toward the substrates ($[000\bar{1}]$ direction) as shown in Figure 3.1(c). Figure 3.1(d) shows the band diagram of the LED at 0 V applied bias. The non-zero internal electric field in the QW leads to a triangular profile in the conduction and valence bands.

An electric field is the gradient of the electrical potential after a change of sign (i.e., $E = -\nabla V$ or $V_{ab} = -\int E\, dz$). In other words, the built-in potential (ϕ_{bi}) is equivalent to the negative area under the graph of electric field against distance. In this simple case, the built-in potential is given by

$$\phi_{bi} = \frac{qN_D w_n^2}{2\epsilon} + \frac{qN_A w_p^2}{2\epsilon} + \left(\frac{qN_D w_n}{2\epsilon} - \frac{\rho_{pol}}{\epsilon}\right) w_{i(QW)} + \frac{2qN_D w_n w_{i(GaN)}}{\epsilon} \qquad (4)$$

where $w_{i(QW)}$ is the width of the InGaN QW and $w_{i(GaN)}$ is the distance between the InGaN QW and the doped layers as shown in Figure 3.1(a).

For the typical case of $E_{pn} < E_{pol}$, in order to reduce E_{int} in the QW, we can either increase E_{pn} or decrease E_{pol}. However, E_{pol} is tied to the indium composition of the InGaN QW which is not a parameter that we can freely control. E_{pn}, on the other hand, depends on the doping concentration of the p and n-type layers and the structure of the *p-i-n* junction.

The magnitude of E_{pn} is determined by $N_A w_p = N_D w_n$ (i.e., the product of the ionized dopant concentration and the depletion width of either side of the *p-i-n* junction). There are many ways to increase $N_A w_p$ and $N_D w_n$: (1) increasing N_A or N_D or (2) decreasing the total thickness of the intrinsic GaN layer between the p and n-type layers (i.e., decreasing $w_{i(GaN)}$).

For the latter approach, we are essentially reducing the region where the built-in potential can be distributed, enlarging w_p and w_n.

Figure 3.2(a) shows the electric field profile of the *p-i-n* junction as dopant concentrations (N_A, N_D) are varied from 1 × 10^{18} cm^{-3} to 2 × 10^{19} cm^{-3}. In the calculation, polarization sheet charge density of 0.014 C m^{-2} was used. The value corresponds to an InGaN QW with 14% indium composition (50% of the theoretical polarization value is used). With increasing dopant concentration, E_{pn} increases, resulting in the reduction of E_{int} as expected. Ultimately, E_{pn} grows larger than E_{pol}, causing the direction of E_{int} to switch. With a high enough dopant concentration (2 × 10^{19} cm^{-3} in this case), E_{int} can be in the same direction as the E_{pn}. It was demonstrated experimentally through biased photocurrent spectroscopy in section 3.5.1. The distance between the QW and p and n-type layers ($w_{i(GaN)}$) is also varied from 0 nm to 40 nm (Figure 3.2(b)). For this series, the dopant concentrations are fixed at 5 × 10^{18} cm^{-3}. With decreasing $w_{i(GaN)}$, a similar trend is observed where the magnitude of E_{int} decreases and ultimately turns positive.

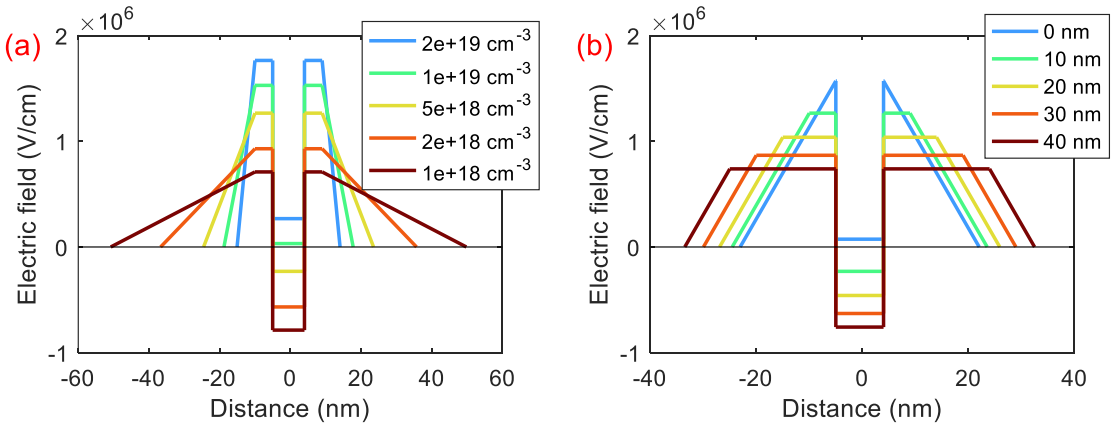

Figure 3.2. Electric field profiles of the SQW LEDs as (a) N_A, N_D are varied from 1 × 10^{18} cm^{-3} to 2 × 10^{19} cm^{-3} and (b) $w_{i(GaN)}$ is varied from 0 nm to 40 nm. The simplistic profiles are obtained by using Eqs. (2)(4).

Our discussion until now has been focused on the devices at zero bias. Under normal LED operating conditions, there is an applied voltage (V_{App}) on the junction. As such, the left-hand side of the Eq. 4 will be replaced by $\phi_{bi} + V_{App}$. On top of that, after the device turn-on, we also have to consider the electrons and holes in the junction. The carrier densities (n, p) are large enough that they cannot be ignored. The excess carriers in the QW lead to a nonmonotonic electric field distribution inside the QW [10]. In the case where $E_{int} < 0$ (i.e., E_{int} and E_{pn} are in opposite direction), the electrons and holes localize at the p and n-side of the QW respectively as shown in Figure 3.3(a). Instead of a constant E_{int}, the magnitude of the field decreases closer to the middle of the QW (Figure 3.3(b)), resulting in the free carrier partial screening of E_{int} [11].

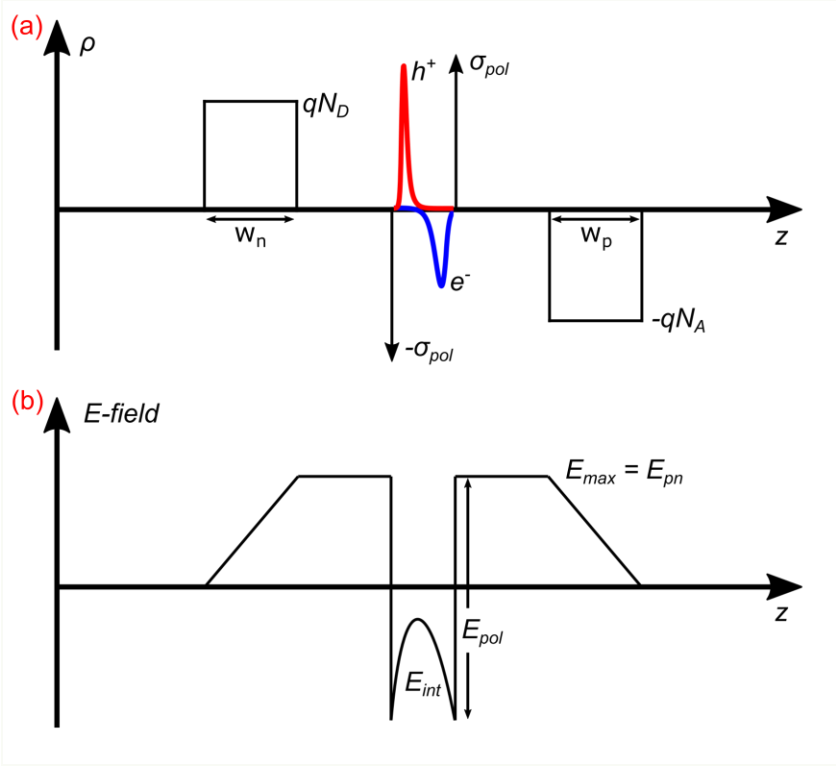

Figure 3.3. (a) Space charge profile and (b) electric field profile of a InGaN/GaN SQW LED under current injection.

To obtain the band diagram and electric field profiles accurately, a one-dimensional Schrödinger-Poisson drift-diffusion solver was used [12]. Only 50% theoretical polarization values were used in the calculation. The simulated structure began with a 30 nm thick n-GaN layer. The 9 nm thick $In_{0.14}Ga_{0.86}N$ single QW is sandwiched by two UID GaN layers with varying thickness ($w_{i(GaN)}$) and 10 nm thick of p(n)-GaN layers with varying doping levels (N_A, N_D) as shown in Figure 3.4. The structure was then capped with a 20 nm p-$Al_{0.10}Ga_{0.90}N$ electron blocking layer (EBL) and a 30 nm thick p-GaN. Simulation parameters are listed in Table 3-1.

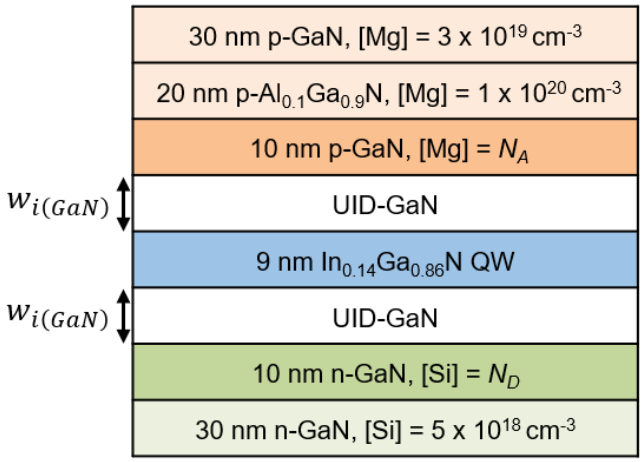

Figure 3.4. Schematic of the epitaxial structure used in the simulations

Layer	E_a (meV)	μ_e (cm^2/Vs)	μ_h (cm^2/Vs)	τ_e^{NR} (s)	τ_h^{NR} (s)	B_o (cm^3/s)	C_o (cm^6/s)
p-GaN	170	32	5	6×10^{-10}	10	3×10^{-11}	2×10^{-31}
p-AlGaN	215	100	5	1×10^{-7}	10	3×10^{-11}	2×10^{-31}
UID-InGaN	*NA*	300	10	1×10^{-7}	1×10^{-7}	3×10^{-11}	2×10^{-31}
UID-GaN	*NA*	300	10	1×10^{-7}	1×10^{-7}	3×10^{-11}	2×10^{-31}
n-GaN	25	200	23	10	7×10^{-10}	3×10^{-11}	2×10^{-31}

Table 3-1. Parameters used in the simulations including: Activation energy (E_a), electron/hole mobility ($\mu_{e/h}$), nonradiative lifetime of electrons/holes ($\tau_{e/h}$), effective radiative recombination coefficient (B_o), and effective Auger recombination coefficient (C_o).

Figure 3.5(a) presents the simulated electric field profiles near the SQW at an injection current density of 10 A/cm^2 as N_A and N_D varied from 5 × 10^{18} cm^{-3} to 9 × 10^{19} cm^{-3}. The distance between the SQW and the doped layers ($w_{i(GaN)}$) was set at 1 nm. As discussed, due to the distribution of electrons and holes in the QW, E_{int} in the QW is not constant and is the smallest near the middle of the well. As shown in Figure 3.5(a), with increasing dopant concentration, E_{pn} increases while the E_{int} decreases. Since E_{int} is not a constant value, we also plotted the average E_{int} in the QW in Figure 3.6(a) as a function of carrier density up to 200 A/cm^2. We see a decrease in the magnitude of the average field at a given current density as the dopant concentrations increase. The simulated band diagrams are also presented in Figure 3.7(a). With increasing dopant concentrations, the flatter QW energy bands lead to less localized electron and hole wavefunctions, resulting in an improvement of the wavefunction overlap.

Similar trends were also observed as $w_{i(GaN)}$ decreased. In these simulations, N_A and N_D were set at 6 × 10^{19} cm^{-3}. The simulated electric field profiles, the average E_{int}, and the simulated band diagrams are presented in Figure 3.5(b), Figure 3.6(b), and Figure 3.7(b),

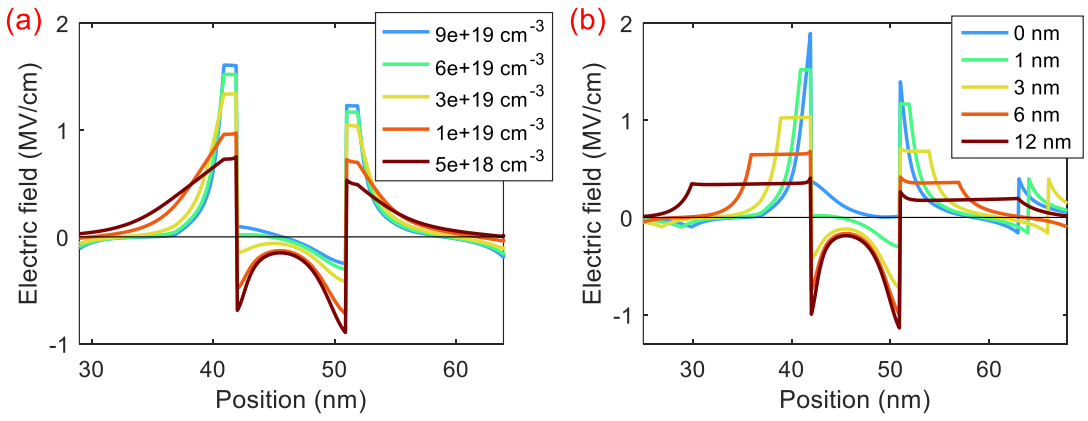

Figure 3.5. Simulated electric field profiles of the SQW LEDs at injection current density of 10 A/cm^2 as (a) N_A, N_D are varied from 5 × 10^{18} cm^{-3} to 9 × 10^{19} cm^{-3}; (b) $w_{i(GaN)}$ is varied from 0.5 nm to 12 nm.

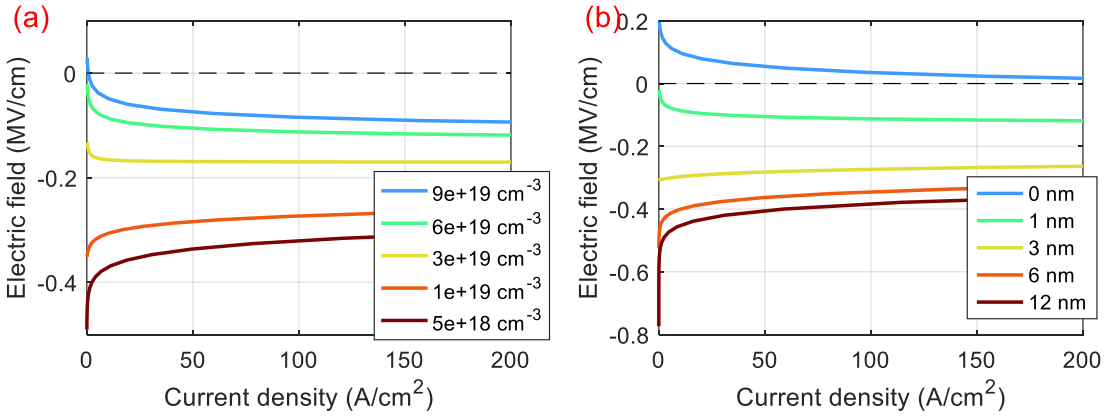

Figure 3.6. The average electric field in the SQW as a function of current density as (a) N_A, N_D are varied from 5 × 10^{18} cm^{-3} to 9 × 10^{19} cm^{-3}; (b) $w_{i(GaN)}$ is varied from 0 nm to 12 nm.

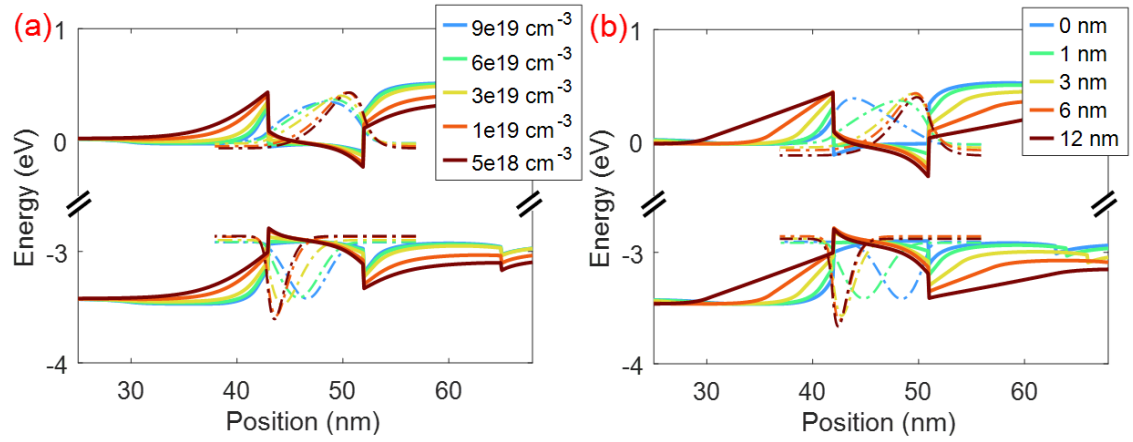

Figure 3.7. Simulated energy band diagrams (solid lines) of the SQW LEDs at injection current density of 10 A/cm^2 as (a) N_A, N_D are varied from 5 × 10^{18} cm^{-3} to 9 × 10^{19} cm^{-3}; (b) $w_{i(GaN)}$ is varied from 0 nm to 12 nm. The dash-dotted lines are the electron and hole wavefunctions

respectively. The magnitude of the average E_{int} in the QW decreases with decreasing $w_{i(GaN)}$ as expected. For the case where $w_{i(GaN)} = 0\ nm$, the sign of average E_{int} was flipped at low current densities (<50 A/cm^2).

In general, through simulations, we have demonstrated that E_{int} in the *c*-plane QW can be reduced by increasing the dopant concentrations of the p- and n-type layers and reducing

the distance between the doped layers and the QW (in other words, reducing the depletion region thickness). In extreme cases, E_{int} can even switch signs and points in the same direction as E_{pn}. This gives us another approach to control E_{int} in the *c*-plane QW.

3.3 Growth optimizations of thin SQW LEDs

The work in this section began with the growth of the multiple quantum well (MQW) InGaN/GaN LEDs which are the industrial standard for high performance LEDs. The samples were grown by metalorganic chemical vapor deposition (MOCVD) on *c*-plane patterned sapphire substrates (PSS). Figure 3.8(a) shows the epitaxial structure which consisted of a 2 µm thick unintentionally doped (UID) GaN template layer, a 2 µm n-GaN layer, a 20-period Si-doped InGaN/GaN superlattice, a 30 nm n-GaN layer, a 5-period undoped InGaN (3 nm)/GaN (24 nm) MQW, a 9 nm p-AlGaN electron blocking layer (EBL), a 130 nm p-GaN layer, and a 10 nm p^+-GaN contact layer. A similar single quantum well (SQW) LED was also grown. The electroluminescence (EL) peak wavelengths of the two LEDs are around 445 nm. Figure 3.8(b) presents the relative external quantum efficiency (EQE) of the two LEDs. Unless otherwise stated, the LEDs were tested using a 'quicktest' method where indium is used as n-contact and p-contacts to the epi material and light is extracted out of the backside of the substrate. The measured EQE is not absolute, but this method provides us with a fast feedback loop to test and compare the samples without processing and packaging the samples. Only a slight drop in efficiency is observed when the active region was changed from MQW to SQW as recombination happens mainly in the QW closest to the p-GaN due to poor hole transport and non-uniform carrier distribution in QWs [13,14].

As discussed in section 3.2, since the thick undoped region of MQW LEDs (which is around 100 nm- 200 nm thick) prevents effective reduction of the internal electric field in the QW, moving forward, only SQW LEDs were studied.

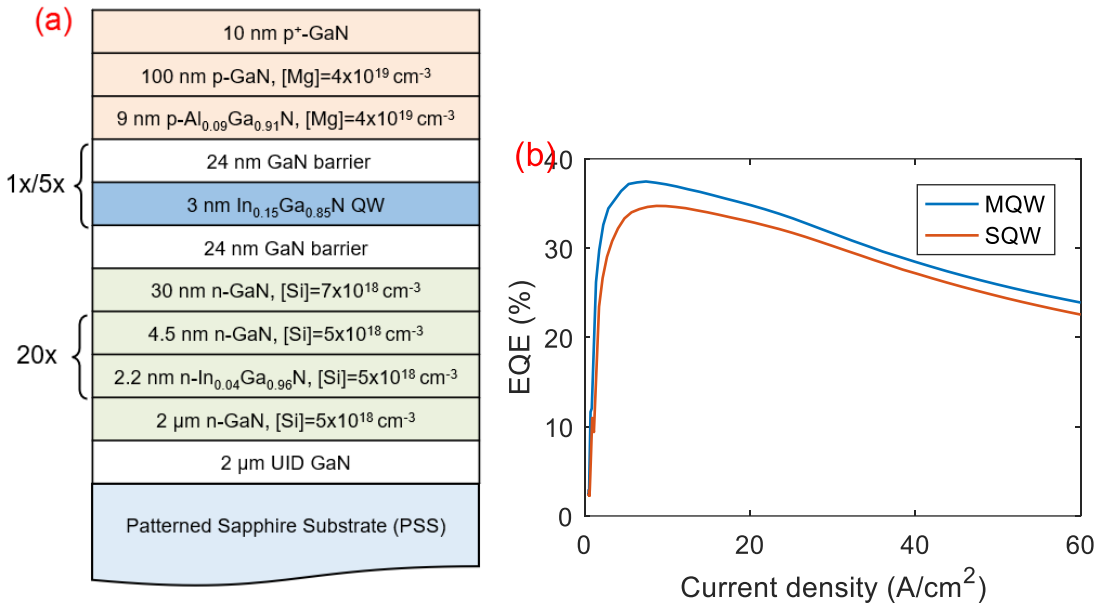

Figure 3.8. (a) Schematic of the epitaxial structures and (b) relative EQE of the MQW and SQW LEDs.

3.3.1 *Impact of doping level and location of doped barriers on thin SQW LEDs*

Our first series focused on the Mg-doped p-type GaN layers. A series of SQW LEDs were grown. The reference LED has two undoped 24 nm thick GaN barriers on both sides of the QW. For the rest of the LEDs in the series, there is a 12 nm thick p-GaN layer after the GaN barrier as shown in Figure 3.9(a). The Mg concentration in the p-GaN layers is calibrated by growing a separate sample which consists of multiple layers of p-GaN with different Cp_2Mg flow rates (Figure 3.10(a)). The targeted Mg concentration for the p-GaN layer is around 1×10^{20} cm^{-3}. However, as we shall see in section 3.3.3, the Mg doping profile in the LED is not abrupt and the actual Mg concentration is actually less than the estimated Mg concentration from the calibration sample. This is due to the delay in Mg incorporation in the first p-GaN layer grown in an epitaxial structure. As such, the actual Mg concentration in the LED is only

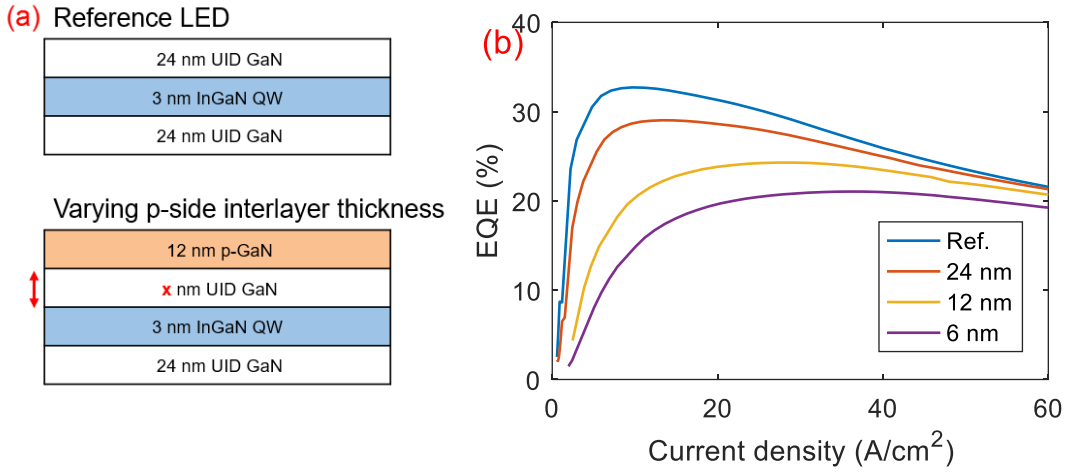

Figure 3.9. (a) Schematic of the epitaxial structures (only show the layers near the QW) and (b) relative EQE as a function of the current density of the LEDs as the thickness of the p-side UID interlayer varies.

around 2×10^{19} cm^{-3} to 8×10^{19} cm^{-3}. For simplicity, we only report the average Mg concentration in the layer.

The thicknesses of the UID GaN interlayers between the p-GaN layer and the SQW were varied from 24 nm to 6 nm. By moving the p-GaN layer closer to the QW, we observed a clear trend of decreasing peak EQE and a shifting of the peak to higher current densities as presented in Figure 3.9(b). The larger decrease in EQE at low current densities indicates an

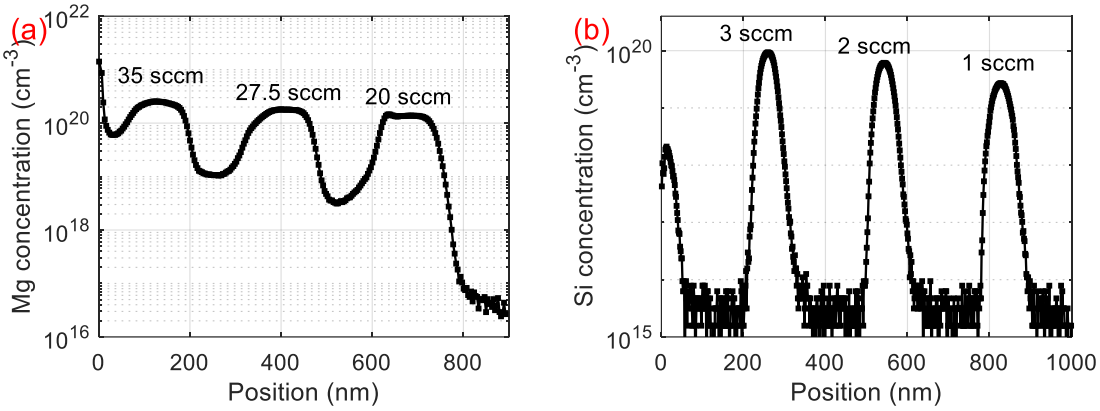

Figure 3.10. SIMS depth profile of (a) magnesium and (b) silicon in the calibration samples. The flow rates of Cp_2Mg and Disilane are also shown in the figures.

increase in Shockley-Read-Hall (SRH) recombination. Another series of SQW LEDs was also grown where the doping level of the p-GaN layer was varied. The thickness of the p-side UID GaN interlayer for this series was fixed at 12 nm. Again, a reduction in EQE was observed with increasing Mg doping level (Figure 3.11(b)).

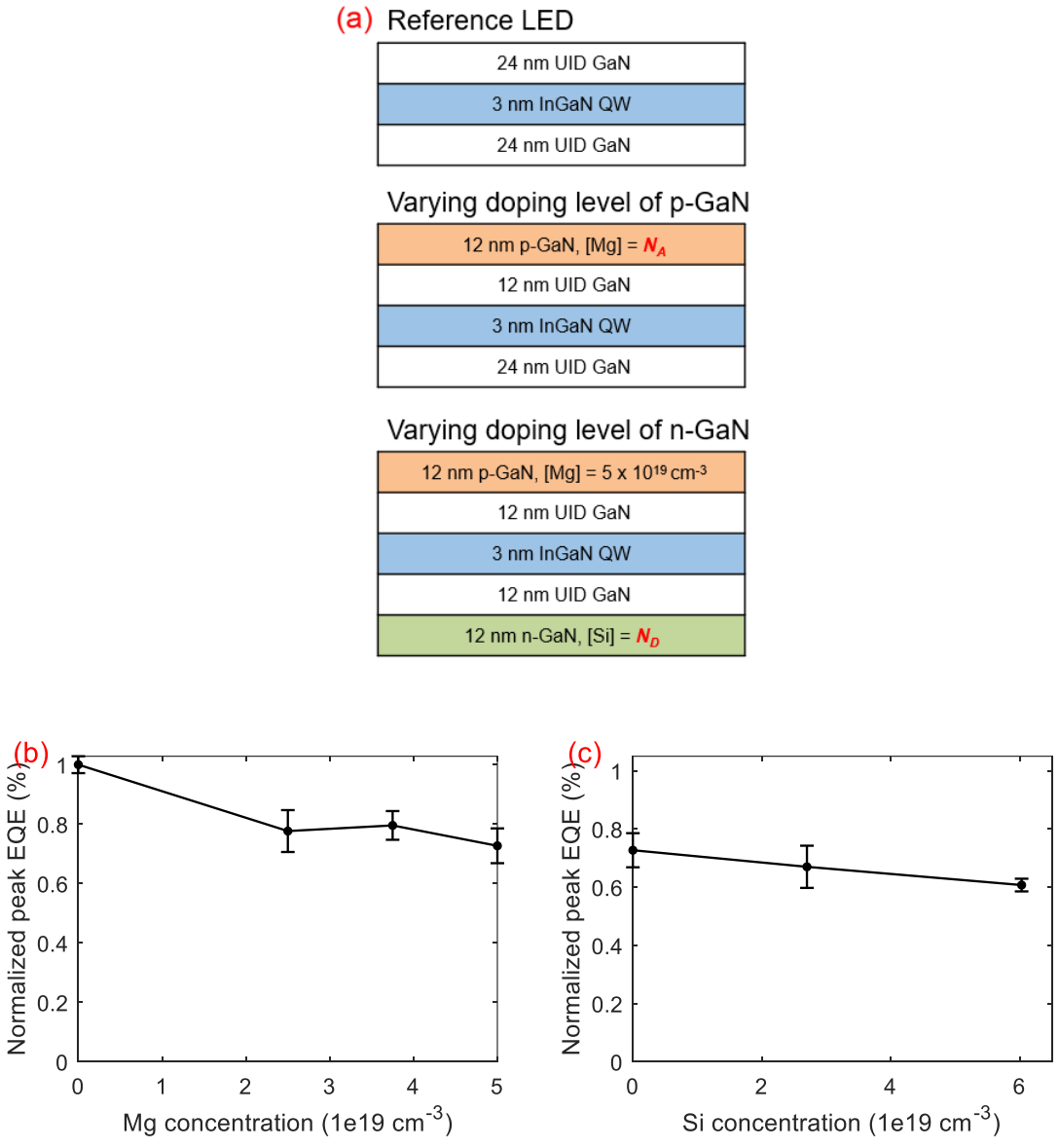

Figure 3.11. (a) Schematic of the epitaxial structures (only show the layers near the QW) and normalized peak EQE (relative to the reference LED) of the LEDs as the doping levels of the (b) p-GaN and (c) n-GaN layers vary.

A series was also grown to study the Si-doped n-type GaN barriers. Both p-GaN and n-GaN layers were grown with 12 nm UID GaN interlayers between the doped barriers and the QW. The Mg concentration in the p-GaN was fixed while the Si concentration was varied from 2.7×10^{19} cm^{-3} to 6.0×10^{19} cm^{-3}. The silicon concentrations were measured by Secondary Ion Mass Spectrometry (SIMS) as shown in Figure 3.10(c). A similar EQE trend was also noticed with increasing Si doping levels.

Despite the potential benefit of improved wavefunction overlap, the doped barriers seem to link to an increase in the SRH coefficients of the LEDs. It was also reported in the past for LEDs with similar structures [7]. The origin of the higher SRH coefficient is not well understood but it could be related to the close proximity of the Mg- and Si-doped layers to the InGaN QW active region. The degradation of the morphology and interfacial quality of the heavily doped layers could be one of the reasons for the increased level of non-radiative recombination centers (NRCs). Further growth optimization is required to minimize the impact of these doped barriers on the device performance.

3.3.2 2-step barrier growth

Up to this point, the 12 nm thick UID GaN interlayer and the p-GaN barrier on top of the QW of the LEDs were grown under the same condition as the QWs. These conditions included growing in the N_2 carrier gas and at the same temperature as the QW. Immediately increasing the growth temperature after the QW growth and introduction of H_2 carrier gas can cause indium desorption and hydrogen etching of the QW which are undesirable. Therefore, a two-step barrier growth process was implemented. This was employed in the past in InGaN/GaN MQW LEDs and solar cells [15,16] where a thin GaN capping layer, often grown

at the same temperature as the QW and in the N_2 carrier gas above the InGaN QW, is used to protect the integrity of the QW. Following the growth of the capping layer, a GaN layer is grown at elevated temperature and in a H_2 carrier gas to improve surface adatom mobility and fill in the V-defects. Restoring the growth morphology following the low temperature QW/capping layer growth is important for the subsequent QW growth in the MQW structures. This process is also beneficial to our SQW LEDs as it improves the material and interfacial quality of the barriers on top of the QW.

The growth conditions of the UID GaN interlayer and the p-GaN barriers were changed except for the bottom 2 nm thick UID GaN layer (denoted as the capping layer) which still shares the same growth conditions as the QW. Two LEDs with different growth conditions (Table 3-2) were grown (3 samples in total, including the reference LEDs). Raising the growth temperature of the interlayer and the p-GaN barriers alone did not improve the LED performance. Changing the type of carrier gas from N_2 to H_2 together with raising the temperature saw a noticeable improvement in the EQE. Moving forward, the 2-step barrier was adopted in all subsequent LEDs.

Sample	Growth temp. (^{o}C)	Carrier gas	Relative EQE (%)
A	875	N_2	25.3
B	915	N_2	24.7
C	915	H_2	29.1

Table 3-2. The growth conditions (of the UID GaN interlayer and the p-GaN barriers) and the relative EQE of the SQW LEDs

3.3.3 *Improving doping profile and incorporation of Mg*

Secondary Ion Mass Spectrometry (SIMS) was used to characterize the doping profile in the LEDs. We noted that the Mg profile of the p-GaN barrier in the LEDs was far from abrupt and the concentration deviated from the value estimated from the calibration sample where thick layers of p-GaN were grown. Figure 3.12(a) shows the measured concentration of Mg, Al, and In in a LED and the cross-sectional schematic of the epitaxial structure. Even though both the p-type EBL and p-GaN barrier were grown under the same Cp_2Mg flow rate of 20 sccm, the Mg concentrations in both layers are different. The Mg concentration in the EBL layer is around 1×10^{20} cm^{-3} and is close to the value estimated through the calibration

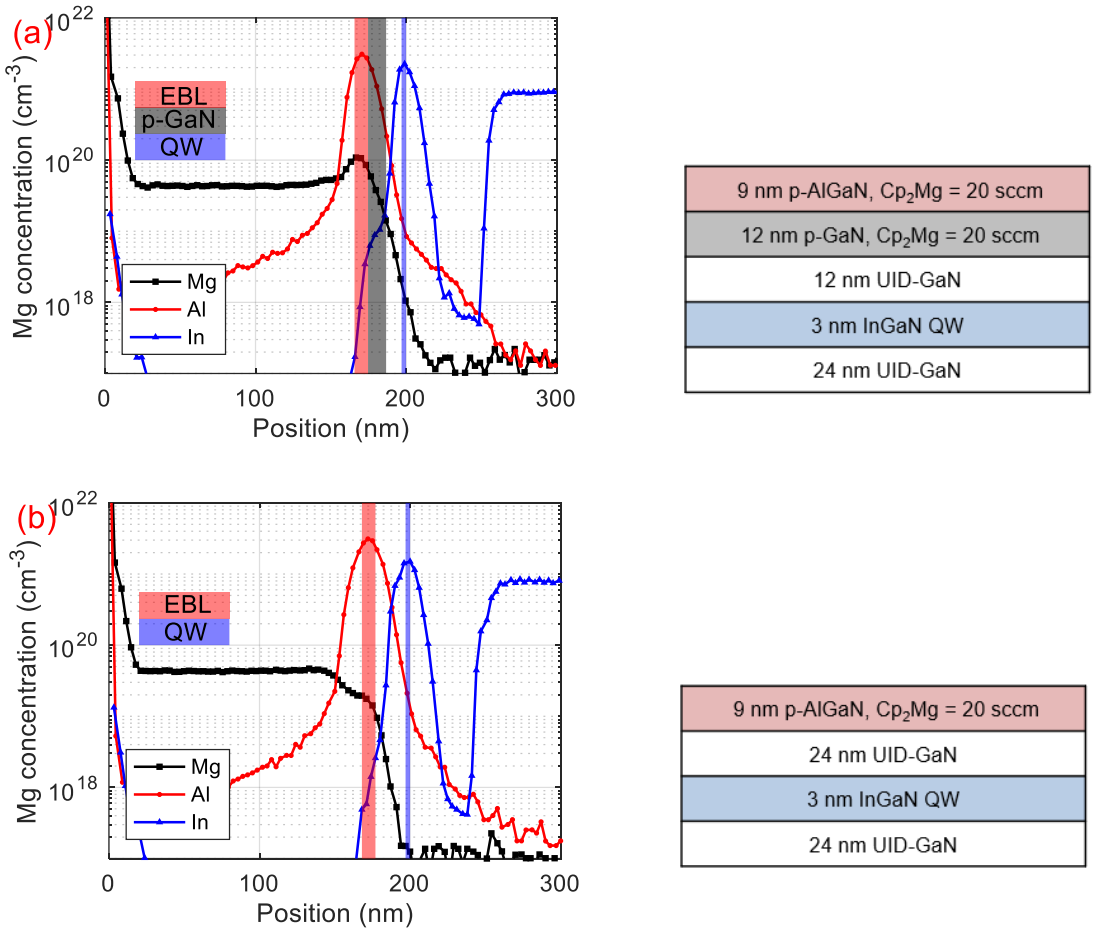

Figure 3.12. SIMS depth profile of Mg-Al-In in (a) LEDs with p-GaN barrier and (b) without p-GaN barrier.

sample (see Figure 3.10(a)). The Mg concentration in the p-GaN barrier, on the other hand, is much lower with values around 2×10^{19} cm^{-3} to 8×10^{19} cm^{-3}. Another sample without the p-GaN barrier was also characterized by SIMS (Figure 3.12(b)). In this sample, the EBL layer, being the first Mg-doped layer in the growth, has a lower Mg concentration of around 2×10^{19} cm^{-3} to 4×10^{19} cm^{-3} even though it has the same Cp_2Mg flow of 20 sccm.

Delay in the incorporation of Mg in III-nitride layers has been reported in the past [17]. The incorporation of Mg is hindered until a sufficiently high concentration of Mg atoms covers the growing surface and the reactor walls. In our study, we clearly see a significant reduction of Mg concentration in the first Mg-doped layers in the growth. Since the doping level of the p-GaN barrier is an important parameter, which directly impacts the internal electric field in the QW, having finer control on the Mg concentration in the p-GaN layer is critical.

A series of LEDs with different Cp_2Mg flow in the p-GaN barriers were grown. The growth conditions are shown in Table 3-3. In one of the samples (LED-D), a Cp_2Mg preflow step was added before the growth of the p-GaN barrier. The growth was paused, and the Cp_2Mg was flowing for 60 s at a flow rate of 15 sccm. Figure 3.13(a) shows the SIMS depth profile of Mg in the LEDs. With increasing flow rate, the Mg concentration in the p-GaN barriers increases. However, the increasing flow rate also increases the Mg concentration of the subsequent EBL layer which has a fixed Cp_2Mg flow rate of 20 sccm. For the sample (LED-

Sample	Cp_2Mg flow rate in the p-GaN barriers (sccm)	Cp_2Mg preflow step
A	15	No
B	30	No
C	45	No
D	15	Yes

Table 3-3. The growth conditions of the SQW LEDs.

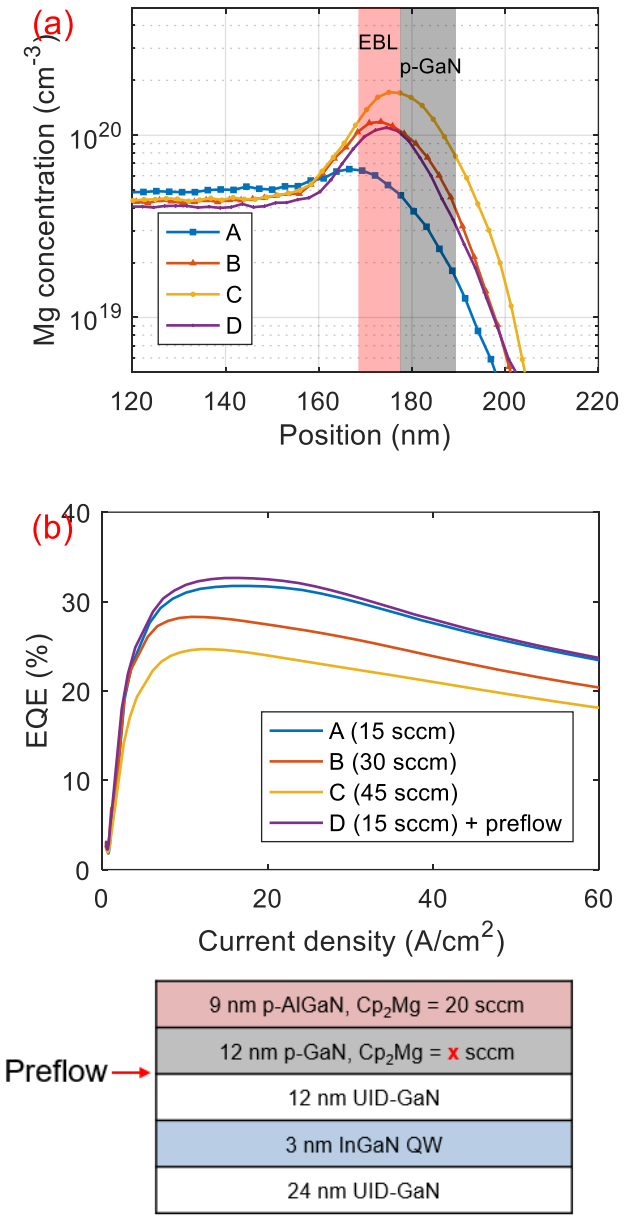

Figure 3.13. (a) SIMS depth profile of Mg in the LEDs. (b) Relative EQE of the LEDs.

D) with the additional preflow step, even though low 15 sccm of Cp_2Mg was used, it has a similar Mg profile as the sample (LED-B) where 30 sccm of Cp_2Mg was used.

Figure 3.13(b) also shows the relative EQE of the four LEDs. Increasing the Cp_2Mg flow rate leads to a reduction of EQE (See LED-A, B, and C). However, there is no noticeable

difference in the EQE between the samples with and without the additional preflow step (LED-A and LED-D). By adding the preflow step, we manage to increase the Mg concentration in the p-GaN barrier without impacting the LED performance.

Reducing the size and density of V-defects

The next growth optimization focused on reducing the density and size of the V-defects. V-defects are inverted hexagonal pyramidal pits that usually form during low temperature MOCVD growth of *c*-plane GaN and InGaN [18–20]. They nucleate at threading dislocations due to the surface depression formed by a dislocation and then propagate outward on $(10\bar{1}1)$ planes. V-defects were generally believed to be deleterious to the device performance in the past. However, in recent years, there have been reports of V-defects being used to improve nitride LEDs, especially for long wavelength devices [21,22]. V-defects were demonstrated to enhance hole injection into deeper wells in MQW LEDs, thereby improving the wall-plug efficiency (WPE) of the LEDs. Nonetheless, in the context of SQW LEDs, the improvement in hole injection is not as impactful since hole injection is not a big problem for SQW active region. On the contrary, V-defects lead to pitted surfaces and rough QW/barrier interfaces. Due to the proximity of the doped barriers to the undoped InGaN SQW and the narrow depletion region, V-defects risk forming leakage pathways and resulting in unwanted dopants in the undoped InGaN active region which could lead to an increase in NRCs.

A SQW LED was grown and interrupted before the InGaN SQW as shown in Figure 3.14 (labeled as sample A). Atomic force microscopy (AFM) was used to characterize the surface of the interrupted growth sample. Figure 3.15(a)(e) present the 20 μm^2 and 5 μm^2 AFM scans of the sample. Numerous V-defects were observed with a density of around 2.2×10^8 cm^{-2} which is close to the threading dislocation density of GaN template grown on sapphire

substrates (mid-10^8 cm^{-2}). The V-defects most likely nucleate during the low temperature growth of the InGaN/GaN superlattice. In order to reduce the density and size of the V-defects, growth conditions of the n-GaN layer on top of the superlattice were modified. The thickness of the n-GaN layer is doubled (30 nm → 60 nm) and the doping level is halved (7.0×10^{18} cm^{-3} → 3.5×10^{18} cm^{-3}) for samples B and C, respectively. Lastly, for sample D, the growth rate of the n-GaN layer and the superlattice were reduced from 1 A/s to 0.5 A/s. Figure 3.15 shows

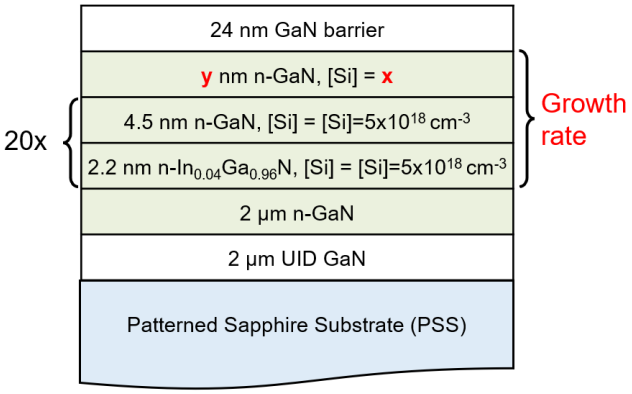

Figure 3.14. Schematic of the epitaxial structure of the interrupted growth samples

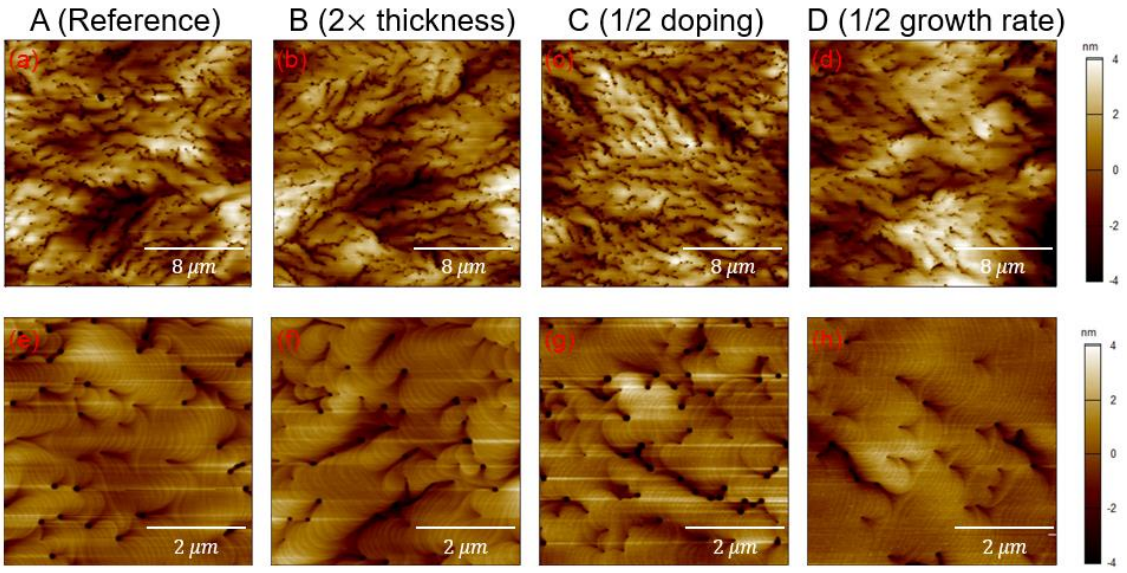

Figure 3.15. (a)(b)(c)(d) 20 × 20 μm^2 AFM images and (d)(e)(f)(g) 5 × 5 μm^2 AFM images of the interrupted samples.

the AFM scans of the samples. No noticeable changes in V-defect density and size for samples B and C, whereas significant improvement was observed for sample D. For sample D, the V-defect density was reduced to around 1.4×10^8 cm^{-2}, and most importantly, there is a noticeable size difference between the V-defects in sample A (>~120 nm) and D (<~80 nm). Reducing the growth rate of the layers preceding the SQW is effective in suppressing the growth of V-defects.

Two SQW LEDs with heavily doped p-GaN and n-GaN barriers on both sides of the QW were grown using the growth conditions used in samples A and D. Significant improvement in EQE was observed for LEDs with the slower growth rate (Figure 3.16). This shows that planarizing the QW/barrier interfaces is important for SQW LEDs with doped barriers.

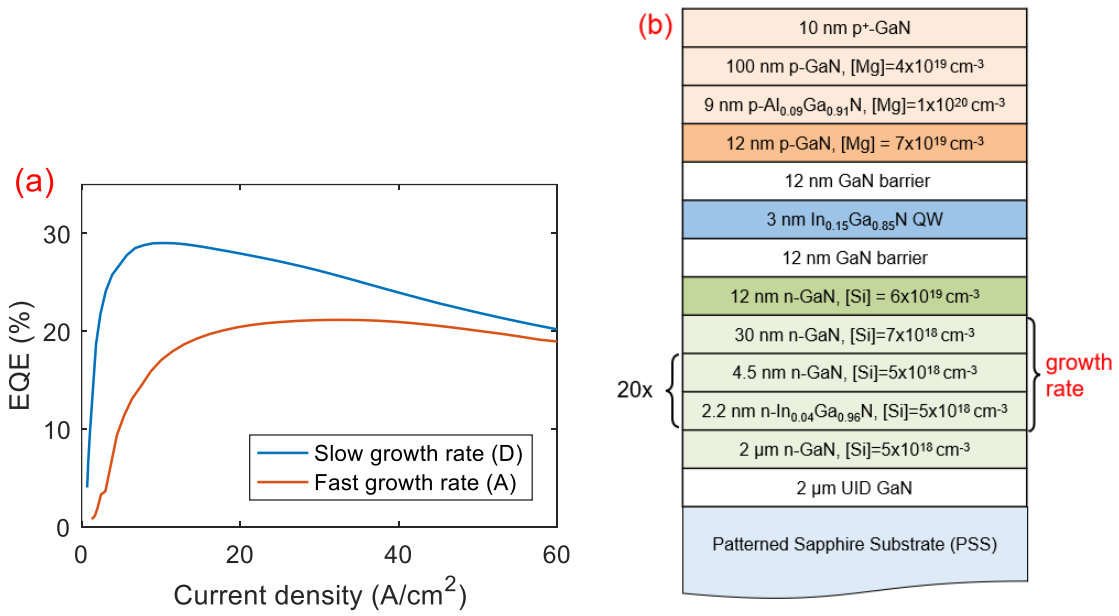

Figure 3.16. Relative EQE of the LEDs with different growth conditions during the growth of superlattice (SL) to reduce V-defect densities and sizes.

3.4 Growth optimizations of thick SQW LEDs

Following the growth optimization of LEDs with thin (3 nm) SQW, we focused on the growth optimization of thick SQW LEDs in this section with the aim of developing LEDs with low efficiency droop. It has been established that Auger recombination, which scales with the cube of the carrier density (n^3), is the primary mechanism responsible for the efficiency droop for nitride LEDs. A straightforward way to delay the onset of the efficiency droop is by increasing the active region volume to lower *n*. However, the large internal electrics in *c*-plane QWs exacerbate the spatial separation of the electron and hole wavefunction, hindering the approach of using a thick InGaN layer active region. By utilizing both thick QW active region (to reduce *n*) and doped barriers (to reduce the internal electric field), we aim to develop *c*-plane thick SQW LEDs with low efficiency droop. In this section, we discuss the growth optimization of thick SQW LEDs.

First, two LEDs with 3 nm and 9 nm thick SQW were grown to study the impact of increasing well widths. 12 nm thick UID GaN interlayers were placed between the heavily Mg(Si)-doped p(n)-GaN layers and the InGaN SQW as shown in Figure 3.17(b). Significant degradation in EQE was observed when the thickness of the QW was increased from 3 nm to 9 nm (Figure 3.17(a)). This is expected as a thicker active region leads to an even larger spatial separation between the electron and hole wavefunction, resulting in a significant loss of wavefunction overlap.

In addition to the lower efficiency, there is also a big spread in device performance for the thick SQW LED across the wafer. Devices measured at different spots of the 2-inch wafer show different EQE as presented in Figure 3.17(a). This is due to the nonuniformity issue in

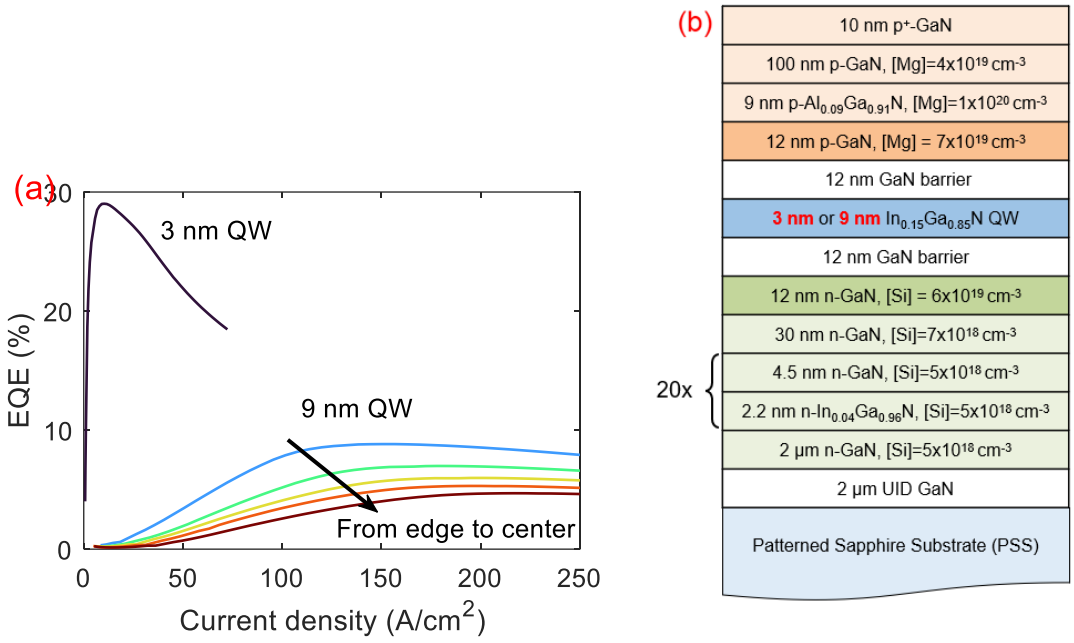

Figure 3.17. (a) Relative EQE and (b) the schematic of the epitaxial structure of the LED with 3 nm thick SQW and 9 nm thick SQW.

the UCSB research MOCVD reactor. There is a growth rate variation across the 2-inch wafer, resulting in thicker QW at the center of the wafer and thinner QW at the edge of the wafer. In a thick QW, the lack of sufficient spatial confinement in the QW causes a significant reduction in the wavefunction overlap. As such, the efficiency of the LED is very sensitive to the thickness of the QW. Without proper internal electric field management, the efficiency of LEDs should decrease with increasing well thickness due to the decreasing wavefunction overlap. Indeed, the peak EQE of the LEDs decreases as the devices get closer to the center of the 2-inch wafer.

3.4.1 Optimizing the thicknesses of the UID GaN interlayers in thick SQW LEDs

Similar to the growth optimization of the thin SQW LEDs, the thicknesses of the interlayers at both p-side and n-side of the SQW were varied. Four LEDs were grown in this series (labeled as series I). The interlayer thicknesses of the LEDs are shown in Table 3-4. In

this series, the doping levels for the p-GaN and n-GaN doped barriers are 7.0×10^{19} cm^{-3} and 5.1×10^{19} cm^{-3}, respectively.

LED	p-side UID interlayer thickness (nm)	n-side UID interlayer thickness (nm)
A	12	12
B	6	6
C	6	0
D	2	0

Table 3-4. The thicknesses of the UID interlayers in LED A, B, C, and D in series I.

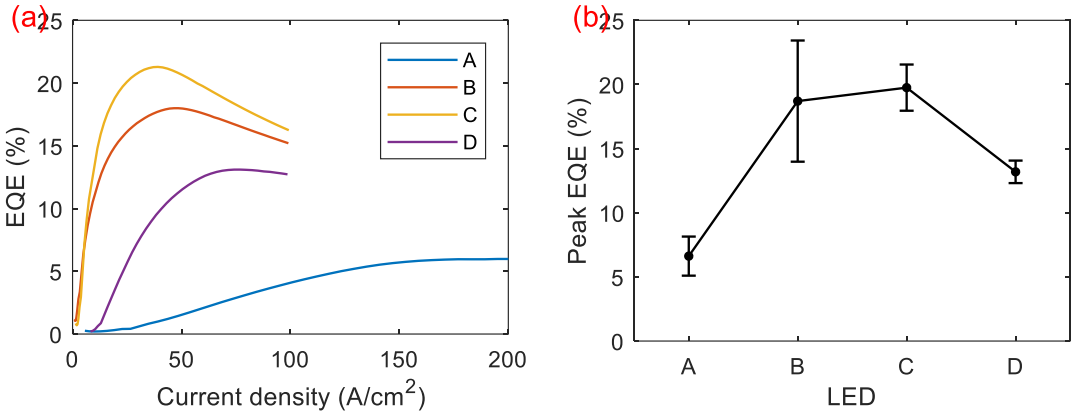

Figure 3.18. (a) Representative EQE as a function of current density and (b) the average peak EQE of thick SQW LED A, B, C, and D.

Figure 3.18(a) shows the EQE of the four LEDs as a function of the carrier density. By reducing the interlayer thickness by half (12 nm to 6 nm), significant improvement in the EQE could be observed (LED A → B). However, the spread of the EQE remains large. The averages and the standard deviations of the peak EQE were shown in Figure 3.18(b). There was a slight improvement in peak EQE when the n-side UID interlayer was completely removed for LED C. Significant improvement in the uniformity of the device performance was also observed. Further reducing the p-side UID interlayer from 6 nm to 2 nm (while having no n-side UID interlayer) saw a decrease in the EQE. In contrast to a similar experiment in thin SQW LEDs (see section 3.3.1), instead of negatively impacting the efficiency, reducing the thickness of

the UID GaN interlayers leads to an improvement in the performance of the LEDs. Nonetheless, when the p-side doped barriers were brought too close to the SQW, similar degradation in EQE was observed.

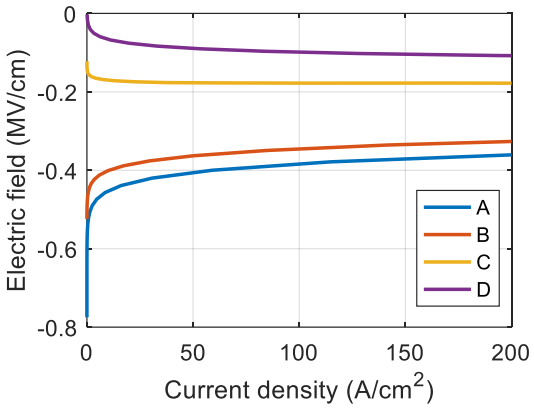

Figure 3.19. The average internal electric field (obtained from simulations) in the SQW as a function of current density of LED A, B, C, and D.

The improvement in the EQE can be explained by the improvement of the wavefunction overlap due to the reduced internal electric field in the SQW. As discussed in section 3.2, reducing the thickness of UID GaN layers in the *p-n* junction restricts the region where the built-in potential can be distributed. This leads to an increase in the *p-n* junction electric field which compensates the opposite polarization field in the SQW, resulting in a smaller net internal electric field in the SQW. A similar Schrödinger-Poisson drift-diffusion solver was used to simulate the electric field profiles of the four LED structures. The average internal electric fields obtained from the simulations are shown in Figure 3.19. As expected, with decreasing interlayer thickness, the magnitude of the internal electric field decreases. Based on this argument, LED-D which has the thinnest UID interlayers should have the best performance. This is not the case because as we have learned in experiments with thin SQW LEDs that doped barriers might also lead to a higher SRH coefficient. The lower EQE in LED-

D is likely due to the increased SRH coefficient as a result of the close proximity of the p-GaN doped barriers to the SQW.

Another two UID interlayer thickness series were grown (series II and III). The doping levels were reduced to [Mg] = 1.5×10^{19} cm^{-3} and [Si] = 1.4×10^{19} cm^{-3} based on the optimization in section 3.4.2 (the next section). The thicknesses of the p-side UID interlayer were varied from 0.5 nm to 8 nm while there is no UID interlayer at the n-side of the QW. Series II and series III have similar epitaxial structures except for the indium composition and the thickness of the QW (listed in Table 3-5). Figure 3.20(a) shows the EQE at 20 A/cm^2 of the four LEDs in series III where improvement in the EQE could be observed as interlayer

LED	QW thickness (nm)	Indium comp. (%)	p-side UID interlayer thickness (nm)
II-A	9	14	8
II-B	9	14	6
II-C	9	14	4
II-D	9	14	2
III-A	7	16	2
III-B	7	16	0.5

Table 3-5. The QW thickness, indium composition, and p-side UID interlayer thickness of the LEDs in series II and series III.

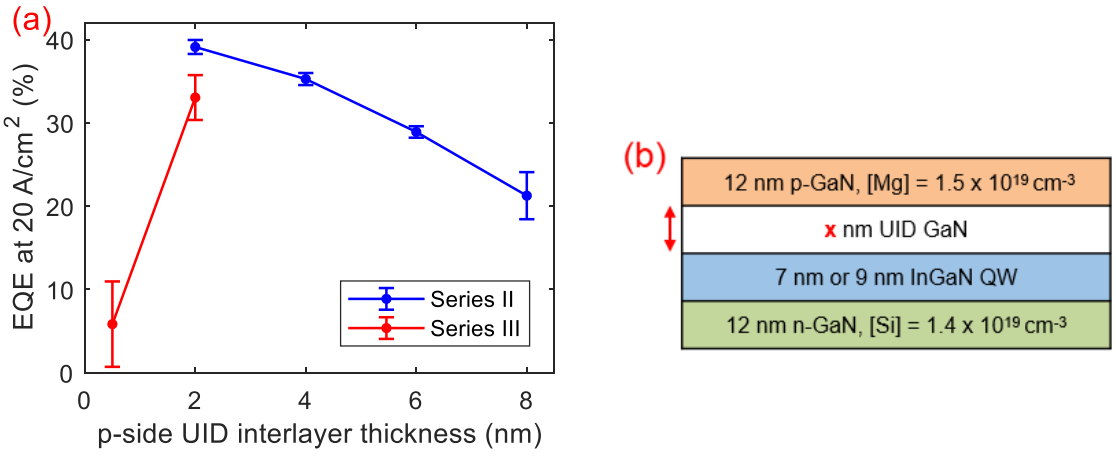

Figure 3.20. (a) Relative EQE at 20 A/cm^2 of LEDs in series II and series III as the p-side UID interlayer thickness varies. (b) Schematic of the epitaxial structure (only shows layers near the SQW).

thickness decreases. With lower doping levels, the trade-off of the higher SRH coefficient is less severe. As a result, the p-GaN doped barriers can be brought much closer to the SQW (down to 2 nm) unlike in series I where doped barriers with much higher dopant concentrations were used. Nonetheless, as the UID interlayer gets too thin (0.5 nm), there is a significant drop in EQE.

In general, we found that the n-side UID interlayer is less important than the p-side UID interlayer, where the completely removal of the n-side UID interlayer is beneficial to the device performance of thick SQW LEDs. On the other hand, the optimized thickness of the p-side UID interlayers was found to be dependent on the doping levels of the p-GaN doped barriers. The optimized thicknesses of the p-side UID interlayers are 6 nm and 2 nm for p-GaN doped barrier with [Mg] = 7.0×10^{19} cm^{-3} and [Mg] = 1.5×10^{19} cm^{-3}, respectively. The lower the doping level, the closer the p-GaN doped barrier can be brought to the QW without seeing a degradation in efficiency.

3.4.2 Optimizing the doping levels of the doped barriers in thick SQW LEDs

Doping levels of the doped barriers were optimized in this section. The study was conducted after series I but before series II and III in section 3.4.1. As a result, the best device in series I (LED-C) was chosen as the starting point. In the epitaxial structure, there is a 6 nm thick p-side UID interlayers between the p-GaN doped barrier and the SQW and none at the n-side. The doping levels of the p-GaN and n-GaN doped barriers were varied from 4.7×10^{19} cm^{-3} to 9.3×10^{19} cm^{-3} and 7×10^{18} cm^{-3} to 7.6×10^{19} cm^{-3}, respectively. We compared the EQE of the LEDs at an injection current density of 20 A/cm^2.

Figure 3.21(a) shows the power of the LEDs as a function of Si concentration for two series. The Mg concentrations of the doped barriers are 4.7×10^{19} cm^{-3} and 7.0×10^{19} cm^{-3} for LEDs in series IV and series V, respectively. In general, with decreasing Si concentration, an improvement in the output power was observed for both series. For series IV, as the Si concentration reaches 7×10^{18} cm^{-3}, there is a significant drop in output power. To investigate further, we looked at the EL wavelengths of two LEDs with the lowest Si concentrations in series I. Figure 3.21(b) shows the peak EL wavelength as a function of current density. The LED with the lowest Si concentration shows a large blueshift with increasing current density which is typical for most *c*-plane InGaN/GaN LEDs. On the other hand, For the LED with the second lowest Si concentration (1.4×10^{19} cm^{-3}), the wavelengths are shorter and show little variation as the current density increases. This is evidence of a reduced internal electric field in the QW [7,23].

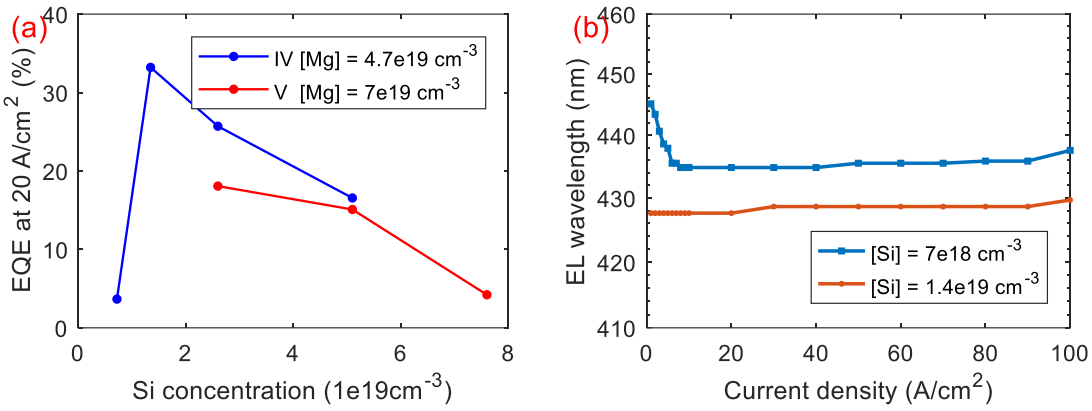

Figure 3.21. (a) Relative EQE at 20 A/cm^2 of the LEDs in series IV and series V as the doping levels of the n-GaN barrier vary. (b) The dependence of the EL wavelength on the current density of two LEDs in series IV with the lowest Si concentration.

The improvement in the output power with decreasing Si concentration can be attributed to the reduction in SRH coefficient, which should decrease with decreasing dopant concentration as we observed in thin SQW LEDs. However, if the Si concentration is too low,

the doped barriers become less effective in reducing the internal electric field, which is especially detrimental to the LEDs with thick QW. For the LED with the lowest Si concentration, the huge degradation in output power and the trend in EL wavelengths show that the reduction of the internal electric field by the doped barriers is insufficient.

Figure 3.22 also shows the output power of the LEDs as a function of Mg concentration in the doped barriers (Figure 3.21(a) and Figure 3.22 share some of the data points). Similarly, with decreasing Mg concentration, there is an improvement in the output power. However, the decline in output power at low Mg concentration was not observed probably due to the range of Mg concentration used in the series.

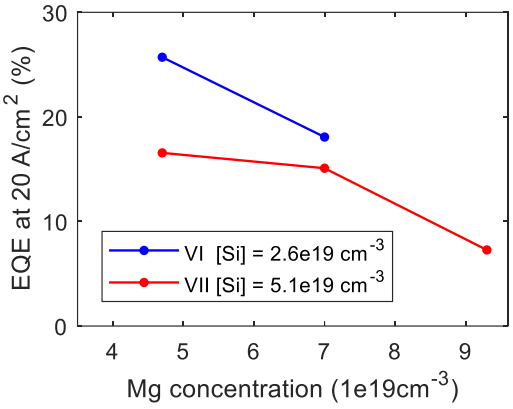

Figure 3.22. Relative EQE at 20 A/cm^2 of the LEDs in series VI and series VII as the doping levels of the p-GaN barrier vary.

3.5 Impacts of doped barriers and quantum well thickness on the LED performance

Following the growth optimizations, we studied how the doped barriers and the quantum well thickness impact the LED performance. In this work, four *c*-plane InGaN/GaN SQW LEDs with different epitaxial structures were grown by metalorganic chemical vapor deposition (MOCVD) on *c*-plane patterned sapphire substrates (PSS). The structures consisted of a 2 μm thick unintentionally doped (UID) GaN template layer, a 2 μm n-GaN layer, a 20-period n-$In_{0.04}Ga_{0.96}N$/GaN 2.2 nm/4.5 nm superlattice, a 30 nm n-GaN layer, a 12 nm UID GaN barrier or Si-doped n-GaN barrier ([Si] = 1.4×10^{19} cm^{-3}), a 3 nm or 9 nm undoped $In_{0.14}Ga_{0.86}N$ QW, a 2 nm UID GaN capping layer, a 10 nm or UID GaN barrier or Mg-doped p-GaN barrier([Mg] = 1.5×10^{19} cm^{-3}), a 26 nm p-$Al_{0.10}Ga_{0.90}N$ electron blocking layer (EBL),

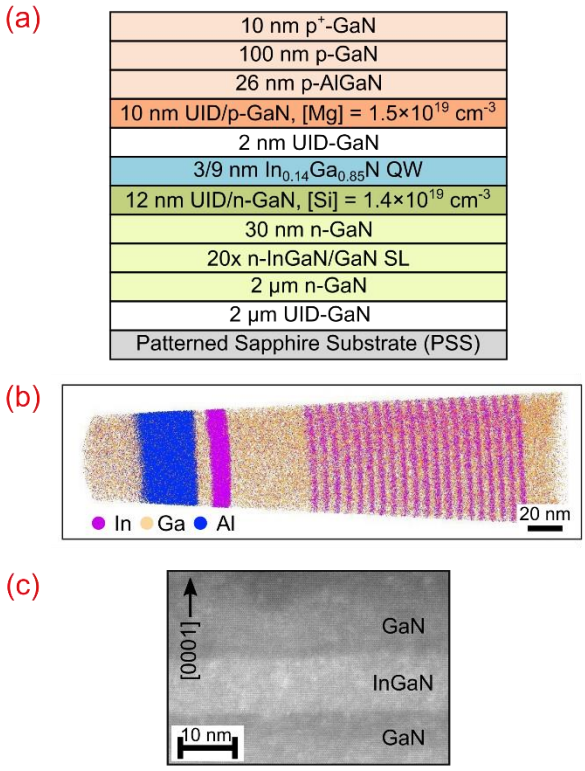

Figure 3.23. (a) Schematic of the epitaxial structures. (b) Atom probe reconstruction and (c) HAADF-STEM image for LED-9D with a 9-nm-thick SQW.

a 100 nm p-GaN, and a 10 nm p^+-GaN contact layer (Figure 3.23 (a)). The 3(9) nm SQW LEDs without and with the doped barriers are henceforth referred to as LED-3UD and LED-3D (LED-9UD and LED-9D), respectively (Table 3-6).

Sample	QW thickness (nm)	Doped barriers
3UD	3	No
3D	3	Yes
9UD	9	No
9D	9	Yes

Table 3-6. The QW thickness and presence or not of doped barriers in the LEDs.

Following the MOCVD growth, the indium composition and QW thickness were measured by x-ray diffraction (XRD) using a PANalytic MRD PRO diffractometer. Furthermore, the indium composition and thickness were also verified by atom probe tomography (APT) and high angle annular dark field scanning transmission electron microscopy (HAADF-STEM) respectively as shown in Figure 3.23(b)-1(c). The samples were then processed into LEDs. First, a 110 nm indium tin oxide (ITO) current spreading layer was deposited by electron-beam evaporation. Rectangular mesas (0.1 mm^2 active area) were then defined by reactive-ion etching the ITO and the epitaxial layers to reach the n-GaN layer. After that, a dielectric omnidirectional reflector (ODR) was deposited via ion beam deposition to serve as a reflective layer and a metal isolation layer. Common Al/Ni/Au n- and p-metal contacts were then deposited by electron-beam evaporation.

3.5.1 Biased photocurrent spectroscopy and simulated electric field profiles

To study the internal electric field (E_{int}) in the QWs, biased photocurrent spectroscopy (BPCS) measurements were carried out on all four LEDs [24,25]. The resulting photocurrent spectra are representative of optical absorption spectra assuming that the collection efficiency

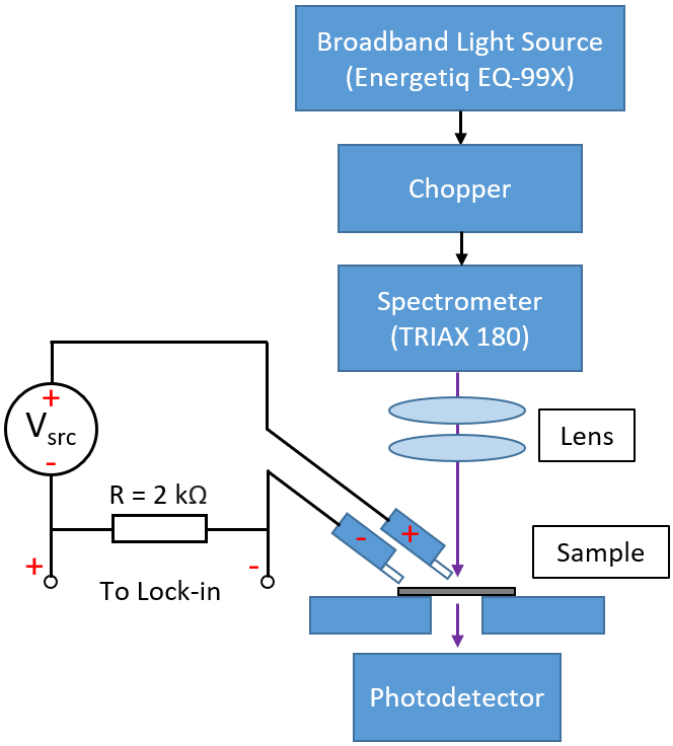

Figure 3.24. The schematic of the biased photocurrent spectroscopy (BPCS) experimental setup.

of the photocurrent is independent of the photon energy [26]. The bias dependence of the photocurrent spectra provides valuable information on the E_{int} as it perturbs the absorption spectra at energies similar to the QW bandgap. In the BPCS setup (Figure 3.24), the LED was illuminated with monochromatic light using a TRIAX 180 monochromator with an Energetiq EQ-99 light source. The LED was biased with a Keithley 2400 sourcemeter. A 2 kΩ resistor was placed in series with the LED to allow the measurement of the photocurrent through it. The additional voltage drop due to the resistor is negligible compared to the applied biases because of the small photocurrent. The optical beam was chopped at 82 Hz and the photocurrent signal was measured with a Princeton Applied Research 5209 lock-in amplifier. The photocurrent spectra were normalized to account for the wavelength dependence of the intensity of the light source. BPCS measurements were performed on the LEDs for applied biases varying from around +1 V to -2 V.

Figure 3.25(a) shows the photocurrent spectra for LED-3UD (3 nm QW, without doped barriers). A blueshift in the absorption edge has been observed as the applied bias changes from +1.2 V to -2 V (where the negative sign indicates a reverse bias). In the conventional Ga-polar InGaN/GaN LEDs with p-side-up geometry, the polarization-related electric field (E_{pol}) in the QW is in the opposite direction of the *p-n* junction electric field (E_{pn}) in the diode. For most InGaN/GaN structures, since the E_{pol} is much larger than the E_{pn}, the net E_{int} in the QW points toward the substrate. For LED-3UD, this remains true as confirmed by the simulations. By using a Schrödinger-Poisson drift-diffusion solver [12,27], the electric fields and band diagrams of the LEDs were simulated with 50% theoretical polarization values. Simulation parameters can be found in section 3.2. As shown in Figure 3.26(a), at zero bias, the E_{int} of LED-3UD is in the opposite direction of the E_{pn}. As a result, increasing the reverse bias leads to a reduction of the net E_{int} and ultimately a blueshift in the absorption edge due to the reduced quantum confined Stark effect (QCSE). This trend is consistent with the BPCS results of *c*-plane InGaN/GaN MQW solar cells [24]. Excitonic features also appeared in the photocurrent spectra at applied biases of -1 V to -2 V. It is known that the E_{int} reduces the exciton binding energy [28,29]. The appearance of exciton peaks in the spectra indicates that the E_{int} is close to zero at -1 V to -2 V biases [30]. From the simulations (Fig. 2(c)), the E_{int} is indeed close to zero at a diode bias of -1 V. The slight discrepancy might be due to the uncertainty in the polarization values used in the simulations. A further increase in the reverse bias should invert the bands, leading to a redshift in the absorption edge. The redshift in the photocurrent spectra after -2 V (not shown) is difficult to observe due to the decreasing signal-to-noise ratio as a result of the increasing leakage current. LED-9UD demonstrated a similar trend (Figure 3.25(c)) except no excitonic features were observed. With a larger well width of 9 nm, the resultant

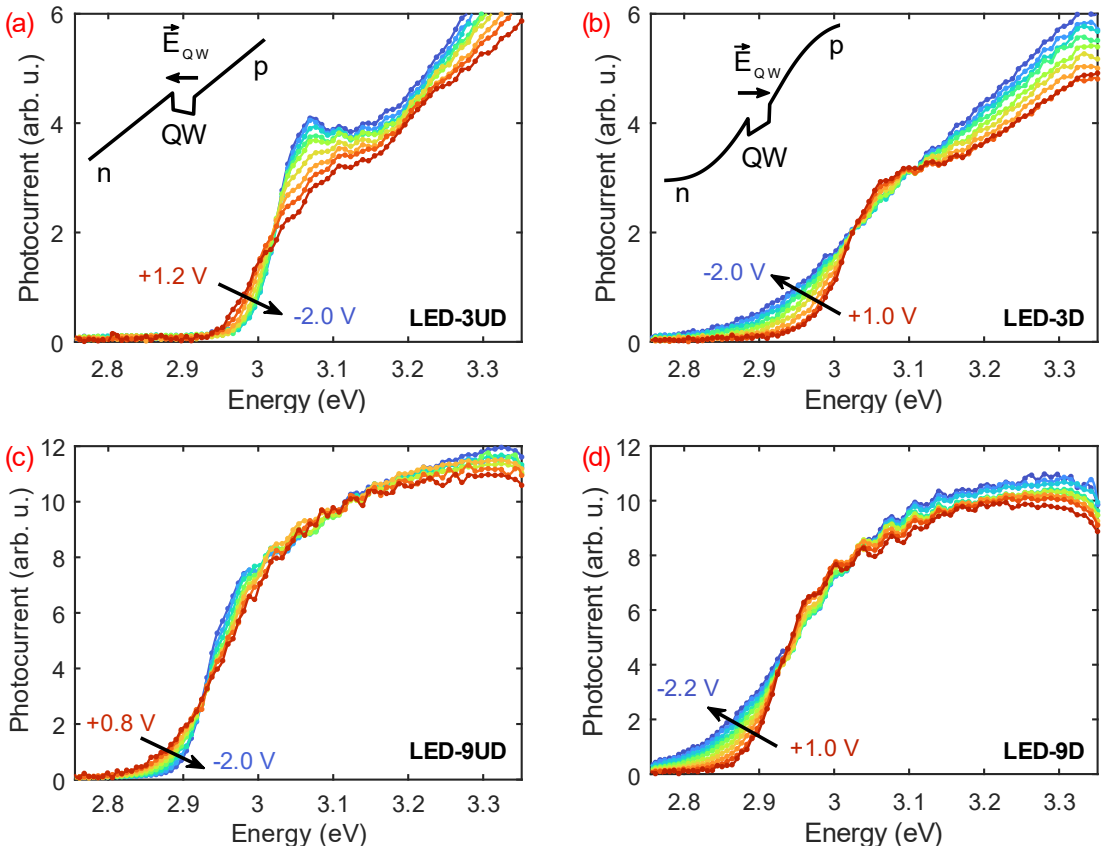

Figure 3.25. Photocurrent spectra for (a) LED-3UD, (b) LED-3D, (c) LED-9UD, (d) LED-9D. The insets in (a) and (b) show the simulated conduction band diagrams at zero bias for LED-3UD and LED-3D, respectively.

lower exciton binding energy makes excitons unstable at room temperature [29]. The BPCS results verified that the E_{int} of both LED-3UD and LED-9UD are in the opposite direction of the E_{pn} at zero bias. Consequently, with increasing forward bias, the E_{int} continues to increase, exacerbating the QCSE, until the partial screening of the E_{pol} by injected free carriers happens at high current densities.

Contrary to the results of LEDs without doped barriers (LED-3UD and LED-9UD), the absorption edges of photocurrent spectra for both LED-3D and LED-9D undergo a redshift as the applied bias varies from around +1 V to -2 V as shown in Figure 3.25(b) and (d). Figure 3.26(b) and (d) show the simulated electric fields of LED-3D and LED-9D under several biased

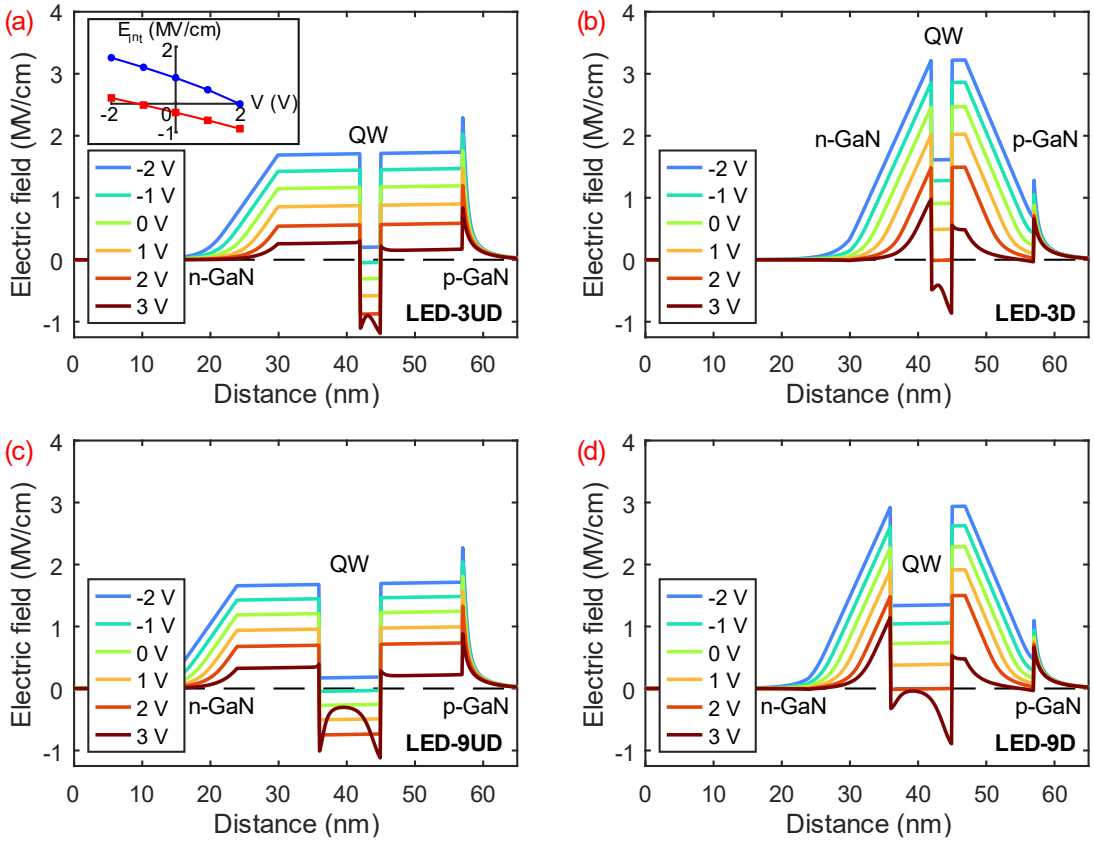

Figure 3.26. Simulated electric fields for (a) LED-3UD, (b) LED-3D, (c) LED-9UD and (d) LED-9D at different bias voltages. Positive electric fields point from the substrate towards the growth surface. The inset in (a) shows the dependence of the internal electric field in the QW (E_{int}) on bias voltages for LED-3UD (red) and LED-3D (blue).

conditions. These electric fields are useful to explain the opposite trends observed in BPCS between LEDs with and without the doped barriers. The thin UID region (5 nm and 11 nm for LED-3D and LED-9D respectively) combined with the highly doped barriers lead to an increase in the E_{pn} across the junction. At zero bias, the maximum E_{pn} is actually higher than the E_{pol} in the QW. Consequently, the net E_{int} in the QW is in the same direction as the *p-n* junction field. As a result, the E_{int} increases with the reverse bias, exacerbating the QCSE and thus causing the redshift in the absorption edge. The observed trends and simulations are in good agreement, verifying that the E_{int} is indeed in the same direction as the E_{pn} at least in the

BPCS applied bias range of -2 V to +1 V (including zero bias). With increasing forward bias, the E_{int} decreases and reaches zero at +2 V according to the simulations. However, this does not imply flat energy bands in the QW when the LEDs are turned on since a further increase in the forward bias results in non-zero E_{int}. Furthermore, after the device turn-on, the excess carriers in the QW also lead to a nonmonotonic electric field distribution inside the QW as shown in Figure 3.26 (+3 V) [10]. Nonetheless, the E_{int} in the LEDs with doped barriers is projected to be lower once the LEDs are in operating condition (>2.9 V) based on the trend of the BPCS results. The lower electric fields lead to flatter energy bands in the QW and an enhancement in the ground state electron-hole wavefunction overlap.

3.5.2 Simulated electron-hole wavefunction overlap

Electron and hole wavefunctions of the four LEDs were also computed with the same Schrödinger-Poisson drift-diffusion solver mentioned above. We first look at the carrier wavefunctions of LED-9UD and LED-9D, as shown in Figure 3.27. Due to E_{int} in the QWs (which point towards the substrates), the electron and hole wavefunctions tend to localize at

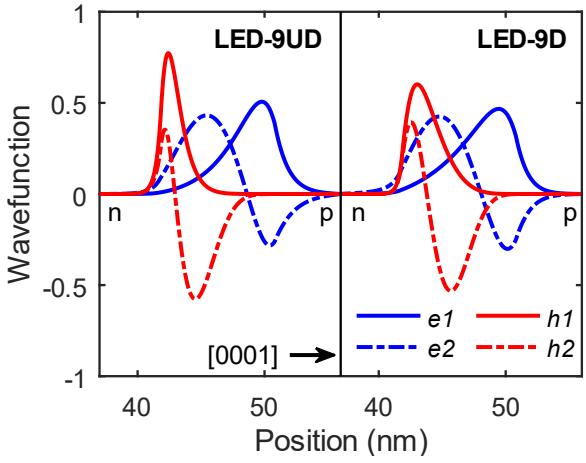

Figure 3.27. Carrier wavefunctions (*e1*, *e2*, *h1*, and *h2*) of (a) LED-9UD and (b) LED-9D at 100 A/cm^2.

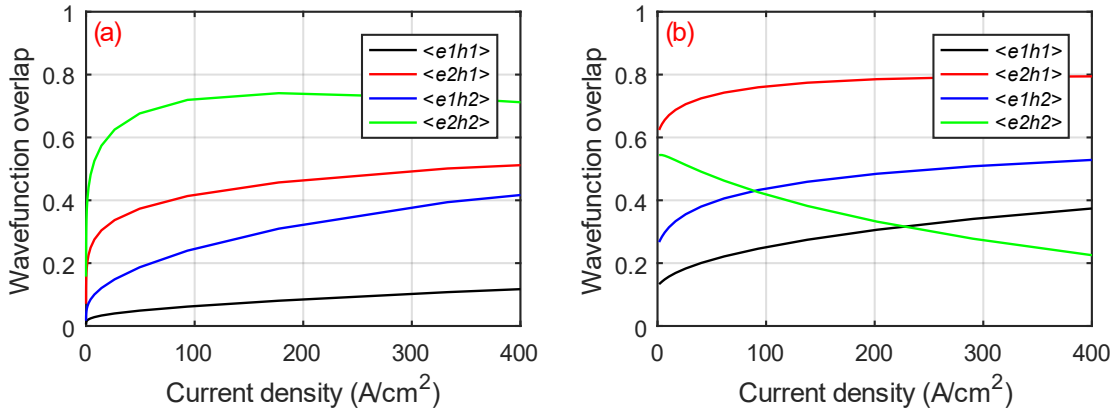

Figure 3.28. Simulated wavefunction overlap of transitions involving the first excited states (*e2*, *h2*) as a function of current density of (a) LED-9UD and (b) LED-9D.

the p and n-side of the QW, respectively. This applies even for the less localized excited states (*e2* and *h2*) although to a lesser extent. With a smaller internal electric field, the wavefunctions in LED-9D, especially the ground states (*e1* and *h1*), are closer to the center of the QW. As a result, there is an improvement in wavefunction overlap for all the transitions involving the ground states compared to that of LED-9UD. The calculated wavefunction overlap of transitions involving the first excited states is plotted for LED-9UD and LED-9D in Figure 3.28. The internal electric field breaks the symmetry of the well, allowing forbidden transitions such as <*e2h1*> and <*e1h2*> transitions. The transitions with the highest overlap are <*e2h2*> and <*e2h1*> for LED-9UD and LED-9D, respectively.

We now compare the ground state <*e1h1*> overlap of the 4 LEDs. Figure 3.29 shows the simulated wavefunction overlap for the four LEDs as a function of the current density. Comparing the <*e1h1*> overlap, it is clear that LEDs with doped barriers exhibit a large overlap compared to their counterparts without doped barriers. However, the overlap of the thick QW LEDs is still small compared to that of thin QW LEDs which have a high degree of confinement. Therefore, for thick QW LEDs, transitions via excited states should also be

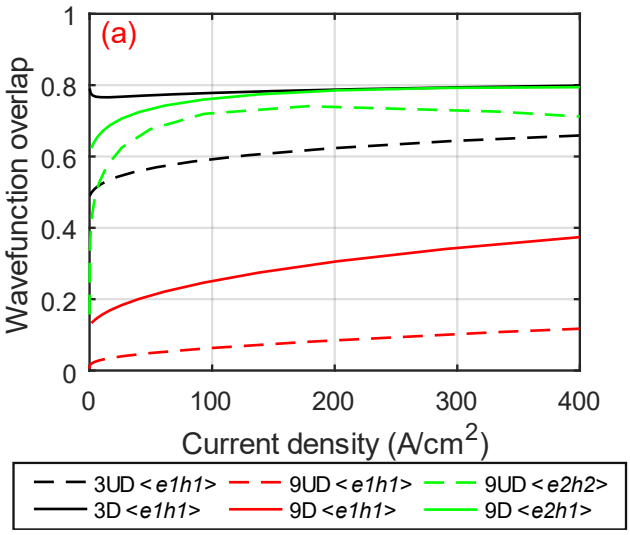

Figure 3.29. Simulated electron-hole wavefunction overlap as a function of current density of the four LEDs.

considered as they can be efficient recombination paths due to the low <*e1h1*> transition rate [31]. The transitions with the highest overlap involving the first excited states for LED-9UD and LED-9D (<*e2h2*> and <*e2h1*> respectively) are also shown in Figure 3.29. As discussed, carriers in the excited states are less localized at the edges of the QW and have a larger spatial extent. Therefore, even with a thick QW, the overlap can be high and comparable to the <*e1h1*> overlap of thin QW LEDs. However, the high wavefunction overlap by itself does not imply that the particular transition contributes significantly to the emission process as the radiative rate of each transition also depends on the population of the participating states.

3.5.3 Simulated energy band diagrams

To further investigate, the simulated energy band diagrams of LED-9UD and LED-9D at 50 A/cm^2 are presented in Figure 3.30(a). For LED-9UD, there are large electric fields near the edges of the QW where the ground states are confined. This leads to a sharp triangular

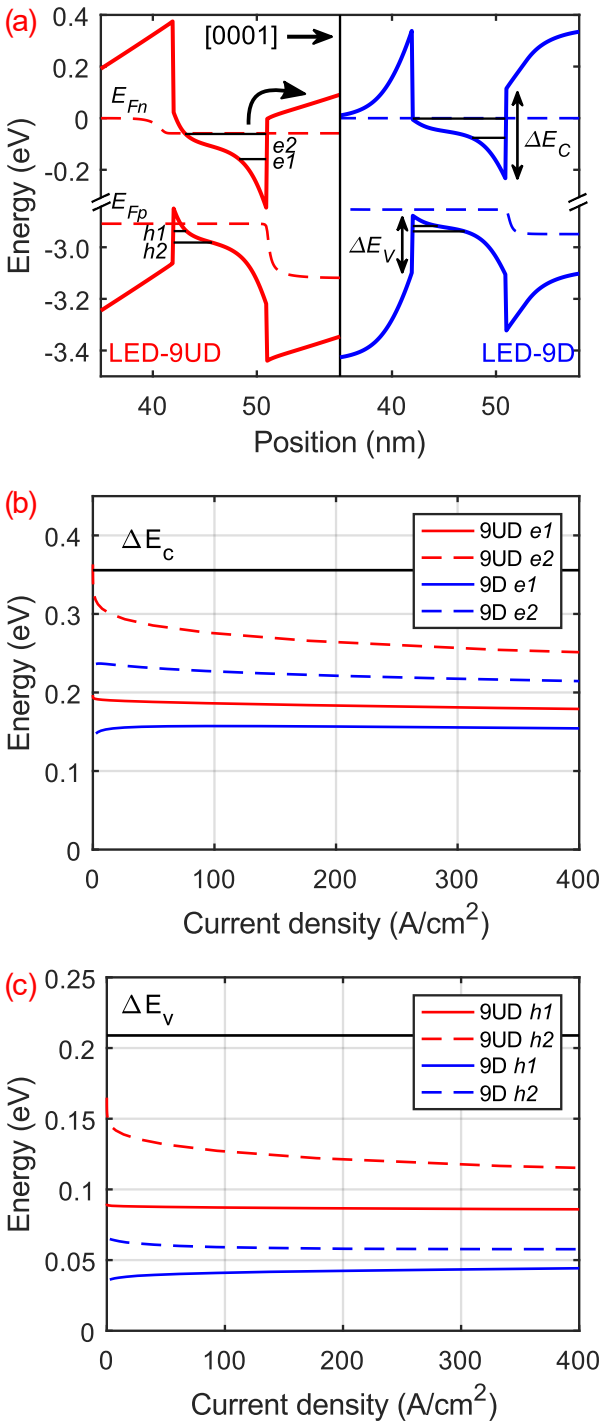

Figure 3.30. (a) Band diagrams near the QWs of LED-9UD (red) and LED-9D (blue) at 50 A/cm^2. The energy levels of the eigenstates and the quasi-Fermi levels ($E_{Fn(p)}$) are also shown in the figures. (b) (c) The energy levels of the eigenstates relative to the bottom of the QW for electrons (b) and holes (c) as a function of current density. The conduction and valence band offsets (ΔE_C and ΔE_V) are also shown in the figures.

profile at the n(p)-side of the valence (conduction) band, thereby causing a large energy separation between the eigenstates for both electrons and holes. On the other hand, for LED-9D that has a smaller E_{int}, the regions at the edges of the QW are flatter, resulting in smaller energy separations. This can be easily understood using the simple case of infinite square wells where the energy separation is inversely proportional to the well width. Here, the sharper triangle profile corresponds to a narrower well with increased confinement energy and separation between confined states. The observed trends still apply at different current densities as shown in Figure 3.30(b)(c) where the computed eigenvalues of each eigenstate as a function of the current density are plotted. For LED-9UD, in order to populate the excited states, the large energy difference between the ground states and excited states leads to a large population of carriers in the ground states. It is manifested in the measured electroluminescence (EL) spectra shown in Figure 3.31(a) which exhibited two peaks at a low current density, representing the ground state and the excited state emissions. The energy difference between the peaks is around 0.2 eV and is in good agreement with the calculated energy difference between <*e1h1*> and <*e2h2*> transitions, as shown in Figure 3.32(a). With increasing current densities, the spectra are dominated by the excited state emission. On the other hand, given the small energy separation between the eigenstates for LED-9D, it is easier to populate the excited states without significant built-up of carriers in the ground states. Consequently, the EL spectra of LED-9D (Figure 3.31(b)) shows a single peak with a transition energy close to the more efficient <*e2h1*> or <*e2h2*> transition (Figure 3.32(b)). Therefore, it is clear that for both thick QW LEDs, transitions via excited states play a significant role in the emission process.

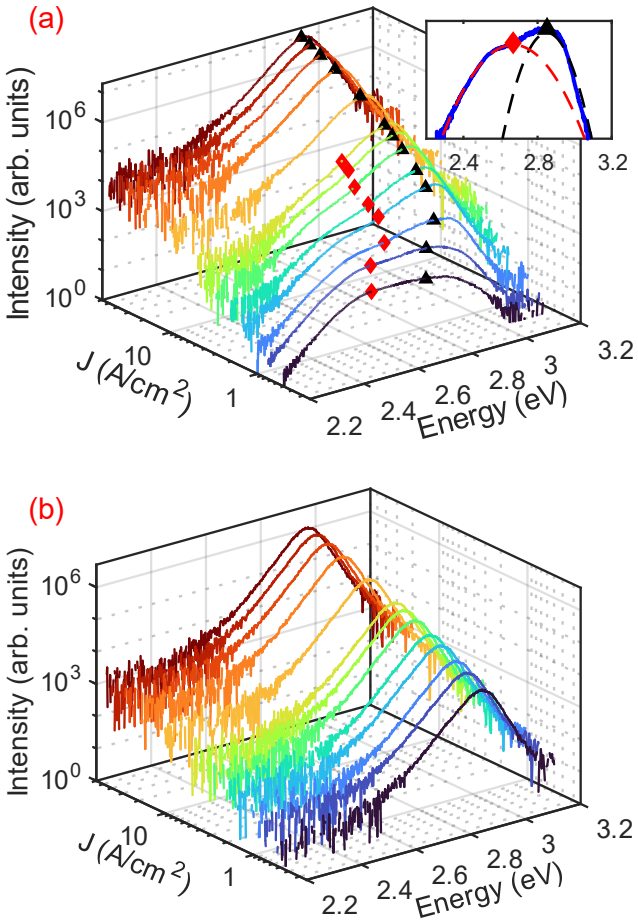

Figure 3.31. Electroluminescence spectra of (a) LED-9UD and (b) LED-9D at different current densities. The fitted ground state (diamond) and excited state (triangle) emission peaks are also shown in the Figure 3.31(a). Inset: EL spectrum and the fitted curves (dashed lines) at 1 A/cm^2.

Compared to the ground states, the excited states are closer to the top of the well. Since the population in the excited states is important for both LED-9UD and LED-9D, the carrier overflow from the QW via thermionic emission can be substantial for the lighter electrons. As shown in Figure 3.30(a)(b) due to the large energy separation between eigenstates for LED-9UD, the excited state is close to the top of the well (p-side), resulting in a small effective barrier (measured relative to the first excited state). Compared to LED-9UD, there is a larger barrier for LED-9D due to the flatter band which brings down the energy levels of the excited

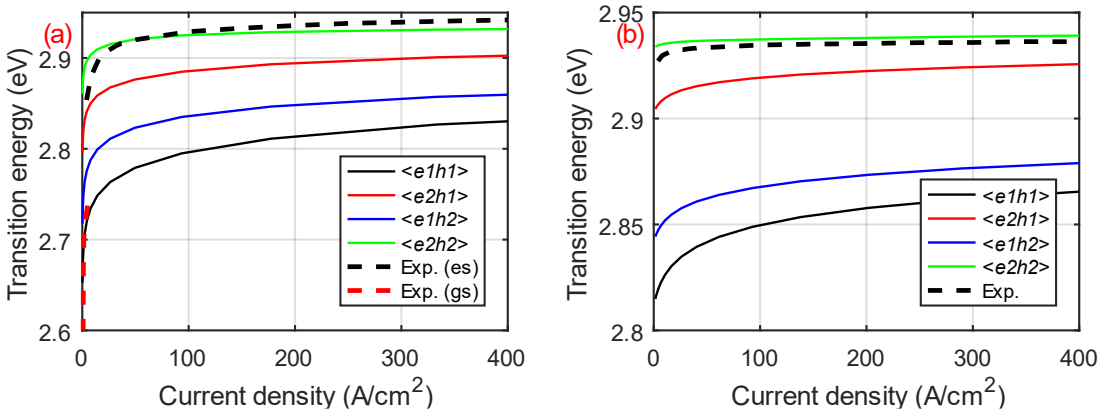

Figure 3.32. Calculated and experimental transition energies as a function of current density of (a) LED-9UD and (b) LED-9D.

states. In the p-side quantum barriers, the separation between the conduction band and the quasi-Fermi level of LED-9D is larger than that of LED-9UD, leading to less carrier overflow for LED-9D. On top of the lower excited states of LED-9D in the QW, the ionized acceptors in the doped barriers also push the quasi-Fermi level toward the valence band, thereby raising the conduction band and further improving the confinement of the electrons in the QW. Consequently, carrier overflow should impact LED-9UD more than LED-9D. The escaped electrons recombine swiftly once they reach the p-type region due to the short minority carrier lifetime. Even though there is a p-AlGaN EBL in the structure which aims to reduce the carrier overflow, the defective AlGaN layer could also provide a pathway for trap-assisted Auger recombination (TAAR) which is a nonradiative recombination mechanism [32,33]. Therefore, LED-9UD is expected to have a lower external quantum efficiency (EQE) than LED-9D even though both LEDs have an efficient recombination pathway via transitions involving excited states.

3.5.4 External quantum efficiency and electroluminescence wavelengths

The external quantum efficiency (EQE) of the LEDs was also measured. Following the device fabrication, devices were mounted on silver headers, wire bonded, and encapsulated in silicone to improve light extraction. The packaged devices were then tested in a calibrated integrating sphere at current densities up to 400 A/cm^2 under pulsed conditions (3-5% duty cycle with 10 μs pulse widths) to minimize heating.

Figure 3.33(a) presents the dependence of the EQE on the current density of the 4 LEDs. LED-3UD which is the most representative of commercial MQW LEDs has a peak EQE of 40% at 6 A/cm^2 with 43% efficiency droop at 400 A/cm^2. The efficiency droop is defined as: droop = $(1 - EQE_J/EQE_{peak})\times 100\%$, where the EQE_{peak} and EQE_J represent the peak EQE and the EQE at different current densities, respectively. The significant droop observed in LED-3UD is common in *c*-plane InGaN/GaN LEDs where the quantum efficiency typically peaks at current densities less than 10 A/cm^2 and drops substantially as the current density increases.

With a thicker 9 nm QW, LED-9UD has a lower peak EQE (32%) than that of LED-3UD. The lower efficiency is likely due to the carrier overflow as previously discussed. However, at high current densities, where Auger recombination dominates, the EQE of LED-9UD surpasses that of LED-3UD due to the reduced carrier density resulting from the thicker QW. Similar efficiency trends have also been observed with increasing QW thickness in *c*-plane LEDs [34,35].

With the doped barriers, LED-9D performed significantly better than LED-9UD, with the highest peak EQE (42%) among the four LEDs in the study. It has an EQE that peaks at 40 A/cm^2 and exhibits a low efficiency droop of 14% at 400 A/cm^2. Comparison of the efficiency

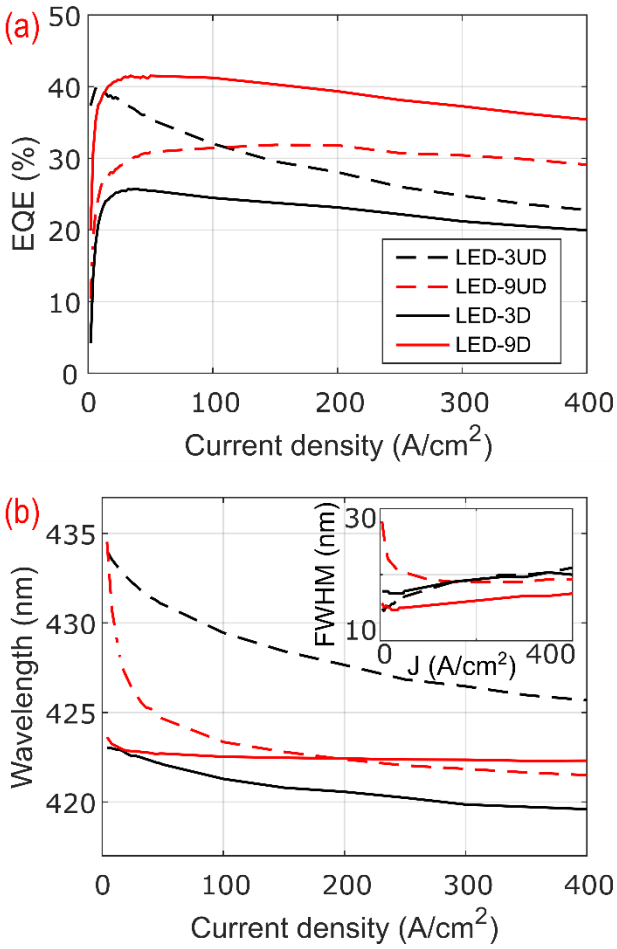

Figure 3.33. (a) External quantum efficiency and (b) EL peak wavelength versus current density of the 4 LEDs. Inset: Full width at half maximum (FWHM) versus current density.

droop should only be made among LEDs with similar peak EQE. Therefore, only the efficiency droop of LED-3UD and LED-9D is reported. Although both LED-9UD and LED-9D have thick QWs, LED-9D has a much higher EQE at high current densities. Apart from the carrier overflow problem, LED-9UD also has a large ground state population due to the much lower <*e1h1*> transition rate and large energy separation between ground and excited states. This partially negates the benefit of using thicker QWs, which are aimed at reducing the carrier densities. Therefore, the doped barriers, which help lowering E_{int}, are essential in achieving efficient thick QW LEDs with low droop.

On the other hand, LED-3D has the lowest EQE in the study regardless of the injected current densities. The reduced E_{int} in the QW due to the doped barriers does not benefit LED-3D as much as LED-9D. This is because thin QW LEDs without doped barriers already have an apparently sufficient wavefunction overlap due to the thin confinement region. Conversely, these doped barriers potentially introduce defect-related NRCs, resulting in a higher SRH rate that explains the low efficiency of LED-3D [7,36,37]. In contrast, its thick QW counterpart (LED-9D) is not significantly impacted by the increased NRCs from the doped barriers. It was suggested that the SRH recombination takes place close to the middle of the QW, where the overlap of the e-h wavefunctions is maximum and not at the defective QW/barrier interfaces [38]. For LED-9D with a thicker QW, the distance between the SRH recombination plane, which is possibly in the middle of the QW, and the NRCs in the doped barriers is larger. This might be a possible explanation for the high quantum efficiency of LED-9D, even at low current densities where the SRH recombination dominates.

Figure 3.33(b) shows the EL peak wavelengths of the LEDs as a function of the current density. The peak wavelengths of LED-3UD and LED-9UD exhibit blueshifts of 8 nm and 13 nm, respectively, over the measured range (1-400 A/cm^2). The blueshifts with increasing current density are common in *c*-plane LEDs, and can be explained by the reduction of the QCSE due to free carrier screening of E_{pol} [39,40]On the other hand, a reduced wavelength shift of 3 nm and 1 nm is observed for the LEDs with doped barriers (LED-3D and LED-9D respectively). Similar small wavelength shifts were also reported for nonpolar and semipolar LEDs where E_{pol} is absent or largely reduced [1,2,41]. The excellent wavelength stability with respect to current density is a desirable feature for display applications [42]. Both LEDs with doped barriers also have shorter emission wavelengths for different reasons. For LED-3D, it is

due to the smaller E_{int} induced redshift, whereas for LED-9D, the shorter emission wavelengths are a result of the higher energy transitions involving excited states. The full width at half maximum (FWHM) of the LEDs (the inset of Figure 3.33(b)) does not vary much with increasing current densities except for LED-9UD which has a larger FWHM at low current densities due to the contribution of both ground state and excited state emissions.

In summary, we have demonstrated *c*-plane InGaN/GaN LEDs with low efficiency droop using a thick SQW with doped barriers. Through biased photocurrent spectroscopy, we showed that the E_{int} of the LEDs with doped barriers is in the same direction as the E_{pn} at zero bias, implying smaller E_{int} in the QWs when LEDs are in operating conditions. Even with the improvement in the ground state wavefunction overlap, thick QW LEDs strongly rely on excited state transitions as observed spectroscopically. Without doped barriers, the thick QW LED suffers from carrier overflow due to the poor confinement of carriers in the excited states. On the other hand, with doped barriers, the E_{int} is reduced, resulting in a flatter band and better confinement of such carriers in the QW and diminishing carrier overflow. Properly designed doped barriers are essential in achieving low droop and efficient thick InGaN/GaN SQW LEDs.

3.6 Impact of doped barriers on the recombination coefficients of *c*-plane InGaN/GaN single quantum well LEDs

In this section, differential carrier lifetime measurements were performed on three sets of *c*-plane InGaN/GaN single quantum well (QW) light-emitting diodes (LEDs). These LEDs were of different QW indium compositions as well as with and without doped barriers. Coupled with the quantum efficiency measurements, the recombination coefficients of the LEDs were calculated to understand the effects of doped barriers on the LEDs.

The samples were grown by metalorganic chemical vapor deposition (MOCVD) on *c*-plane patterned sapphire substrates (PSS). The epitaxial structure (Figure 3.34(a)) was similar to that of the LEDs in section 3.5, which began with a 2 μm thick unintentionally doped (UID) GaN template layer, a 2 μm n-GaN layer, a 20-period n-$In_{0.04}Ga_{0.96}N$/GaN 2.2 nm/4.5 nm superlattice and a 30 nm n-GaN layer. The undoped InGaN single QW was capped by a 2 nm GaN layer and sandwiched either between a 12 nm n-type GaN barrier ([Si] = 1.5×10^{19} cm^{-3}) and a 10 nm p-type GaN barrier ([Mg] = 1.7×10^{19} cm^{-3}), or UID GaN barriers of the same thicknesses. The structure was then ended with a 26 nm p-$Al_{0.10}Ga_{0.90}N$ electron blocking layer (EBL), a 100 nm p-GaN, and a 10 nm p^+-GaN contact layer. InGaN QWs with three different compositions (13.5%, 16%, and 22%) were grown, and the corresponding LEDs were denoted as LED-V, LED-B, and LED-G, respectively according to their violet, blue and green light emission, respectively. For every indium composition, two LEDs were grown: one with and the other without doped barriers. These two LEDs have a suffix of 'D' (doped) and 'R' (reference), respectively (e.g. LED-BD and LED-BR correspond to the blue LEDs ([In] = 16%) with and without doped barriers, respectively).

The samples were processed into devices of two sizes (Figure 3.34(b)(c)). The larger devices (0.1 mm^2 active area) were mounted on silver headers, wire bonded, and encapsulated in silicone to improve the light extraction efficiency. The packaged devices were tested in a calibrated integrating sphere from 1 A/cm^2 to 400 A/cm^2 to determine the external quantum efficiency (*EQE*). Pulsed conditions (3-5% duty cycle with 10 μs pulse widths) were used for

LED	Indium comp. (%)	Doped barriers
VR (ref.)	13.5	No
VD (doped)	13.5	Yes
BR	16	No
BD	16	Yes
GR	22	No
GD	22	Yes

Table 3-7. The indium composition and presence or not of doped barriers in the LEDs.

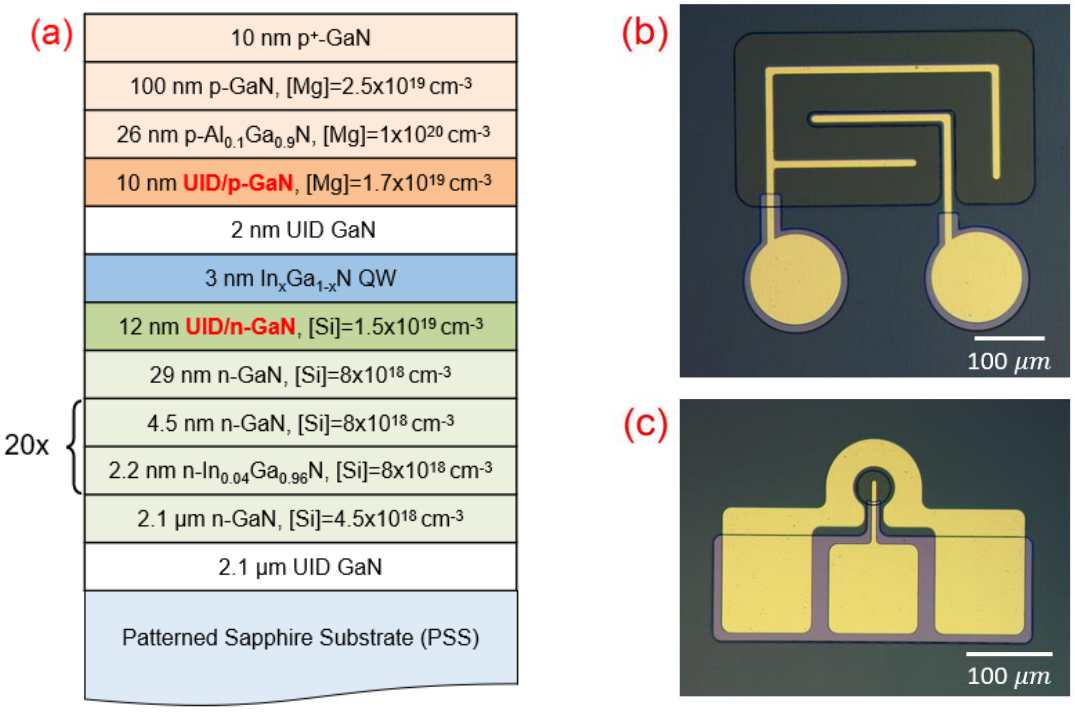

Figure 3.34. (a) Schematic of the epitaxial structure of the LEDs. Optical microscope images of (b) the larger device with 0.1 mm^2 active area (for EQE measurements) and (c) the smaller device with 40 μm diameter (for differential carrier lifetime measurements).

testing above 50 A/cm^2 to minimize heating. The *IQE* of the LEDs was estimated by assuming a light extraction efficiency (*LEE*) of 80% based on ray tracing simulations [43] (i.e. $IQE = EQE/LEE$). Smaller devices with circular mesas (40 μm diameter) were used for differential carrier lifetime measurements.

3.6.1 External quantum efficiency and electroluminescence wavelengths

We first compare the measured *EQE* of the six LEDs, as shown in Figure 3.35(a). At the low indium content of 13.5%, the LED with doped barriers (LED-VD) has lower efficiency than the reference LED (LED-VR). This is because the doped barriers also introduce defect-

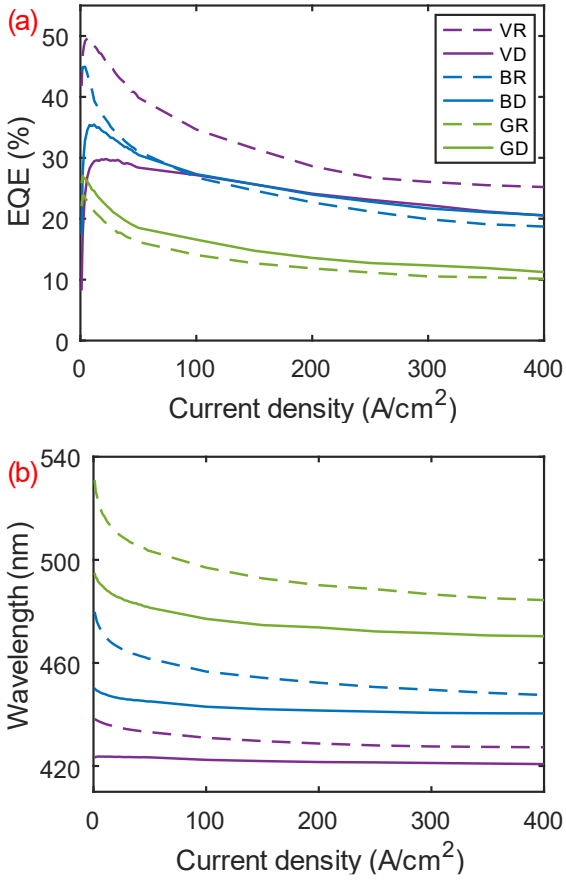

Figure 3.35. (a) External quantum efficiency and (b) EL peak wavelength vs current density of the LEDs with (VD, BD, and GD) and without doped barriers (VR, BR, and GR).

related non-radiative recombination centers (NRCs), which enhance the non-radiative recombination coefficient [7,23,36,37]. However, the increasing indium content reduces the *EQE* difference between LEDs with and without doped barriers. Although LED-BD has a lower peak *EQE* (36%) than the reference LED-BR (which has a peak EQE of 45%), it has a higher *EQE* at high current densities (>100 A/cm^2). For the highest indium content in this study (22%), with doped barriers, LED-GD has higher efficiency than its counterpart (LED-GR) regardless of current densities. It seems that the higher NRCs, due to the doped barriers, impact the LEDs with high-composition QWs less than that with low-composition QWs.

The dependence of the electroluminescence (EL) peak wavelengths on the current density is shown in Figure 3.35(b). As expected, LEDs with doped barriers have shorter emission wavelengths due to the reduced quantum confined Stark effect (QCSE) from reduced internal electric fields. On top of that, they also exhibit smaller variation in wavelengths with respect to the current density due to the reduced internal electric field to be screened by injected carriers, consistent with previous results [7,23]. An one-dimensional Schrödinger-Poisson drift-diffusion solver was used to compute the ground state (<*e1h1*>) transition energies of the six LEDs [12]. The transition energies (converted to photon wavelength) calculated using 50% and 100% theoretical polarization values were plotted in Figure 3.36. There are some discrepancies between the experimental and simulated emission wavelengths, especially for higher composition LEDs. This is partly due to the uncertainty in the polarization values used in the simulations and the inability of 1D simulations to account for alloy disorder in InGaN layers. Nonetheless, the variation in wavelengths with increasing current densities is well captured by the simulations (i.e., smaller variation for LEDs with doped barriers).

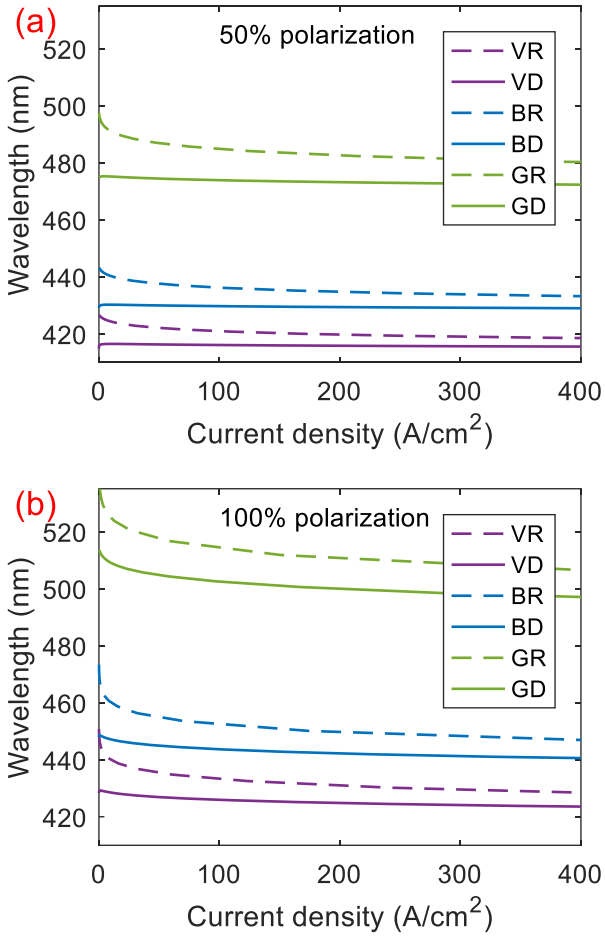

Figure 3.36. Calculated ground state transition energies (converted to photon wavelength) vs. current density of the LEDs using (a) 50% polarization values and (b) 100% polarization values

3.6.2 Differential carrier lifetime measurements and evaluation of recombination coefficients

Figure 3.37 presents the schematic of the differential carrier lifetime measurement setup. During the measurement, a small-signal voltage (100 mV) from a network analyzer (PNA-X N5247A) was added to a DC bias using a bias tee and then applied to the LEDs using a micro-probe (ACP40-GS-50). The small-signal frequency was swept from 10 MHz to 500 MHz. The modulated output light was then collected using an optical fiber and fed into a high-

speed silicon photodetector (UPD-200-UP). Following this, the signal was amplified by a low noise amplifier and sent back to the network analyzer. To account for the frequency response of the photodetector and amplifier, the response was measured separately by a high-speed laser and subtracted from the response of the LEDs. Differential carrier lifetimes of the LEDs were then obtained by fitting the input impedance (Figure 3.38(a)) and modulation response (Figure

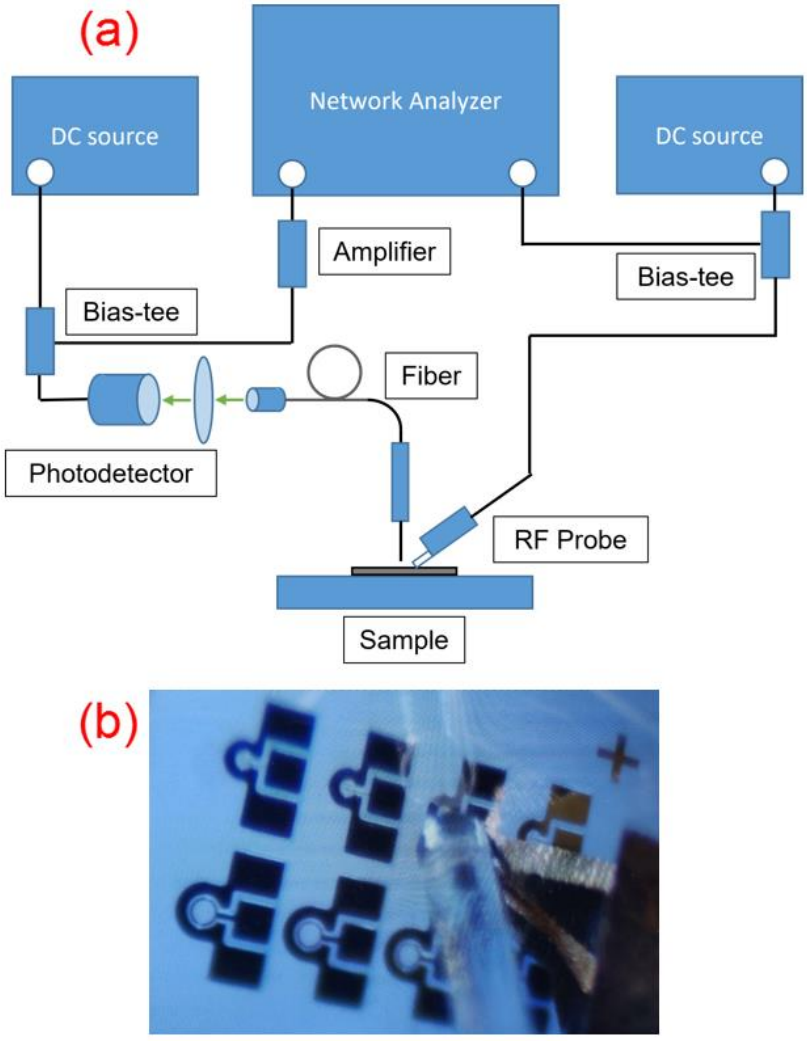

Figure 3.37. (a) Schematic of the differential carrier lifetime measurement setup. (b) Image of a device under test. Optical fiber is used to collect the modulated light from the top of the LED. The RF micro-probe is also shown in the image.

3.38(b)) of the LEDs using a rate equation-based recombination model [44]. The equations for the input impedance (Z_{in}) and modulation response $H(\omega)$ are given by:

$$Z_{in}(\omega) = R_s + \frac{R_c(1+j\omega\tau) + R_w}{(1+j\omega\tau)(1+j\omega\tau_0) + j\omega C_{tot} R_w} \quad (5)$$

$$H(\omega) = \frac{v_{out}(\omega)}{v_w(\omega)} = \frac{R_w}{R_s(1+j\omega\tau)(1+j\omega\tau_0) + R_s(j\omega R_w C_{tot}) + R_c(1+j\omega\tau) + R_w}. \quad (6)$$

Figure 3.39(a) shows the dependence of the differential carrier lifetime of the LEDs on current density. For the same indium content, the lifetimes of LEDs with doped barriers are approximately 50% shorter than that of the reference LEDs. It is possible that shorter lifetimes can solely be due to the higher Shockley-Read-Hall (SRH) coefficient as a result of defects introduced by the doped barriers. However, as we shall see in the subsequent analysis, the shorter lifetimes are the combination of both higher radiative and non-radiative recombination coefficients in the LEDs with doped barriers.

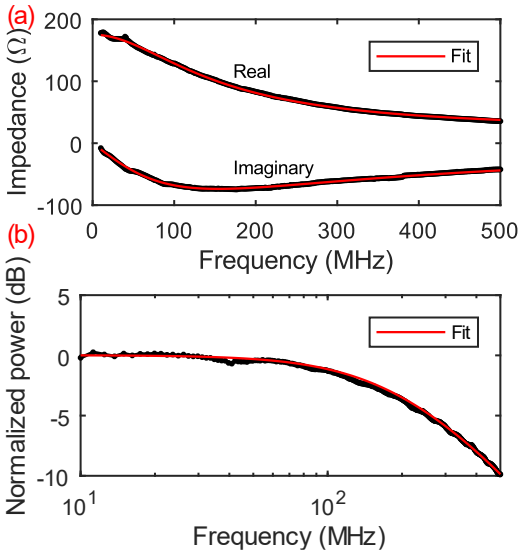

Figure 3.38. (a) The real and imaginary parts of the input impedance and (b) the modulation response of LED-BD at 200 A/cm^2. Black dots and lines: experimental data; red lines: model.

With differential carrier lifetime (τ), the carrier density (n) can then be determined using the following integral [45]:

$$n = \int_0^G \tau \, dG \tag{7}$$

where $G = (J/qh)$, J, q, and h are the total generation rate, current density, electron charge, and active region thickness, respectively. Although the evaluation of n requires τ at zero current density (τ_0), in actuality, τ can only be measured down to a minimum current density. Thus, the usual procedure is to extrapolate τ and assume τ to be constant at low current density where SRH-dominated regime is reached. Unfortunately, τ did not plateau even at the smallest current density in the measurement. Instead, n is calculated by choosing τ_0 to be τ measured

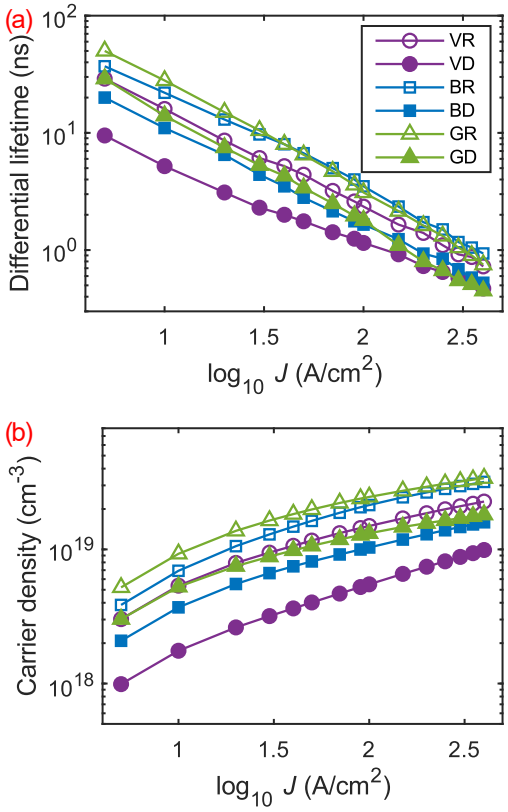

Figure 3.39. (a) The extracted differential carrier lifetimes and (b) carrier density (calculated from Eq. 7) vs current density of the LEDs.

at the lowest current density (5 A/cm^2 in this study). Since the actual τ_0 should be higher than the value used in the calculation, the calculated *n* can be seen as the lower bound of the actual values. Figure 3.39(b) shows the calculated *n* of the LEDs. As expected, LEDs with doped barriers also have a lower *n* at a given current density due to the shorter τ.

At steady state, *G* is also the total recombination rate. After separating *G* into a radiative rate ($G_R = G \times IQE$) and a non-radiative rate ($G_{NR} = G \times (1 - IQE)$, the recombination coefficients in the simple *ABC* model, namely the SRH (*A*), radiative (*B*), and Auger (*C*) coefficients can then be estimated following the work of David *et al.* [45,46]. Three recombination quantities are calculated: G_{NR}/n, $B = G_R/n^2$, and $C = (G_{NR} - An)/n^3$ where *A* is the value of G_{NR}/n at low current density where the Auger recombination is negligible because of its n^3 dependence. On top of the standard non-radiative SRH recombination and Auger recombination, there could be other possible non-radiative recombination mechanisms. Trap-assisted Auger recombination (TAAR) has been observed by electron emission spectroscopy [32] as well as forward-bias photocurrent measurement [47] and was invoked as a source of green gap by David *et al.* [46]. However, we do not have an independent way to introduce defects in otherwise identical structures in this study as the introduction of defects by doped barriers not only increases the NRCs but also enhances the wavefunction overlap. Since it is difficult to decouple TAAR effect from the other recombination channels in the *ABC* model, we do not consider TAAR in this study. The three calculated quantities are shown in Figure 3.40 as functions of *n*.

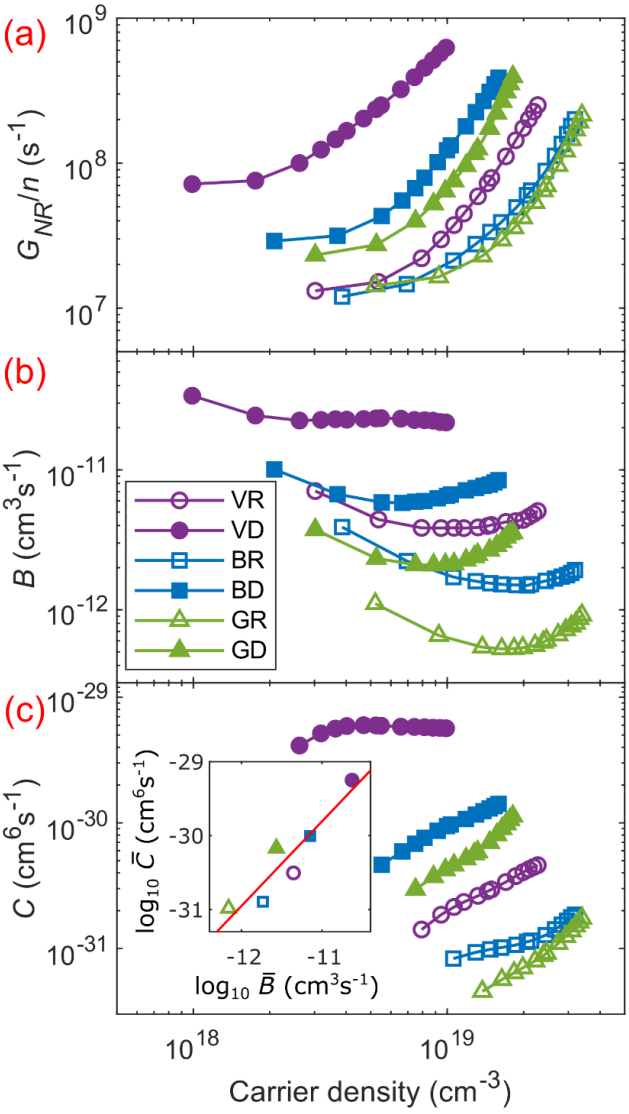

Figure 3.40. (a) G_{NR}/n (the value at low J yields SRH coefficient A), (b) the radiative coefficient B, and (c) the Auger coefficient C as a function of carrier density. Inset: The correlation between the average B and C (on a log-log scale).

3.6.3 Discussion

As shown in Figure 3.40(a), for all LEDs, the quantity G_{NR}/n converges to a constant value at low current densities which should be equal to their SRH coefficient A. The radiative and Auger coefficients B and C (Figure 3.40(b)(c)) are carrier dependent as reported in similar

experiments [48–50]. An enhancement of *B* at low *n* and high *n*, which can be explained by Coulomb interaction and free carrier screening respectively, is observed for all LEDs [48]. There is a significant correlation between the *B* and *C* as functions of carrier density, the In content, and the presence or not of doped barriers since the wavefunction overlap affects both recombination processes [49,51]. The values of *B* and *C* are averaged over the measured range and are shown in the inset of Figure 3.40(c). We found that the increase of *B* is accompanied by an increment of *C* similar to what was reported in Ref. 49.

In Figure 3.41, *A* and the average values of *B* are also plotted as a function of indium composition. As seen in Figure 3.41(b), *B* decreases with increasing indium composition. This is expected as the higher polarization-induced electric field in higher indium composition QW results in an even smaller wavefunction overlap, which in turn leads to a reduced radiative transition rate. Most importantly, the presence of doped barriers in the LEDs leads to higher radiative coefficients, where an enhancement of 4-5 times was observed. The higher radiative coefficients are strong indicators that doped barriers lead to a reduction in internal electric fields in the QWs, which is their desired effect.

As mentioned above, doped barriers also introduce NRCs which lead to a higher detrimental SRH coefficient. Higher *A* indeed is observed for all LEDs with doped barriers. The work to identify the defects responsible for the more numerous NRCs is in progress with Mg-related defects as one of the candidates. It is also known that SRH recombination shows a strong dependence on wavefunction overlap [38,51]. The improved wavefunction overlap in LEDs with doped barriers further exacerbated the non-radiative SRH recombination. However, the increase in *A* is observed to be smaller with increasing indium composition (5.5 times and 1.6 times higher for violet and green LEDs, respectively). This is not surprising as it was

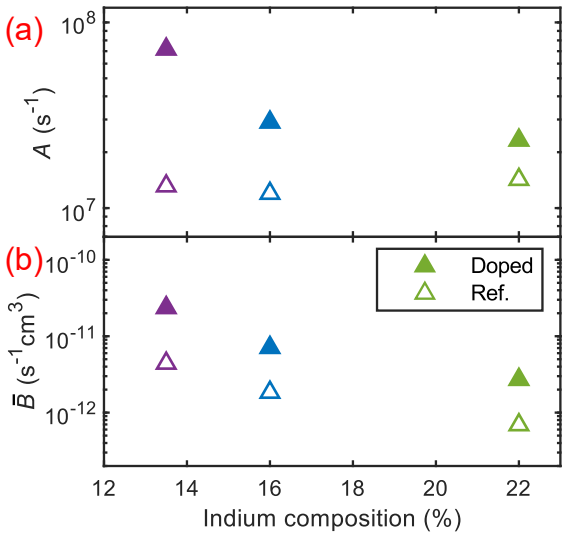

Figure 3.41. (a) SRH coefficient *A* and (b) average radiative coefficient *B* as a function of indium composition.

reported that in high-composition QWs, the overlap dependence of SRH coefficients is less pronounced possibly due to a change in the physics governing SRH recombinations [46]. Additionally, even without the doped barriers, since NRCs increase with increasing indium composition [52], the additional NRCs from the doped barriers contribute to a smaller fraction of the total NRCs in the QW with higher indium composition. As such, the penalty associated with the doped barriers is less severe for high-composition QWs. This explains the observed EQE trend where LEDs with doped barriers outperform the reference LEDs at high indium composition.

In general, the beneficial enhancement in *B* is accompanied by the unwanted increase in the non-radiative coefficients *A* and *C* partly due to the similar overlap dependence of these non-radiative recombination processes. Nonetheless, the larger recombination coefficients result in a decrease in *n* at a given injected current density as shown in Figure 3.39(b). The reduced *n* should delay the efficiency droop onset to higher current densities [7,30] although

only slight improvement in efficiency was observed for LED-BD and LED-GD at high current densities.

A major drawback in employing doped barriers in LEDs is the blueshifted emission wavelengths. The reduction in the internal electric field leads to a flatter energy band in the QW. This decreases the field-induced redshift, resulting in emitted photons with energies closer to the flat-band values. Therefore, a shorter emission wavelength is an unavoidable consequence of reducing the internal electric field in the QW, making this technique to be less optimal for achieving long wavelength emitters in the visible range. Despite that, this approach is not only limited to InGaN/GaN QW. It can also be applied to AlGaN-based UV emitters, where a shorter emission wavelength is desirable and the large internal electric field in the QW remains a problem [53].

In conclusion, through the use of doped barriers, we studied the impact of reduced internal electric fields on the recombination coefficients in the QW. Higher recombination coefficients *A*, *B*, and *C* were observed in the LEDs with doped barriers due to their dependence on wavefunction overlap. Doped barriers also introduce additional NRCs, which further enhance the *A* coefficients although the effect is less for high-composition QWs, resulting in the efficiency of the LEDs with doped barriers exceeding that of the reference LEDs. Despite the higher SRH coefficients, doped barriers present another approach to manipulating the internal electric fields in *c*-plane InGaN/GaN QWs.

3.6.4 Modulation bandwidths

Differential carrier lifetime measurement also allows us to determine the modulation bandwidths of the LEDs. The shorter carrier lifetimes or faster recombination dynamics in

LEDs with doped barriers enhance their modulation bandwidths, making them suitable for high-speed applications in visible light communication (VLC). Figure 3.42(a) shows the normalized frequency response of the LEDs at 400 A/cm^2. The extracted 3-dB bandwidths are also plotted in Figure 3.42(b) as a function of current density. The 3-dB bandwidths of the LEDs increase with current density due to the decreasing carrier lifetimes at high current densities. On top of that, LEDs with doped barriers (VD, BD, and GD) show higher 3-dB bandwidth than the reference LEDs (VR, BR, and GR). This is expected as LEDs with doped barriers have much shorter carrier lifetimes. 3-dB bandwidths of 265 MHz, 284 MHz, and 347 MHz were demonstrated by LED-VD, LED-BD, and LED-GD respectively at 400 A/cm^2 whereas the bandwidths of the reference LEDs are around 165 MHz to 206 MHz at the same current density.

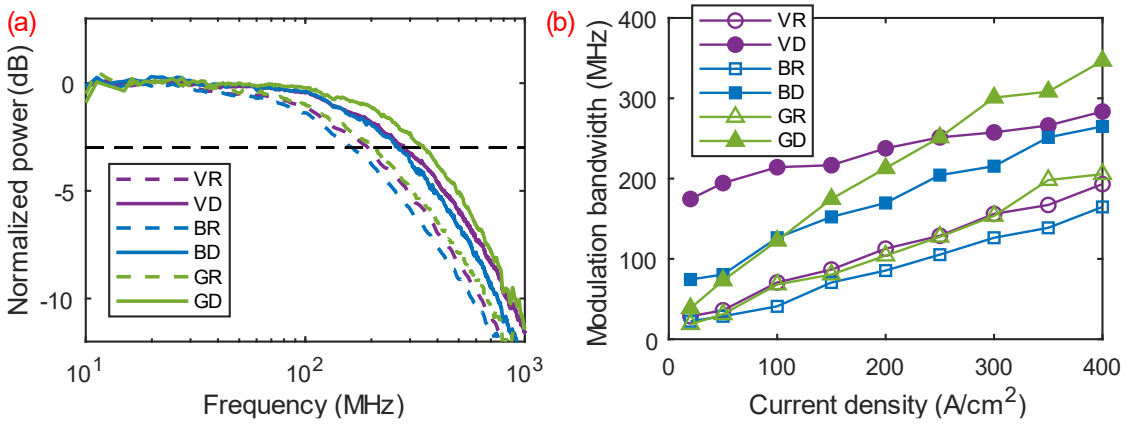

Figure 3.42. (a) Normalized frequency response of the LEDs at 400 A/cm^2. (b) 3-dB bandwidth of LEDs vs current density.

3.7 Conclusion

In this work, doped barriers were used to control the internal electric fields in *c*-plane InGaN quantum wells (QWs), with the purpose of minimizing band-tilting in the QWs and improving the wavefunction overlap between electron and hole. Device simulations were performed to investigate how the placement and doping levels of the doped barriers modify the electric fields in the junction and in the QW. Growth optimizations were conducted on both thin and thick single QW LEDs to minimize the non-radiative recombination centers originating from the heavily doped barriers while ensuring effective field reduction in the QWs. With doped barriers, a thick QW active region was employed to reduce the carrier density and thus delay the onset of the efficiency droop to higher carrier densities. Low efficiency droop 9-nm-thick *c*-plane SQW LEDs were demonstrated. Biased photocurrent spectroscopy (BPCS) was also carried out to probe the internal electric fields in the devices. Through BPCS, we showed that, for LEDs with doped barriers, the increase in the *p*-*n* junction field manages to change the direction of the internal electric field at zero bias, implying smaller internal electric fields when LEDs are in operating conditions. Lastly, differential carrier lifetimes measurements were performed on LEDs of different QW indium compositions as well as with and without doped barriers. LEDs with doped barriers show short lifetimes and low carrier densities in the active region compared to the reference LEDs. Despite higher non-radiative SRH and Auger coefficients, improvement of radiative coefficients was indeed observed for LEDs with doped barriers, affirming the roles of doped barriers in reducing the internal electric fields and improving the wavefunction overlap.

References:

1. D. L. Becerra, Y. Zhao, S. H. Oh, C. D. Pynn, K. Fujito, S. P. DenBaars, and S. Nakamura, "High-power low-droop violet semipolar ($30\bar{3}\bar{1}$) InGaN/GaN light-emitting diodes with thick active layer design," Appl. Phys. Lett. **105**, 171106 (2014).

2. S. H. Oh, B. P. Yonkee, M. Cantore, R. M. Farrell, J. S. Speck, S. Nakamura, and S. P. DenBaars, "Semipolar III-nitride light-emitting diodes with negligible efficiency droop up to ~1 W," Appl. Phys. Express **9**, 102102 (2016).

3. Y. Zhao, Q. Yan, C.-Y. Huang, S.-C. Huang, P. Shan Hsu, S. Tanaka, C.-C. Pan, Y. Kawaguchi, K. Fujito, C. G. de Walle, J. S. Speck, S. P. DenBaars, S. Nakamura, and D. Feezell, "Indium incorporation and emission properties of nonpolar and semipolar InGaN quantum wells," Appl. Phys. Lett. **100**, 201108 (2012).

4. B. N. Bryant, A. Hirai, E. C. Young, S. Nakamura, and J. S. Speck, "Quasi-equilibrium crystal shapes and kinetic Wulff plots for gallium nitride grown by hydride vapor phase epitaxy," J. Cryst. Growth **369**, 14–20 (2013).

5. K. Fujito, S. Kubo, and I. Fujimura, "Development of Bulk GaN Crystals and Nonpolar/Semipolar Substrates by HVPE," MRS Bull. **34**, 313–317 (2009).

6. V. Fiorentini, F. Bernardini, and O. Ambacher, "Evidence for nonlinear macroscopic polarization in III–V nitride alloy heterostructures," Appl. Phys. Lett. **80**, 1204–1206 (2002).

7. N. G. Young, R. M. Farrell, S. Oh, M. Cantore, F. Wu, S. Nakamura, S. P. DenBaars, C. Weisbuch, and J. S. Speck, "Polarization field screening in thick (0001) InGaN/GaN single quantum well light-emitting diodes," Appl. Phys. Lett. **108**, 61105 (2016).

8. G. Franssen, T. Suski, P. Perlin, R. Bohdan, A. Bercha, W. Trzeciakowski, I. Makarowa, P. Prystawko, M. Leszczyński, I. Grzegory, S. Porowski, and S. Kokenyesi, "Fully-screened polarization-induced electric fields in blue⁄violet InGaN⁄GaN light-emitting devices grown on bulk GaN," Appl. Phys. Lett. **87**, 41109 (2005).

9. C. G. de Walle and J. Neugebauer, "First-principles calculations for defects and impurities: Applications to III-nitrides," J. Appl. Phys. **95**, 3851–3879 (2004).

10. S. Y. Karpov, "Nitride Semiconductor Devices: Principles and Simulation," in *Nitride Semiconductor Devices: Principles and Simulation*, J. Piprek, ed. (Wiley-VCH, 2007), pp. 1–496.

11. F. Della Sala, A. Di Carlo, P. Lugli, F. Bernardini, V. Fiorentini, R. Scholz, and J.-M. Jancu, "Free-carrier screening of polarization fields in wurtzite GaN/InGaN laser structures," Appl. Phys. Lett. **74**, 2002–2004 (1999).

12. See http://yrwu-wk.ee.ntu.edu.tw/ for more information on the Schrödinger-Poisson drift-diffusion solver developed by Y.-R. Wu *et al*..

13. C. S. Xia, Z. M. Simon Li, Z. Q. Li, Y. Sheng, Z. H. Zhang, W. Lu, and L. W. Cheng,

"Optimal number of quantum wells for blue InGaN/GaN light-emitting diodes," Appl. Phys. Lett. **100**, 263504 (2012).

14. M. Peter, A. Laubsch, W. Bergbauer, T. Meyer, M. Sabathil, J. Baur, and B. Hahn, "New developments in green LEDs," Phys. status solidi **206**, 1125–1129 (2009).

15. S. M. Ting, J. C. Ramer, D. I. Florescu, V. N. Merai, B. E. Albert, A. Parekh, D. S. Lee, D. Lu, D. V Christini, L. Liu, and E. A. Armour, "Morphological evolution of InGaN/GaN quantum-well heterostructures grown by metalorganic chemical vapor deposition," J. Appl. Phys. **94**, 1461–1467 (2003).

16. Y.-L. Hu, R. M. Farrell, C. J. Neufeld, M. Iza, S. C. Cruz, N. Pfaff, D. Simeonov, S. Keller, S. Nakamura, S. P. DenBaars, U. K. Mishra, and J. S. Speck, "Effect of quantum well cap layer thickness on the microstructure and performance of InGaN/GaN solar cells," Appl. Phys. Lett. **100**, 161101 (2012).

17. K. Köhler, T. Stephan, A. Perona, J. Wiegert, M. Maier, M. Kunzer, and J. Wagner, "Control of the Mg doping profile in III-N light-emitting diodes and its effect on the electroluminescence efficiency," J. Appl. Phys. **97**, 104914 (2005).

18. M. Shiojiri, C. C. Chuo, J. T. Hsu, J. R. Yang, and H. Saijo, "Structure and formation mechanism of V defects in multiple InGaN⁄GaN quantum well layers," J. Appl. Phys. **99**, 73505 (2006).

19. B. Heying, E. J. Tarsa, C. R. Elsass, P. Fini, S. P. DenBaars, and J. S. Speck, "Dislocation mediated surface morphology of GaN," J. Appl. Phys. **85**, 6470–6476 (1999).

20. X. H. Wu, C. R. Elsass, A. Abare, M. Mack, S. Keller, P. M. Petroff, S. P. DenBaars, J. S. Speck, and S. J. Rosner, "Structural origin of V-defects and correlation with localized excitonic centers in InGaN/GaN multiple quantum wells," Appl. Phys. Lett. **72**, 692–694 (1998).

21. F. Jiang, J. Zhang, L. Xu, J. Ding, G. Wang, X. Wu, X. Wang, C. Mo, Z. Quan, X. Guo, C. Zheng, S. Pan, and J. Liu, "Efficient InGaN-based yellow-light-emitting diodes," Photon. Res. **7**, 144–148 (2019).

22. C. Lynsky, R. C. White, Y. C. Chow, W. Y. Ho, S. Nakamura, S. P. DenBaars, and J. S. Speck, "Role of V-defect density on the performance of III-nitride green LEDs on sapphire substrates," J. Cryst. Growth **560**–**561**, 126048 (2021).

23. Y. C. Chow, C. Lynsky, F. Wu, S. Nakamura, S. P. DenBaars, C. Weisbuch, and J. S. Speck, "Reduction of efficiency droop in *c*-plane InGaN/GaN light-emitting diodes using a thick single quantum well with doped barriers," Appl. Phys. Lett. **119**, 221102 (2021).

24. M. Piccardo, C.-K. Li, Y.-R. Wu, J. S. Speck, B. Bonef, R. M. Farrell, M. Filoche, L. Martinelli, J. Peretti, and C. Weisbuch, "Localization landscape theory of disorder in semiconductors. II. Urbach tails of disordered quantum well layers," Phys. Rev. B **95**, 144205 (2017).

25. R. T. Collins, K. v. Klitzing, and K. Ploog, "Photocurrent spectroscopy of

$GaAs/Al_xGa_{1-x}$ quantum wells in an electric field," Phys. Rev. B **33**, 4378–4381 (1986).

26. H. Helmers, C. Karcher, and A. W. Bett, "Bandgap determination based on electrical quantum efficiency," Appl. Phys. Lett. **103**, 32108 (2013).

27. C.-K. Li, M. Piccardo, L.-S. Lu, S. Mayboroda, L. Martinelli, J. Peretti, J. S. Speck, C. Weisbuch, M. Filoche, and Y.-R. Wu, "Localization landscape theory of disorder in semiconductors. III. Application to carrier transport and recombination in light emitting diodes," Phys. Rev. B **95**, 144206 (2017).

28. R. Cingolani, A. Botchkarev, H. Tang, H. Morko\ifmmode \mbox\cc\else ç\fi, G. Traetta, G. Coli, M. Lomascolo, A. Di Carlo, F. Della Sala, and P. Lugli, "Spontaneous polarization and piezoelectric field in $GaN/Al_{0.15}Ga_{0.85}N$ quantum wells: Impact on the optical spectra," Phys. Rev. B **61**, 2711–2715 (2000).

29. S.-H. Park, J.-J. Kim, and H.-M. Kim, "Exciton binding energy in wurtzite InGaN/GaN quantum wells," J. Korean Phys. Soc. **45**, 582–585 (2004).

30. A. David and M. J. Grundmann, "Influence of polarization fields on carrier lifetime and recombination rates in InGaN-based light-emitting diodes," Appl. Phys. Lett. **97**, 33501 (2010).

31. G. Muziol, H. Turski, M. Siekacz, K. Szkudlarek, L. Janicki, M. Baranowski, S. Zolud, R. Kudrawiec, T. Suski, and C. Skierbiszewski, "Beyond Quantum Efficiency Limitations Originating from the Piezoelectric Polarization in Light-Emitting Devices," ACS Photonics **6**, 1963–1971 (2019).

32. D. J. Myers, K. Gelžinytė, A. I. Alhassan, L. Martinelli, J. Peretti, S. Nakamura, C. Weisbuch, and J. S. Speck, "Direct measurement of hot-carrier generation in a semiconductor barrier heterostructure: Identification of the dominant mechanism for thermal droop," Phys. Rev. B **100**, 125303 (2019).

33. T. A. Henry, A. Armstrong, A. A. Allerman, and M. H. Crawford, "The influence of Al composition on point defect incorporation in AlGaN," Appl. Phys. Lett. **100**, 43509 (2012).

34. N. F. Gardner, G. O. Müller, Y. C. Shen, G. Chen, S. Watanabe, W. Götz, and M. R. Krames, "Blue-emitting InGaN–GaN double-heterostructure light-emitting diodes reaching maximum quantum efficiency above $200 A/cm^2$," Appl. Phys. Lett. **91**, 243506 (2007).

35. V. Avrutin, S. din A. Hafiz, F. Zhang, Ü. Özgür, H. Morkoç, and A. Matulionis, "InGaN light-emitting diodes: Efficiency-limiting processes at high injection," J. Vac. Sci. \& Technol. A **31**, 50809 (2013).

36. U. Kaufmann, M. Kunzer, H. Obloh, M. Maier, C. Manz, A. Ramakrishnan, and B. Santic, "Origin of defect-related photoluminescence bands in doped and nominally undoped GaN," Phys. Rev. B **59**, 5561–5567 (1999).

37. A. Nirschl, M. Binder, M. Schmid, I. Pietzonka, H.-J. Lugauer, R. Zeisel, M. Sabathil, D. Bougeard, and B. Galler, "Towards quantification of the crucial impact of auger

recombination for the efficiency droop in (AlInGa)N quantum well structures," Opt. Express **24**, 2971–2980 (2016).

38. A. David, C. A. Hurni, N. G. Young, and M. D. Craven, "Field-assisted Shockley-Read-Hall recombinations in III-nitride quantum wells," Appl. Phys. Lett. **111**, 233501 (2017).

39. T. Takeuchi, S. Sota, M. Katsuragawa, M. Komori, H. Takeuchi, H. Amano, and I. Akasaki, "Quantum-Confined Stark Effect due to Piezoelectric Fields in {GaInN} Strained Quantum Wells," Jpn. J. Appl. Phys. **36**, L382--L385 (1997).

40. S. Chichibu, T. Sota, K. Wada, and S. Nakamura, "Exciton localization in InGaN quantum well devices," J. Vac. Sci. & Technol. B Microelectron. Nanom. Struct. Process. Meas. Phenom. **16**, 2204–2214 (1998).

41. Y.-D. Lin, A. Chakraborty, S. Brinkley, H. C. Kuo, T. Melo, K. Fujito, J. S. Speck, S. P. DenBaars, and S. Nakamura, "Characterization of blue-green m-plane InGaN light emitting diodes," Appl. Phys. Lett. **94**, 261108 (2009).

42. R. Lu, Q. Hong, Z. Ge, and S.-T. Wu, "Color shift reduction of a multi-domain IPS-LCD using RGB-LED backlight," Opt. Express **14**, 6243–6252 (2006).

43. C. Lalau Keraly, L. Kuritzky, M. Cochet, and C. Weisbuch, "Ray Tracing for Light Extraction Efficiency (LEE) Modeling in Nitride LEDs," in *III-Nitride Based Light Emitting Diodes and Applications*, T.-Y. Seong, J. Han, H. Amano, and H. Morkoç, eds. (Springer Singapore, 2017), pp. 301–340.

44. A. Rashidi, M. Nami, M. Monavarian, A. Aragon, K. DaVico, F. Ayoub, S. Mishkat-Ul-Masabih, A. Rishinaramangalam, and D. Feezell, "Differential carrier lifetime and transport effects in electrically injected III-nitride light-emitting diodes," J. Appl. Phys. **122**, 35706 (2017).

45. A. David, N. G. Young, C. Lund, and M. D. Craven, "Review — The Physics of Recombinations in III-Nitride Emitters," ECS J. Solid State Sci. Technol. **9**, 16021 (2020).

46. A. David, N. G. Young, C. A. Hurni, and M. D. Craven, "Quantum Efficiency of III-Nitride Emitters: Evidence for Defect-Assisted Nonradiative Recombination and its Effect on the Green Gap," Phys. Rev. Appl. **11**, 31001 (2019).

47. A. C. Espenlaub, D. J. Myers, E. C. Young, S. Marcinkevičius, C. Weisbuch, and J. S. Speck, "Evidence of trap-assisted Auger recombination in low radiative efficiency MBE-grown III-nitride LEDs," J. Appl. Phys. **126**, 184502 (2019).

48. A. David, N. G. Young, and M. D. Craven, "Many-Body Effects in Strongly Disordered III-Nitride Quantum Wells: Interplay Between Carrier Localization and Coulomb Interaction," Phys. Rev. Appl. **12**, 44059 (2019).

49. A. David, N. G. Young, C. Lund, and M. D. Craven, "Compensation between radiative and Auger recombinations in III-nitrides: The scaling law of separated-wavefunction recombinations," Appl. Phys. Lett. **115**, 193502 (2019).

50. A. David, N. G. Young, C. A. Hurni, and M. D. Craven, "All-optical measurements of carrier dynamics in bulk-GaN LEDs: Beyond the ABC approximation," Appl. Phys. Lett. **110**, 253504 (2017).

51. E. Kioupakis, Q. Yan, and C. G. de Walle, "Interplay of polarization fields and Auger recombination in the efficiency droop of nitride light-emitting diodes," Appl. Phys. Lett. **101**, 231107 (2012).

52. A. M. Armstrong, M. H. Crawford, and D. D. Koleske, "Contribution of deep-level defects to decreasing radiative efficiency of InGaN/GaN quantum wells with increasing emission wavelength," Appl. Phys. Express **7**, 32101 (2014).

53. M. H. Crawford, "Chapter One - Materials Challenges of AlGaN-Based UV Optoelectronic Devices," in *III-Nitride Semiconductor Optoelectronics*, Z. Mi and C. Jagadish, eds., Semiconductors and Semimetals (Elsevier, 2017), Vol. 96, pp. 3–44.